

# ABSTRACT

A STUDY OF THE REACTION  $\bar{p}n \rightarrow \pi^+ \pi^- \pi^-$   
FROM 1.09 TO 1.43 GeV/c

By

James Michael Mountz

In a deuterium bubble chamber experiment 3, 4, 5, and 6 prong topological cross sections were obtained for an incident antiproton momenta from 1.09 to 1.43 GeV/c. Also determined were cross sections for the reactions  $\bar{p}n \rightarrow \pi^+ \pi^- \pi^-$ ,  $\bar{p}n \rightarrow \rho^0 \pi^-$  and  $\bar{p}n \rightarrow f^0 \pi^-$ .

The differential cross sections for  $\bar{p}n \rightarrow \rho^0 \pi^-$  and  $\bar{p}n \rightarrow f^0 \pi^-$  were obtained. A test of the crossing symmetry principle was made by comparing the differential cross sections for the reaction  $\bar{p}n \rightarrow \rho^0 \pi^-$  with those of its line reversed reaction  $\pi^- p \rightarrow n \rho^0$ . Within experimental error the crossing symmetry principle was found to be valid for these reactions.

In an analysis of the c.m. angular distributions for the  $\rho^0$  and  $f^0$  mesons the spin state composition of the  $\bar{p}n$  system was found to be predominately in a  $s = 2$  state.

The Dalitz plot was used to compare the predictions of the Veneziano model with the data. The overall agreement

is good, but

prominent whe

2.0 GeV/c.

James Michael Mountz

is good, but the areas of discrepancies become more prominent when the model is compared to data from 1.6 to 2.0 GeV/c.

A

in part



A STUDY OF THE REACTION  $\bar{p}n \rightarrow \pi^+ \pi^- \pi^-$   
FROM 1.09 TO 1.43 GeV/c

By

James Michael Mountz

A DISSERTATION

Submitted to  
Michigan State University  
in partial fulfillment of the requirements  
for the degree of

DOCTOR OF PHILOSOPHY

Department of Physics

1974

I wish t

H. Zee Ming M

the analysis

gained from h

make the work

enjoyable. M

Gerald A. Smi

during the ph

our scanning a

during the mea

I am grat

during the las

for the encour

## ACKNOWLEDGMENTS

I wish to express my appreciation to Professor H. Zee Ming Ma, for his patience and guidance throughout the analysis of this experiment. The motivation that I gained from his friendly and thoughtful advice helped to make the work involved in preparing this dissertation more enjoyable. Many thanks are due also to Professor Gerald A. Smith for his helpful suggestions and comments during the physics analysis of the data. I am thankful to our scanning and measuring staff for all their efforts during the measurement phase of this experiment.

I am grateful to my wife Gail, for her devotion to me, during the last year of this research. I am also grateful for the encouragement that I received from my parents.

1

LIST OF TABLE

LIST OF FIGUR

Chapter

I. INTROD

II. CROSS

2.1

2.2

2.3

2.4

2.5

2.

2.

2.6

2.

2.

2.

2.

III. RESONA

3.1

3.2

3.3

## TABLE OF CONTENTS

	Page
LIST OF TABLES . . . . .	v
LIST OF FIGURES. . . . .	viii
 Chapter	
I. INTRODUCTION . . . . .	1
II. CROSS SECTION MEASUREMENTS. . . . .	3
2.1 Scanning and Corrections . . . . .	3
2.2 Measuring and Corrections. . . . .	6
2.3 Fiducial Volume Length. . . . .	8
2.4 Track Count . . . . .	9
2.5 The Interaction Likelihood . . . . .	10
2.5.1 Corrections for Unseen Elastics . . . . .	11
2.5.2 The Interaction Likelihood Calculation . . . . .	14
2.6 Topological and Reaction Cross Section . . . . .	14
2.6.1 Separation of $\bar{p}p$ Contaminations . . . . .	19
2.6.2 Topological Cross Section Calculations . . . . .	33
2.6.3 Acceptance Criteria for Events for the Reaction $\bar{p}n \rightarrow \pi^+ \pi^- \pi^0$ . . . . .	41
2.6.4 $\bar{p}n \rightarrow \pi^+ \pi^- \pi^0$ Reaction Cross Section Calculation. . . . .	45
III. RESONANCE PRODUCTION. . . . .	51
3.1 The $\rho^0 \pi^-$ , $f^0 \pi^-$ Resonance Production . . . . .	51
3.2 Event Selection . . . . .	51
3.3 Resonance Cross Section Determination . . . . .	57

Chapter	Page
IV. DIFFERENTIAL CROSS SECTIONS AND COMPARISON OF LINE REVERSED REACTIONS . . . . .	66
4.1 Motivation and Formalism . . . . .	66
4.2 Experimental Analysis . . . . .	71
4.3 The Line Reversed Reaction Comparisons. . . . .	79
V. SPIN DETERMINATION OF THE ANTIPROTON NEUTRON SYSTEM . . . . .	83
5.1 Formalism . . . . .	83
5.2 Analysis . . . . .	87
VI. THE DALITZ PLOT FOR THE $\bar{p}n \rightarrow \pi^+ \pi^- \pi^-$ REACTION AND ITS COMPARISON WITH THE PREDICTIONS OF THE VENEZIANO MODEL . . . . .	91
6.1 Motivation, Theoretical Background and Analysis . . . . .	91
VII. SUMMARY AND CONCLUSIONS. . . . .	117
APPENDICES	
Appendix	
A. Scanning Efficiency Determination . . . . .	120
B. Measuring Efficiency Determination . . . . .	130
C. Fiducial Volume Length Calculation . . . . .	134
D. Track Count. . . . .	140
E. Proof That Equal Areas on the Dalitz Plot Correspond to Equal Probabilities in Phase Space . . . . .	147
LIST OF REFERENCES. . . . .	150

Table

2.1. The sc  
perc

2.2. Measur  
...

2.3. The av  
beam

2.4. The num  
fidu

2.5. The in  
dc/dc

2.6. Experim  
inter

2.7. Event t

2.8. The num

2.9a. Slowest  
chara  
Figur

2.9b. Charact  
distr  
track

2.10. Probabi  
a par  
of th

2.11a. Contami  
the 4

# LIST OF TABLES

Table	Page
2.1. The scanning efficiency, given in terms of percentage of correct events . . . . .	7
2.2. Measurement efficiencies for the $\bar{p}d \rightarrow p_{sp} + \dots$ topological cross section. . . $p_{sp}$ .	8
2.3. The average tracklength of the incident beam particles. . . . .	9
2.4. The number of beam tracks entering the fiducial volume . . . . .	10
2.5. The intercept and slope parameters for $d\sigma/dt$ in the elastic cross sections. . .	13
2.6. Experimental values used in calculating the interaction likelihood $\sigma_T/N_T$ . . . . .	15
2.7. Event type hypotheses . . . . .	16
2.8. The number of events in this experiment . .	19
2.9a. Slowest positive track project momentum characteristics (for the events shown in Figures 2.2 and 2.3). . . . .	28
2.9b. Characteristics of the projected momentum distribution for the slowest positive track (for events shown in Figure 2.4). .	28
2.10. Probability that the measurer will measure a particular $\bar{p}p$ type event on the basis of the scanning criteria . . . . .	34
2.11a. Contamination from the $\bar{p}p$ type reactions in the 4-prong sample in millibarns. . . .	35



Table

2.11b. Contam  
6 pr

2.12. The  $\bar{p}d$   
sect

2.13.  $\bar{p}n$  top  
scree

2.14. The ind

2.15a. The num  
Psp +  
cross

2.15b. The num  
Psp +  
cross  
cut

3.1. Sample

3.2. Resonance  
 $\pi \pi$

3.3a.  $\alpha_p$  and  
1.09

3.3b. The  $\rho^0$   
cross  
of 1

4.1. Invari

4.2. Averag

4.3. The di

4.4. The co  
para  
line

5.1. Spin s

6.1. Values

6.2. Perce  
the  
num

Table	Page
2.11b. Contamination from the $\bar{p}p$ type reactions in the 6 prong sample in millibarns . . . . .	36
2.12. The $\bar{p}d \rightarrow p_{sp} + \dots$ topological cross sections. . . . .	41
2.13. $\bar{p}n$ topological cross section and the screening factor . . . . .	41
2.14. The initial contamination of the data. . . . .	42
2.15a. The number of events accepted as the $\bar{p}d \rightarrow p_{sp} + \pi^+ \pi^- \pi^-$ reaction, and the corresponding cross section with the fiducial volume cut . . . . .	48
2.15b. The number of events accepted as the $\bar{p}d \rightarrow p_{sp} + \pi^+ \pi^- \pi^-$ reaction, and the corresponding cross section without the fiducial volume cut . . . . .	48
3.1. Sample count . . . . .	57
3.2. Resonance parameters for the reaction $\bar{p}n \rightarrow \pi^+ \pi^- \pi^-$ from 1.09 to 1.43 GeV/c . . . . .	58
3.3a. $\alpha_\rho$ and $\alpha_f$ values for $\bar{p}n \rightarrow \pi^+ \pi^- \pi^-$ for momenta 1.09, 1.19, 1.31 and 1.43 GeV/c . . . . .	59
3.3b. The $\rho^0$ , $\pi^-$ , $f^0$ , $\pi^-$ ; and $\pi^+ \pi^- \pi^-$ statistical cross sections for the momentum range of 1.09 to 1.43 GeV/c . . . . .	60
4.1. Invariant mass cuts. . . . .	74
4.2. Average differential cross sections . . . . .	76
4.3. The differential cross section parameters . . . . .	80
4.4. The comparison of the intercept and slope parameters from this experiment with its line reversed reaction . . . . .	82
5.1. Spin state composition of the $\bar{p}n$ system . . . . .	90
6.1. Values of the $\rho$ trajectory parameters. . . . .	106
6.2. Percentages of each spin parity state and N, the ratio of the fitted to the total number of events . . . . .	108

Table	Page
A-1-A. Definition of the scan code numbers . . .	122
A-1-B. Classification of major and minor errors .	123
A-2. Results of code number count for the three and five prong events . . . . .	124
A-3. Results of the code number count for the four and six prong events . . . . .	126
B-1. The total number of passed events is given in Table B-1-A; and total number of failed events is given in Table B-1-B. .	132
B-2. The measurement efficiencies for the entire sample . . . . .	133
B-3. Events in measured sample which were unwanted quantified in terms of percentage of the total sample. . . . .	133
D-1. Beam count results. . . . .	141
D-2. Summary of the track count . . . . .	145

Figure

2.1. A typ

2.2a. 1068

2.2b. 1143

2.3a. 413 6-

2.3b. 530 6-

2.4. Project  
slow  
4 P

2.5a. Probab  
spec  
will  
spec

2.5b. Monte  
pro  
Mark

2.6a. Probab  
spec  
will  
spec

2.6b. Monte  
 $\pi^+$  n

2.7. The  $\bar{p}$   
cross  
inte

## LIST OF FIGURES

Figure	Page
2.1. A typical bubble chamber picture . . . . .	5
2.2a. 1068 4-Prong events . . . . .	22
2.2b. 1143 4-Prong events . . . . .	22
2.3a. 413 6-Prong events. . . . .	24
2.3b. 530 6-Prong events. . . . .	24
2.4. Projected momentum distributions for the slowest positive track for a sample of 4 Prong events . . . . .	27
2.5a. Probability that a positive pion with a spectator neutron from a four prong event will be mistakenly measured as a spectator proton. . . . .	30
2.5b. Monte Carlo prediction for the slowest projected $\pi^+$ momentum distribution for Mark 16. . . . .	30
2.6a. Probability that a positive pion with a spectator neutron from a six prong event will be mistakenly measured as a spectator proton. . . . .	32
2.6b. Monte Carlo prediction for the slowest projected $\pi^+$ momentum distribution for Mark 16 . . . . .	32
2.7. The $\bar{p}d \rightarrow 3, 4, 5$ and 6 prong topological cross section arising from the $\bar{p}n$ interaction . . . . .	38

Figure

2.8. The p  
sec  
the

2.9. Charac  
acce  
r

2.10. Charac  
acce

2.11. The p  
comp  
East

3.1. The -  
reac

3.2. Charac  
acce  
pn

3.3. The w  
GeV

3.4. The r  
wit

4.1. The e  
for

4.2. Diffe

4.3. The d

4.4. Reson

4.5. The

5.1. The  
cr

6.1. Grou  
s(  
on

Figure	Page
2.8. The $\bar{p}n$ 3 and 5 prong topological cross section compared with the prediction of the impulse approximation . . . . .	40
2.9. Characteristics of events satisfying initial acceptance criteria for the $\bar{p}d \rightarrow p_{sp} + \pi^+ \pi^- \pi^-$ reactions . . . . .	44
2.10. Characteristics of events satisfying final acceptance criteria for the $\bar{p}d \rightarrow p_{sp} + \pi^+ \pi^- \pi^-$ reaction . . . . .	47
2.11. The $\bar{p}n \rightarrow \pi^+ \pi^- \pi^-$ reaction cross section compared to the results published by Eastman, et al. . . . .	50
3.1. The $\pi^+ \pi^-$ invariant mass distribution for the reaction $\bar{p}d \rightarrow p_{sp} + \pi^+ \pi^- \pi^-$ . . . . .	53
3.2. Characteristic of events satisfying final acceptance criteria for the reaction $\bar{p}n \rightarrow \pi^+ \pi^- \pi^-$ . . . . .	56
3.3. The $\pi^+ \pi^-$ invariant mass distribution at 1.31 GeV/c. . . . .	62
3.4. The resonant cross section and comparison with higher momentum data . . . . .	65
4.1. The elementary baryon exchange diagrams for the processes listed below . . . . .	68
4.2. Differential distributions . . . . .	73
4.3. The definition for $\theta$ in the c.m. frame . . . . .	74
4.4. Resonance region and control band regions . . . . .	75
4.5. The average differential cross section . . . . .	78
5.1. The resonance produced differential cross section . . . . .	89
6.1. Group 1 data for (A) The Dalitz plot of $s(\pi^+ \pi_1^-)$ vs $s(\pi^+ \pi_2^-)$ ; (b) The projection onto the mass squared axis. . . . .	102

Figure

6.2. Sample  
s( $\pi$ )  
onto

6.3. The co  
data  
the

6.4. Dalitz  
samp  
betw

6.5. The co  
data  
Dali

6.6. Dalitz  
samp  
betw

C.1. Vertex  
respe

C.2. Geomet  
radi

D.1. Vertex



Figure	Page
6.2. Sample 2 data for (A) The Dalitz plot of $s(\pi^+\pi^-)$ vs $s(\pi^+\pi^-)$ ; (B) The projection onto the mass squared axis . . . . .	105
6.3. The comparison of the Veneziano fit to the data in sample 1 for slices across the Dalitz plot. . . . .	110
6.4. Dalitz plot for the Veneziano Model fit for sample 1 for (A) The absolute deviation between the model; (B) The Fit. . . . .	112
6.5. The comparison of the Veneziano fit to the data in sample 2 for slices across the Dalitz plot . . . . .	114
6.6. Dalitz plot of the Veneziano Model fit for sample 2 for (A) The absolute deviation between the model; (B) The fit. . . . .	116
C.1. Vertex position of all measured events with respect to the fiducial volume. . . . .	137
C.2. Geometric picture of a circle with the same radius of curvature as the beam . . . . .	139
D.1. Vertex position for all measured events . . . . .	146

In h  
fundamental  
action can b  
scattering i  
using the so  
scattering a  
interaction  
and applicab  
ing a symmet  
endowment of  
ideas should  
region of th  
dynamical id  
is sometimes  
the intuitiv

One

ing symmetry  
principle is  
ically simpl  
experimental

## CHAPTER I

### INTRODUCTION

In high energy physics one yearns to discover the fundamental principles by which elementary particle interaction can be explained, or at least classified. Where scattering is concerned these principles may be quantified using the scattering amplitude formalism. Ideally a scattering amplitude not only represents the dynamical interaction but also is assumed to implicitly obey known and applicable symmetry principles. The basis for accepting a symmetry idea can sometimes be intuitive. The endowment of the scattering amplitude with these intuitive ideas should be experimentally tested with respect to the region of their applicability. Experimental tests of the dynamical ideas are no less important, but in reality it is sometimes difficult to obtain a clear separation between the intuitive and dynamical ideas.

One such idea is the familiar principle of crossing symmetry. Though the theoretical implication of this principle is clear, sometimes one must invoke theoretically simplifying ideas in order that comparison with experimental data may be made. In this work we have used

the reaction

$\bar{p} + p \rightarrow p^0 n$  for

Another

the duality

dualistic Ve

the  $\bar{p} n \rightarrow \pi^+ -$

compare the

Veneziano mo

of the  $\bar{p} n$  sy

Veneziano mo

A ma

obtained from

Laboratory 31

beam of antip

GeV/c. This

reels of film

using the 30-

National Labor

published else

Most o

from which top

sections were

sis as mention

sively in the

prises about o

the reaction  $\bar{p}n \rightarrow \rho^0\pi^-$  and its crossed channel reaction  $\pi^-p \rightarrow \rho^0n$  for such a study.

Another idea that emanates from the connection of the duality principle with strong interaction is the dualistic Veneziano<sup>1</sup> model, and its novel application<sup>2</sup> to the  $\bar{p}n \rightarrow \pi^+\pi^-\pi^-$  reaction. The Dalitz plot is used here to compare the data with the prediction of the spin modified Veneziano model. In addition, the spin state composition of the  $\bar{p}n$  system was determined separately from the Veneziano model comparison.

A major portion of the data for this study was obtained from an exposure of the Brookhaven National Laboratory 31-inch deuterium bubble chamber to an incident beam of antiprotons of momenta 1.09, 1.19, 1.31 and 1.43 GeV/c. This resulted in a total of 150,000 triads on 72 reels of film. The remaining sample of events was obtained using the 30-inch deuterium bubble chamber at the Argonne National Laboratory. Details for these data have been published elsewhere.<sup>3</sup>

Most of this work deals with the Brookhaven data, from which topological, reaction and resonance cross sections were obtained in addition to the dynamical analysis as mentioned before. The Argonne data is used exclusively in the dynamics analysis, and in this capacity comprises about out third of the total sample.

## CHAPTER II

### CROSS SECTION MEASUREMENTS

#### 2.1 Scanning and Corrections

The 72 reels of film from the Brookhaven exposure were scanned for all three and five prong events, plus those four and six prong events with an obvious spectator proton track. By being obvious here one means that a track must be at least twice minimum ionizing in any of the three views. An event that fell in the above mentioned category was measured if its interaction vertex was visible in all three views and within the measurement region, as shown in Figure 2.1. The subjective part of the event selection begins here, because the final measured sample contained only those events which the measurer felt belonged in the above mentioned category. Therefore in reality the aspired sample can never be completely obtained. In this manner a total of 37,716, 49,030, 17,808 and 16,845 events were found in the 3, 4, 5 and 6 prong topologies respectively.

In order to determine the total number of events that occurred in the sample, one must know how many events were not recorded correctly, or not recorded at



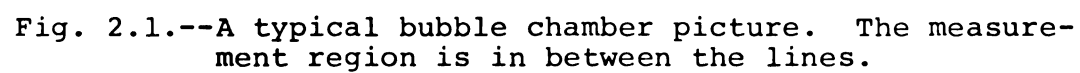
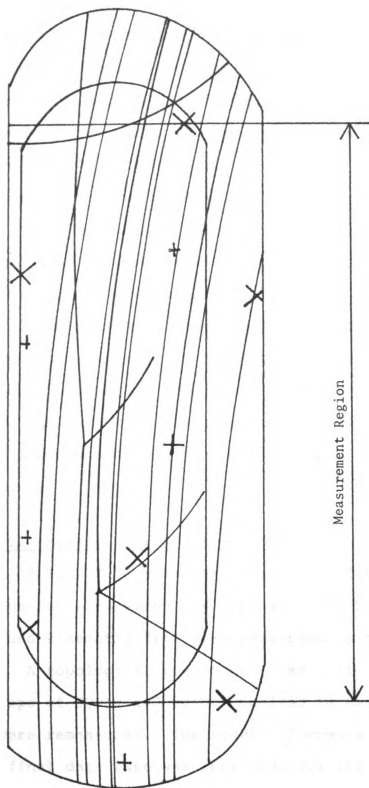


Fig. 2.1.--A typical bubble chamber picture. The measurement region is in between the lines.





all by the  
independent  
losses of e  
missing in  
knows the n  
independent

A sa  
second scan  
distributed  
this sample  
calculated.  
first and se  
scan table a  
scanner. A  
calculating  
is given in

A to  
track informa  
program TVGP,  
program SQUAW  
on the output  
TVGP or SQUAW  
counted on th  
measurement i

all by the scanner. One way to do this is to perform an independent second scan of the sample. Assume that the losses of events in both scans are random, the number missing in a particular sample can be calculated if one knows the number found in common and separately from two independent scans of the sample.

A sample of 12 out of the total of 72 rolls were second scanned. These rolls were randomly and evenly distributed among the four beam momenta. All events in this sample were analyzed and scanning efficiencies were calculated. In the case of a discrepancy between the first and second scan, the event was reprojected onto the scan table and was examined and classified by a third scanner. A full explanation of the details involved in calculating the scanning efficiencies list in Table 2.1 is given in Appendix A.

## 2.2 Measuring and Corrections

A total of 121,399 events were measured. The track information for each event was reconstructed by the program TVGP,<sup>4</sup> and kinematic fits were performed by the program SQUAW.<sup>5</sup> A topological event count was performed on the output tape of SQUAW and events failing to pass TVGP or SQUAW were remeasured. The number of events counted on the final data tape was corrected for its measurement inefficiencies which are shown in Table 2.2.



Table 2.1.--The scanning efficiency, given in terms of percentage of correct events.

Momentum (GeV/c)	3-Prong	4-Prong	5-Prong	6-Prong
1.09	.901 $\pm$ .0065	.855 $\pm$ .0102	.901 $\pm$ .0065	.877 $\pm$ .0163
1.19	.871 $\pm$ .0061	.855 $\pm$ .0088	.871 $\pm$ .0061	.857 $\pm$ .0138
1.31	.872 $\pm$ .0058	.833 $\pm$ .0089	.872 $\pm$ .0058	.862 $\pm$ .0132
1.43	.883 $\pm$ .0048	.840 $\pm$ .0071	.883 $\pm$ .0048	.865 $\pm$ .0110

Table 2.2.

Momentum  
(GeV/c)

1.09

1.19

1.31

1.43

The detail  
are discuss

The  
determinat  
action reg  
for the sc  
location i  
observed e  
the trackl  
volume by  
region.

To  
that has t  
through ea  
The actual

Table 2.2.--Measurement efficiencies for the  $\bar{p}d \rightarrow p_{sp} + \dots$  topological cross section.

Momentum (GeV/c)	3-Prong	4-Prong	5-Prong	6-Prong
1.09	.938	.929	.912	.883
1.19	.957	.930	.916	.870
1.31	.947	.937	.908	.884
1.43	.956	.941	.916	.880

The details of the measurement efficiency calculations are discussed in Appendix B.

### 2.3 Fiducial Volume Length

The target thickness that enters into cross section determinations is the average path length of the interaction region. Since the measurement region is demarcated for the scanner by visual marks on the film, its precise location is unclear. In order to insure that every observed event was recorded within the region over which the tracklength is calculated, one defines a fiducial volume by considering a sub-zone inside the measurement region.

To calculate the fiducial volume length, an arc that has the same curvature as the beam is constructed through each measured vertex within the fiducial volume. The actual length of the beam track for that vertex is

the length  
boundary.

A  
in the fi  
gives the

Table 2.3

---

Labor

---

---

In  
one must kn  
In this exp  
all reels u  
scaled up t  
total numbe  
details are



the length of the arc lying within the fiducial volume boundary.

Appendix C explains the geometrical ideas involved in the fiducial volume length determination. Table 2.3 gives the average tracklength for each momentum.

Table 2.3.--The average tracklength of the incident beam particles.

Laboratory Momentum (GeV/c)	Tracklength (cm)
1.09	41.9 $\pm$ .5
1.19	41.9 $\pm$ .5
1.31	41.7 $\pm$ .5
1.43	41.8 $\pm$ .5

#### 2.4 Track Count

In order to calculate an experimental cross section one must know how many particles are incident on the target. In this experiment a count of beam tracks was taken over all reels using every 50th frame. The results are then scaled up to the total number of frames measured. The total numbers of beams are listed in Table 2.4 and the details are given in Appendix D.

Table 2.4.--

Moment
1
1
1
1

The  
of lb per ev  
event. This  
track count,  
is determine  
section for  
of events is

If t  
of length L  
the total cr  
total number

where  $A_0$  is  
$$1 - e^{-\frac{A_0}{2} L}$$
  
particles t

Table 2.4.--The number of beam tracks entering the fiducial volume.

Momentum (GeV/c)	Total number of beam
1.09	168664
1.19	258432
1.31	497598
1.43	330805

### 2.5 The Interaction Likelihood

The interaction likelihood, expressed in units of  $\mu\text{b}$  per event, is the cross section equivalent of an event. This ratio depends on the fiducial volume length, track count, and the total cross section. Once this ratio is determined for a particular experiment, the cross section for any event type can be calculated if the number of events is known.

If there are  $N_{TK}$  tracks entering a fiducial volume of length  $L$  of a liquid deuterium target of density  $\rho$ , and the total cross section for interaction is  $\sigma_T$ , then the total number of interactions  $N_T$  is given by

$$N_T = N_{TK} \left(1 - e^{-\frac{A_0}{2} \rho L \sigma_T}\right) \quad (2.1)$$

where  $A_0$  is the Avagadroe number and the factor

$\left(1 - e^{-\frac{A_0}{2} \rho L \sigma_T}\right)$  represents the fraction of the incident particles that will interact.

The

2.

A ty

incident bea

ing of the t

to it by the

more obvious

in the beam

mine losses

able stub len

From

estimated the

tains two bul

$.076 \pm .025$  c

$.076 \pm .025$  c

The m

related to th

$\frac{M_D}{M_P} R_P(P_P)$  whe

$\frac{M_D}{M_P}$  and moment

with mass  $M_D$ .

at  $P_D = \frac{M_D}{M_P} P_P$

with a range

with a range

The interaction likelihood is given by

$$\frac{\sigma_T}{N_T} = \frac{\sigma_T}{N_{TK} (1 - e^{-\rho \frac{A_0}{2} L \sigma_T})} \quad (2.2)$$

### 2.5.1 Corrections for Unseen Elastics

A typical elastic event shows a slight kink on the incident beam track and a small stub indicating the recoiling of the target particle due to the momentum transferred to it by the beam. It is observed that a small stub is a more obvious signature of elastic scattering than a kink in the beam track. Therefore, it is more logical to determine losses in elastic events based on a minimum observable stub length criterion.

From the stub size measurements, it has been estimated the minimum stub length that can be seen contains two bubbles, which corresponds to a length of  $.076 \pm .025$  cm in space. A proton with a range of  $.076 \pm .025$  cm has a momentum of  $70 \pm 8$  mev/c.

The momentum of a deuteron with a given range is related to that of a proton by the scaling law  $R_D (P_D) = \frac{M_D}{M_P} R_P (P_P)$  where  $R_P$  is the range of the proton with mass  $M_P$  and momentum  $P_P$ , and  $R_D$  is the range of the deuteron with mass  $M_D$ . The momentum of the deuteron  $P_D$  is taken at  $P_D = \frac{M_D}{M_P} P_P$ . Therefore the momentum of the deuteron with a range of  $.076 \pm .025$  cm is twice that of a proton with a range of  $.038 \pm .012$  cm. This gives a cutoff

momentum for

ponding val

-0.0049 +.0001  
-.0001

for deuteron

The

obtained fro

missing =

where s is t

Chapter 2.6.2

momentum targ

camera view a

cutoff.

The  $\sigma$  (u

lating the am

less than  $8^\circ$

spectator pro

The d

eterized by d

(t=0) and b a

compilation b

extrapolation

experiment, 1

Table 2.5.

momentum for the deuteron of  $112^{+8}_{-10}$  MeV/c. The corresponding values for the momentum transfer squared  $t$  are  $-.0049^{+.0007}_{-.0011}$  GeV<sup>2</sup>/c<sup>2</sup> for protons and  $-.0125^{+.0019}_{-.0024}$  GeV<sup>2</sup>/c<sup>2</sup> for deuterons.

The total missing elastic cross section can be obtained from the expression:

$$\sigma_{\text{missing}} = \int_0^{t_D} \frac{d\sigma}{dt} (\bar{p}d \text{ elastic } dt + \frac{1}{8} \int_0^{t_p} \frac{d\sigma}{dt} (\bar{p}p \text{ elastic}) dt + \sigma(\text{unseen } \bar{p}n \text{ elastic}) \quad (2.3)$$

where  $s$  is the screening correction as explained in Chapter 2.6.2. This expression must be corrected for high momentum target recoils which are not in the plane of the camera view and have apparent lengths less than the .076 cm cutoff.

The  $\sigma$  (unseen  $\bar{p}n$  elastic) was determined by estimating the amount of  $\bar{p}n$  elastic cross section with kinks less than  $8^\circ$  in the laboratory, and without a visible spectator proton track.

The differential cross sections  $d_\sigma/dt$  are parameterized by  $d_\sigma/dt (t=0) e^{-bt}$  where the parameters  $d_\sigma/dt (t=0)$  and  $b$  are obtained from Ma, et al.,<sup>6</sup> and from a compilation by the Particle Data Group.<sup>7</sup> Using a linear extrapolation of these data to the mean momentum of this experiment, 1.27 GeV/c, one obtains the results given in Table 2.5.

Table 2.5.--

Target Parti

Neutron

Proton

Deuteron

Using these

A correc

done for stub

corresponds t

and up to .00

ranges of .07

a projected 1

1.0 percent in

missing elasti

stubs was dete

momentum event

unobserved ela

section is 31+



Table 2.5.--The intercept and slope parameters for  $d\sigma/dt$  in the elastic cross sections.

Target Particle	$d\sigma/dt$ ( $t=0$ ) mb/(GeV/c) <sup>2</sup>	$\cdot b(\text{GeV/c})^{-2}$
Neutron	617 $\pm$ 27	14.2 $\pm$ .6
Proton	617 $\pm$ 27	14.2 $\pm$ .6
Deuteron	1700 $\pm$ 200	44. $\pm$ 2.

Using these values and equation (2.3) one obtains

$$\sigma_{\text{missing}} = 27^{+6}_{-7} \text{ mb} \quad (2.4)$$

A correction for stubs not on the film plane was done for stub lengths from .076 cm to .167 cm. This corresponds to  $t$  values up to .02 GeV<sup>2</sup>/c<sup>2</sup> for the deuteron and up to .008 GeV<sup>2</sup>/c<sup>2</sup> for the proton. For stub length ranges of .077 cm to .167 cm the percent of the stub with a projected length less than .077 cm was calculated for 1.0 percent increment of increased stub lengths. The missing elastic cross section for each  $t$  bin due to short stubs was determined and then summed. The higher recoil momentum events yield an additional 4 mb loss to the unobserved elastic events. The final unseen elastic cross section is  $31^{+7}_{-8}$  mb.

Alt  
events is t  
lengthen th  
unseen part  
tribution t  
this amount  
the effecti

Usi  
recting for  
count line a  
Appendix D c

To d  
 $S_T/N_T$  with r  
rection, one  
section is p  
1.6%.

## 2.6

After  
TVGP, the SQ  
to the event  
the best fit  
is suggested.  
uncertainties  
rect hypotheses

### 2.5.2 The Interaction Likelihood Calculation

Although the direct effect of unseen elastic events is to raise the number of recorded events and to lengthen the fiducial volume, one may reason that this unseen part of the elastic cross section makes no contribution to this experiment. If one therefore subtracts this amount from the  $\bar{p}d$  total cross section, one obtains the effective total cross section for this experiment.

Using the effective total cross section and correcting for the attenuation of the beam between the beam count line and the fiducial volume line as explained in Appendix D one obtains the results given in Table 2.6.

To determine the sensitivity of the quantity  $\sigma_T/N_T$  with respect to the unseen elastic scattering correction, one notes that if 50 mb of unseen elastic cross section is proposed, the value of  $\sigma_T/N_T$  changes by only 1.6%.

## 2.6 Topological and Reaction Cross Section

After each event is measured and processed through TVGP, the SQUAW program performs kinematic fits according to the event type hypothesis listed in Table 2.7. Ideally the best fit will be obtained when the correct hypothesis is suggested. In reality the systematic and statistical uncertainties in the track information may cause an incorrect hypothesis to have a better fit according to objective

Table 2.6.---Experimental values used in calculating the interaction likelihood  $\sigma_T/N_T$ . The quantity  $\sigma_T$  is equal to the  $\bar{p}d$  total cross section  $\sigma_T(\bar{p}d)$  less the unseen elastic cross section ( $\sigma_{\text{missing}}$ ).

Momentum (GeV/c)	$\sigma_T(\bar{p}d)$ (mb)	$\sigma_T = \sigma_T(\bar{p}d) - \sigma_{\text{missing}}$ (mb)	Number of tracks entering the fiducial volume	Tracklength (cm)	$-\rho \frac{A}{2} \sigma_T$ l-e Probability of interaction	$\sigma_T/N_T$ Interaction likelihood $\mu/\text{event}$
1.09	200.5	$169.5 \pm 24$	168664	$41.9 \pm .5$	.258	$3.90 \pm .075$
1.19	195.6	$164.6 \pm 24$	258432	$41.9 \pm .5$	.254	$2.52 \pm .049$
1.31	191.2	$160.2 \pm 24$	<b>497598</b>	$41.7 \pm .5$	.246	$1.30 \pm .025$
1.43	184.6	$153.6 \pm 24$	330805	$41.8 \pm .5$	.240	$1.94 \pm .039$

Table 2.7.-

Topology

3

4

5

Table 2.7.--Event type hypotheses.

Topology	Reaction	Mark number
3	$\bar{p}d \rightarrow p_{sp} p \bar{p} \pi^-$	3
	$\bar{p}d \rightarrow p_{sp} p \bar{p} \pi^- MM$	5
	$\bar{p}d \rightarrow p_{sp} \pi^+ \pi^- \pi^-$	8
	$\bar{p}d \rightarrow p_{sp} \pi^+ \pi^- \pi^- \pi^0$	9
	$\bar{p}d \rightarrow p_{sp} \pi^+ \pi^- \pi^- MM$	10
	$\bar{p}d \rightarrow p_{sp} K^+ K^- \pi^-$	30
	$\bar{p}d \rightarrow p_{sp} K^+ K^- \pi^- MM$	31
4	$\bar{p}d \rightarrow p p \bar{p} \pi^-$	3
	$\bar{p}d \rightarrow p p \bar{p} \pi^- MM$	5
	$\bar{p}d \rightarrow p \pi^+ \pi^- \pi^-$	8
	$\bar{p}d \rightarrow p \pi^+ \pi^- \pi^- \pi^0$	9
	$\bar{p}d \rightarrow p \pi^+ \pi^- \pi^- MM$	10
	$\bar{p}d \rightarrow N \pi^+ \pi^+ \pi^- \pi^-$	16
	$\bar{p}d \rightarrow \pi^+ \pi^+ \pi^- \pi^- MM$	17
	$\bar{p}d \rightarrow p K^+ K^- \pi^-$	30
	$\bar{p}d \rightarrow p K^+ K^- \pi^- MM$	31
5	$\bar{p}d \rightarrow p_{sp} \pi^+ \pi^+ \pi^- \pi^- \pi^-$	8
	$\bar{p}d \rightarrow p_{sp} \pi^+ \pi^+ \pi^- \pi^- \pi^- \pi^0$	9
	$\bar{p}d \rightarrow p_{sp} \pi^+ \pi^+ \pi^- \pi^- \pi^- MM$	10
	$\bar{p}d \rightarrow p_{sp} K^+ K^- \pi^+ \pi^- \pi^-$	30
	$\bar{p}d \rightarrow p_{sp} K^+ K^- \pi^+ \pi^- \pi^- MM$	31

Table 2.7.--Continued.

Topology	Reaction	Mark number
6	$\bar{p}d \rightarrow p\pi^+\pi^+\pi^-\pi^-\pi^-$	8
	$\bar{p}d \rightarrow p\pi^+\pi^+\pi^-\pi^-\pi^-\pi^0$	9
	$\bar{p}d \rightarrow p\pi^+\pi^+\pi^-\pi^-\pi^-\text{MM}$	10
	$\bar{p}d \rightarrow n\pi^+\pi^+\pi^+\pi^-\pi^-\pi^-$	16
	$\bar{p}d \rightarrow \pi^+\pi^+\pi^+\pi^-\pi^-\pi^-\text{MM}$	17
	$\bar{p}d \rightarrow pK^+K^-\pi^+\pi^-\pi^-$	30
	$\bar{p}d \rightarrow pK^+K^-\pi^+\pi^-\pi^-\text{MM}$	31

statistic

therefore

well as

If these

final sam

1

required

$10^{-4}$ . In

two stand

case of m

were invo

S

interacti

obtained

Because o

the twice

procedure

correctio

the  $\hat{p}_d \rightarrow$

I

fiducial

prong eve

contamina



statistical tests. In order to obtain a pure sample one therefore imposes acceptance criteria based on physics, as well as statistical tests on all events in a desired sample. If these criteria are too stringent one must correct the final sample for the loss of good events.

In this experiment an acceptable hypothesis was required to achieve a confidence level of greater than  $10^{-4}$ . In addition, the missing mass square must be within two standard deviations of the expected value. In the case of multiple fits, additional kinematic constraints were invoked to determine the correct hypothesis.

Since the goal of this experiment is to study  $\bar{p}n$  interactions the 4 and 6 prong events should have been obtained due to the presence of a spectator proton. Because of the uncertainty in calling a proton track by the twice minimum ionization criterion in the measuring procedure, as discussed in Chapter 2.1, a significant correction has to be performed to eliminate events from the  $\bar{p}d \rightarrow N_{sp} + 4$  or 6 prong final states.

In Table 2.8 the raw topological count within the fiducial volume at each momentum is given. The 4 and 6 prong events are completely uncorrected for any  $n_{sp}$  contaminations.

Table 2.8.--The number of events in this experiment. The even prongs include contaminations from  $\bar{p}p$  reaction products. The fiducial volume cut as discussed in Chapter 2.3 has been invoked.

Momentum (GeV/c)	#3 Prong	#4 Prong	#5 Prong	#6 Prong
1.09	3861	5289	1780	1495
1.19	5836	7381	2638	2208
1.31	10699	13533	4990	4262
1.43	7303	9364	3282	2784

#### 2.6.1 Separation of $\bar{p}p$ Contaminations

One consequence of the deuteron double scattering process<sup>8</sup> is the production of very high momentum spectator protons. In this work, an attempt was made to measure the complete sample of these spectators.

If a sample of  $\bar{p}n$  events with high momentum spectator protons are examined on a scan table, one would see that in many cases these events appear very similar to those from  $\bar{p}p$  annihilations. This similarity resulted in a significant contamination from  $\bar{p}p$  interactions. The analysis discussed in this section deals with the events in this ambiguous region.

In the 4 prong sample the most common type of track misinterpretation was due to scanners misjudging one of the positive pion tracks from the reactions  $\bar{p}d \rightarrow n_{sp} + 2\pi^+ 2\pi^- + k(\pi^0)$  as a spectator proton track,

thus meas  
between t  
many of t  
events.

track ion  
of contam

I  
tion of t  
is a sign  
(called M  
independe

2.3 the p  
events th

Here the  
to the io

this was

A  
that alth  
criteria,  
lower mom

than do t  
minimum i  
200 MeV/c  
GeV/c.

To  
true Mark

thus measuring the event. Due to kinematic ambiguities between the above reactions and  $\bar{p}d \rightarrow p_{sp} + \pi^+ 2\pi^- + k(\pi^0)$  many of the  $\bar{p}p$  events were incorrectly classified as  $\bar{p}n$  events. This meant that a quantitative analysis based on track ionizations had to be made to determine the amount of contaminations.

If one considers the projected momentum distribution of the slowest positive track it is found that there is a significant difference between  $\bar{p}d \rightarrow p_{sp} + \pi^+ 2\pi^- + \pi^0$  (called Mark 9) and  $\bar{p}d \rightarrow n_{sp} + 2\pi^+ 2\pi^-$  (called Mark 16), independent of kinematic information. In Figures 2.2 and 2.3 the projected momentum distributions are given for all events that are called Mark 16 by the acceptance criteria. Here the projected momentum is used because this is related to the ionization of the track as seen by the scanner, and this was used to determine if a measurement was to be made.

A statistical analysis of these distributions shows that although all were called Mark 16 by the acceptance criteria, the real Mark 16 events have on the average a lower momentum associated with the slowest positive track than do the  $\bar{p}n$  events. This is expected because the twice minimum ionizing criterion corresponds to a cutoff at about 200 MeV/c for a pion while the proton can have up to  $\sim 1$  GeV/c.

To determine the amount and characteristics of true Mark 16 candidates that were called Mark 9 by the

Fig. 2.2-A.--1068 4-Prong events. These events were correctly classified by the acceptance criteria as being  $\bar{p}d \rightarrow n_{sp} + 2\pi^+2\pi^-$ .

Fig. 2.2-B.--1143 4-Prong events. These events were classified as  $\bar{p}d \rightarrow n_{sp} + 2\pi^+2\pi^-$  by the acceptance criteria.<sup>sp</sup> After the ionization scan these events were found to be candidates for the reaction  $\bar{p}d \rightarrow p_{sp} + \pi^+2\pi^-\pi^0$ .

EVENTS/ 10. MEV/C  
90.  
60.  
30.  
0.

EVENTS/ 10. MEV/C  
60.  
30.  
0.

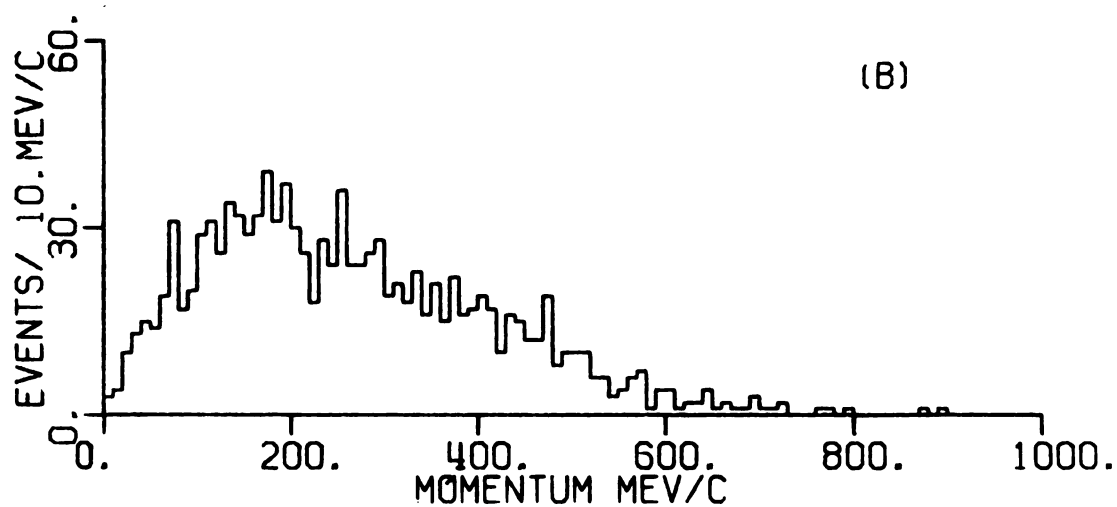
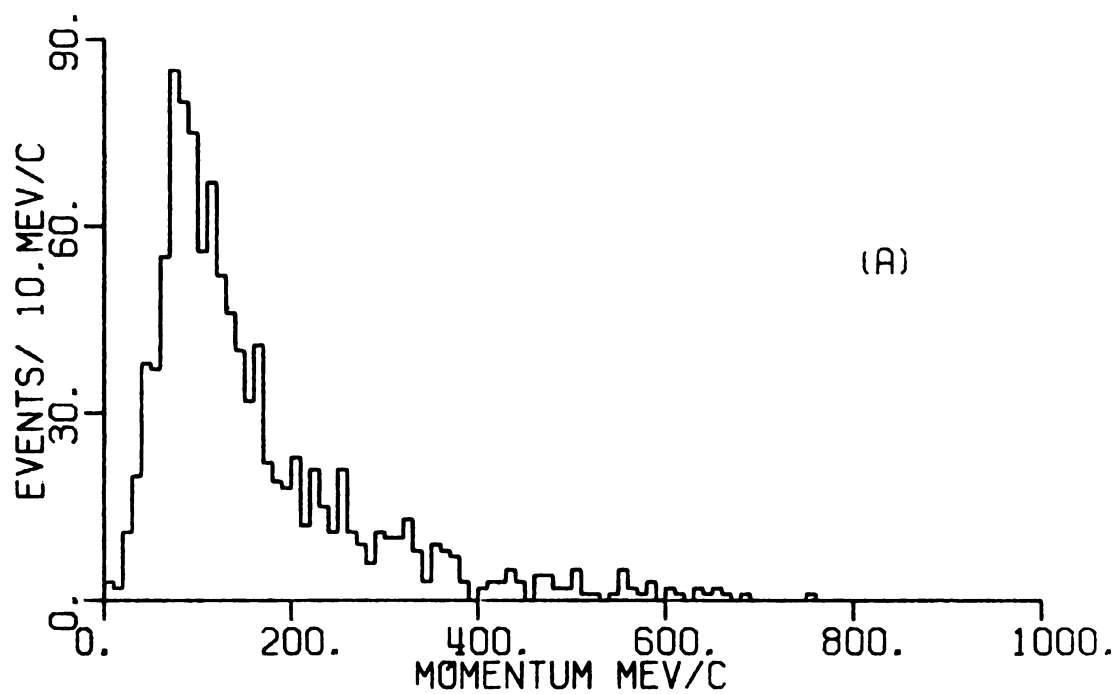
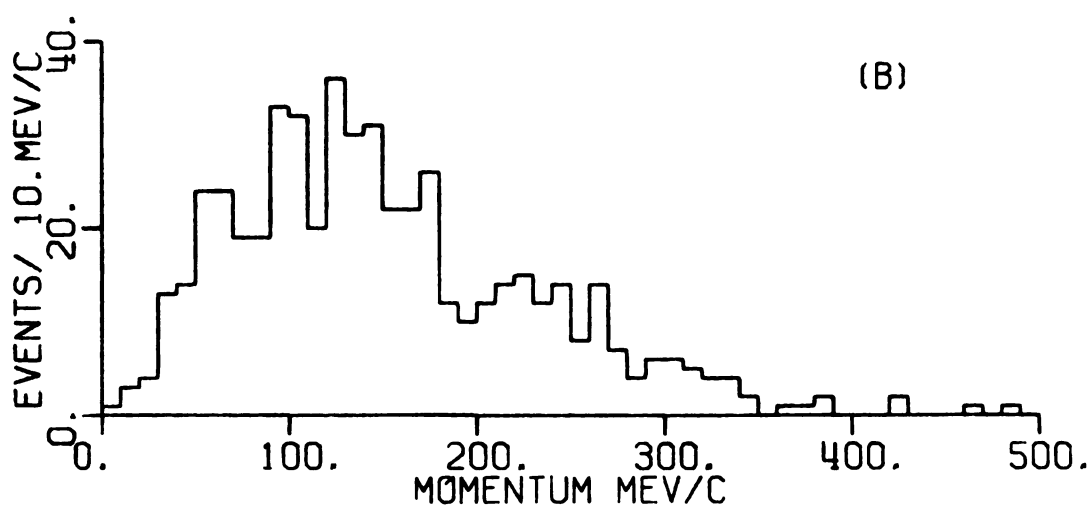
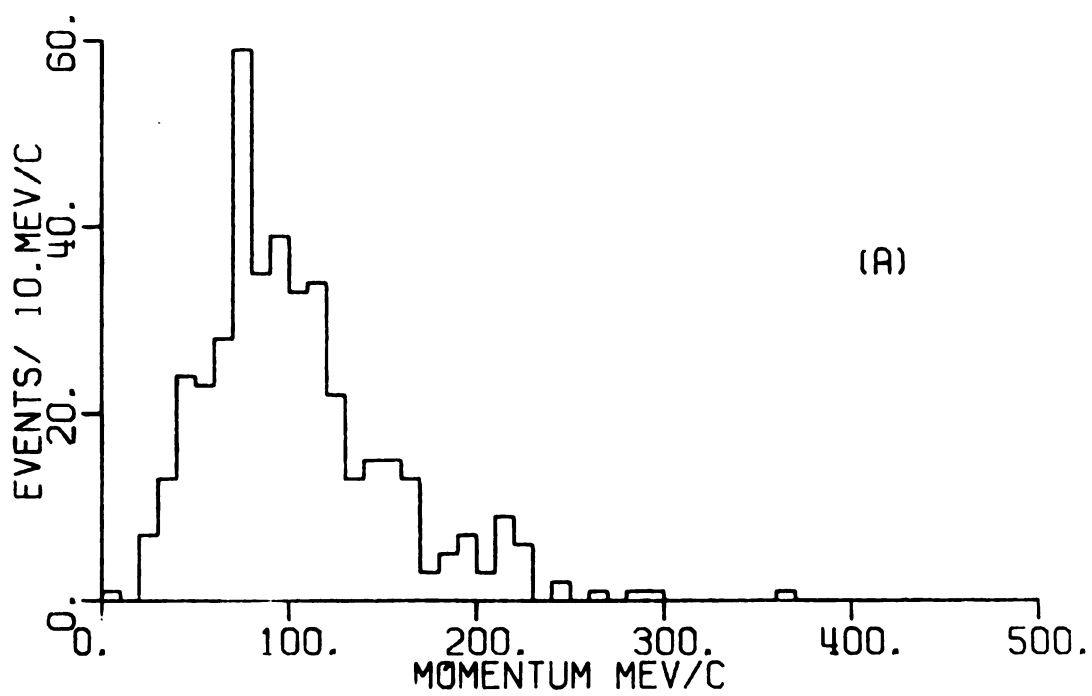


Fig. 2.3-A.--413 6-Prong events. These events were correctly classified by the acceptance criteria as being  $\bar{p}d \rightarrow n_{sp} + 3\pi^+3\pi^-$ .

Fig. 2.3-B.--530 6-Prong events. These events were classified as  $\bar{p}d \rightarrow n_{sp} + 3\pi^+3\pi^-$  by the acceptance criteria. After the ionization scan they were found to be candidates for the reaction  $\bar{p}d \rightarrow p_{sp} + 2\pi^+3\pi^-\pi^0$ .

EVENTS/10. MEV/C  
0. 20. 40. 60.

EVENTS/10. MEV/C  
0. 20. 40.





acceptan

sample)

scan tal

tance c

of the s

are not

is seen

of how

the  $\bar{p}n$

in Table

slowest

pared to

decays

shape f

is show

agreeme

satisfy

spectate

to the

higher

tion to

Probabil

Measured

acceptance criteria (the so-called "called 9 is 16" sample), a sample of 4 prong events was examined on the scan table irrespective of classification by the acceptance criterion.

In Figure 2.4 the projected momentum distributions of the slowest positive track are given. Although there are not as many events considered here, statistically it is seen that the  $\bar{p}p$  events have the same shape regardless of how the event was classified. This is also true for the  $\bar{p}n$  events. A complete statistical analysis is given in Table 2.9.

The projected momentum distribution for the slowest  $\pi^+$  from a clean sample of Mark 16 events is compared to the Monte Carlo prediction corrected for pion decays in the chamber. It is found that these agree in shape for momentum below 80 MeV/c. A comparison of this is shown in Figure 2.5-B and 2.6-B. One expects this agreement to occur since all pions with low momentum satisfy the twice minimum ionizing criterion for the spectators. The existence of high momentum pions is due to the fact that tracks with large dip angles have higher apparent ionizations.

The ratio of the experimental momentum distribution to that of the Monte Carlo prediction gives the probability that a pion of a given momentum will be measured. These ratios are shown in Figures 2.5-A and

Fig. 2.4.--Projected momentum distributions for the slowest positive track for a sample of 4 Prong events.

2.4-A Called 16 is 16

2.4-B Called 9 is 16

2.4-C Called 9 is 9

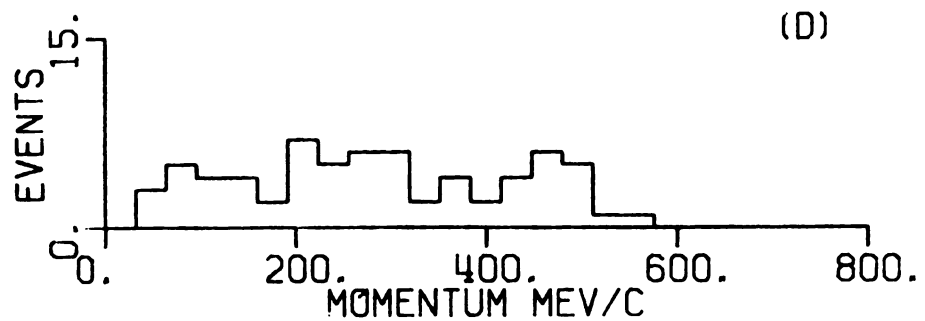
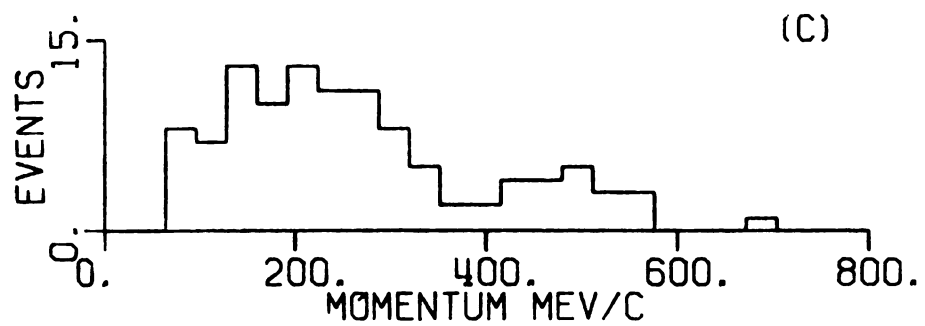
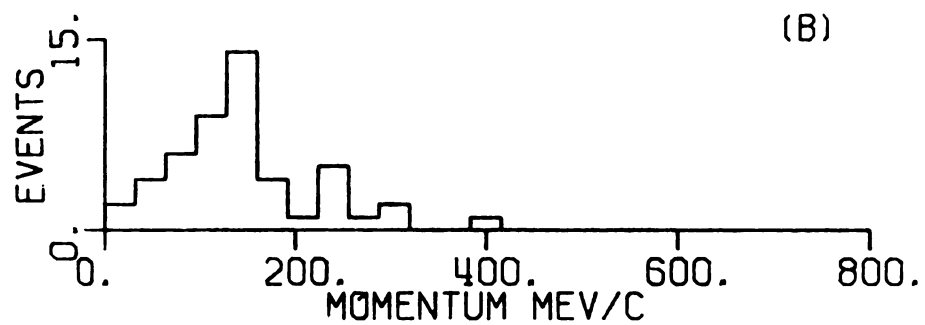
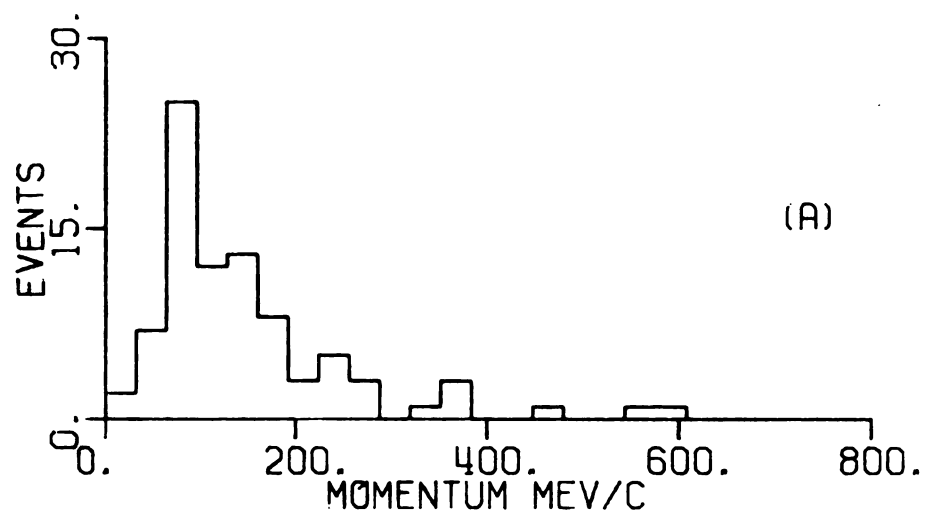
2.4-D Called 16 is 9

EVENTS  
30.  
15.  
0.

EVENTS  
15.  
0.

EVENTS  
15.  
0.

EVENTS  
15.  
0.



Table

---

Number  
<moment  
R.M.S.

---

Number  
<moment  
R.M.S.

---

Table

---

Number  
<moment  
R.M.S.

---

Number  
<moment  
R.M.S.

Table 2.9-A.--Slowest positive track projected momentum characteristics (for the events shown in Figures 2.2 and 2.3).

	Called 16 is 9	Called 16 is 16
Number 4 prong	1143	1068
<momentum> MeV/c	264. + 5.	160. + 4.
R.M.S. deviation	152. + 13.	119. + 10.
Number 6 prong	530	413
<momentum> MeV/c	152. + 4.	104. + 3.
R.M.S. deviation	81. + 11.	51. + 9.

Table 2.9-B.--Characteristics of the projected momentum distribution for the slowest positive track (for events shown in Figure 2.4).

	Called 9 is 9	Called 16 is 9	Called 16 is 16	Called 9 is 16
Number 4 prong	112	69	85	49
<momentum> MeV/c	272.+14.	289.+19	148.+ 12.	145.+10.
R.M.S. deviation	152.+44.	159.+56	107.+ 34.	76.+34.
Number 6 prong	66	40	27	6
<momentum> MeV/c	155.+11.	136.+11.	94.9+5.4	109.+16.
R.M.S. deviation	92.+38.	67.+34.	28. +27.	40.+65.

Fig. 2.5-A.--Probability that a positive pion with a spectator neutron from a four prong event will be mistakenly measured as a spectator proton.

Fig. 2.5-B.--Monte Carlo prediction for the slowest projected  $\pi^+$  momentum distribution for Mark 16. The shaded area represents that from the four prong data sample. The Monte Carlo distribution is normalized to the data below 80 MeV/c.

MOMENTUM BIAS

EVENTS/ 10 MEV/C

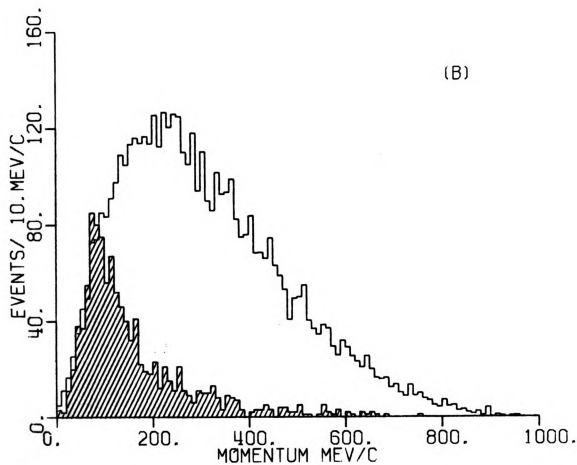
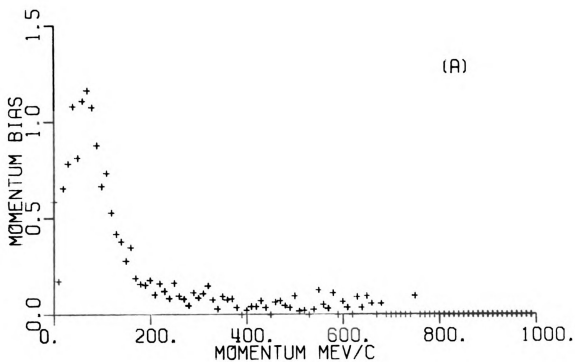




Fig. 2.6-A.--Probability that a positive pion with a spectator neutron from a six prong event will be mistakenly measured as a spectator proton.

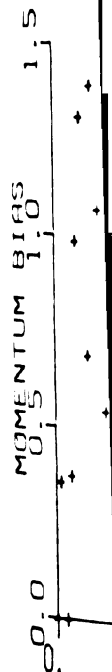
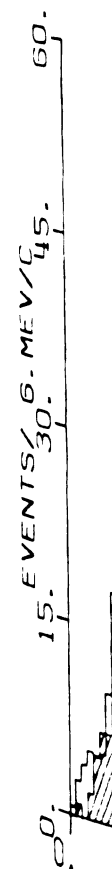
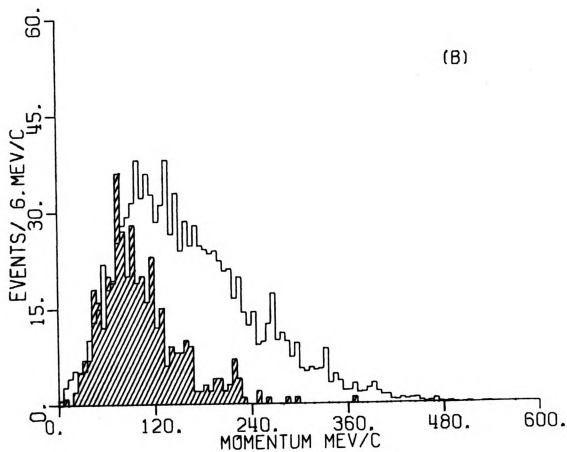
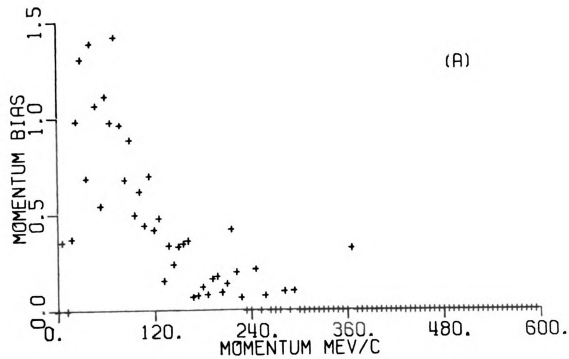


Fig. 2.6-B.--Monte Carlo prediction for the slowest projected  $\pi^+$  momentum distribution for Mark 16. The shaded area represents that from the six prong data sample. The Monte Carlo distribution is normalized to the data below 80 MeV/c.





2.6-A for

this same

the  $\bar{p}d \rightarrow$

in the sam

ionization

Or

the percent

found. Th

due to the

Table 2.11

appropriat

momentum ra

effect. Th

Section 2.6

In

cal cross s

given in Ta

given in Ta

ment losses

In

from topolog

2.6-A for 4 and 6 prongs respectively. One can also use this same probability curve to find how many events of the  $\bar{p}d \rightarrow n_{sp} + 2\pi^+ 2\pi^- + k\pi^0$  where ( $k = 1, 2, 3, 4$ ) are in the sample because the ratio depends only on the imposed ionization cutoff.

Once the scanning bias per momentum bin is known, the percentage contamination from any reaction can be found. These are listed in Table 2.10. The contaminations due to the  $\bar{p}d \rightarrow n_{sp} + \dots$  type reactions given in Table 2.11 are the product of these percentages by the appropriate  $\bar{p}p$  cross sections <sup>3,9,10</sup> extrapolated to this momentum range and corrected for the deuteron screening effect. The deuteron screening effect is explained in Section 2.6.2.

#### 2.6.2 Topological Cross Section Calculations

In the simplest situation, to obtain the topological cross sections, one would multiply the raw event count given in Table 2.8 by the appropriate interaction likelihood given in Table 2.6, and correct for scanning and measurement losses, that is

$$\sigma_n = \frac{\sigma_T}{N_T} * N_n * \frac{1}{\epsilon_{s,n} \epsilon_{M,n}} \quad (2.5)$$

In this work, the  $\bar{p}p$  type reactions are excluded from topological cross sections determinations.

Table 2.10.--Probability that the measurer will measure a particular  $\bar{p}p$  type event on the basis of the scanning criteria.

Momentum (GeV/c)	$4\pi$	$4\pi 1\pi^0$	$4\pi 2\pi^0$	$4\pi 3\pi^0$	$4\pi 4\pi^0$	$6\pi$	$6\pi 1\pi^0$	$6\pi 2\pi^0$
1.09	.223	.313	.380	.410	.483	.387	.456	.428
1.19	.213	.280	.360	.430	.445	.361	.436	.442
1.31	.217	.275	.355	.405	.487	.371	.412	.459
1.43	.190	.275	.360	.394	.493	.361	.398	.473

Table 2.11-A.--Contamination from the  $\bar{p}p$  type reactions in the 4-prong sample in millibarns. Correction due to the deuteron screening has been applied.

Momentum (GeV/c)	$4\pi$ mb	$4\pi 1\pi^0$ mb	$4\pi 2\pi^0$ mb	$4\pi 3\pi^0$ mb	$4\pi 4\pi^0$ mb	Total mb
1.09	.727 $\pm$ .061	3.52 $\pm$ .23	3.73 $\pm$ .28	2.43 $\pm$ .21	.13 $\pm$ .07	10.56 $\pm$ .85
1.19	.640 $\pm$ .057	3.00 $\pm$ .21	3.53 $\pm$ .27	2.55 $\pm$ .21	.12 $\pm$ .06	9.82 $\pm$ .81
1.31	.594 $\pm$ .051	2.90 $\pm$ .20	3.58 $\pm$ .27	2.45 $\pm$ .20	.17 $\pm$ .07	9.73 $\pm$ .79
1.43	.462 $\pm$ .051	2.81 $\pm$ .20	3.74 $\pm$ .26	2.46 $\pm$ .20	.20 $\pm$ .07	9.64 $\pm$ .77

Table 2.1

Momentum  
GeV/c

1.09

1.19

1.31

1.43

The

reaction  $\bar{p}$

2.12. Fig

topologica

Be

due to  $\bar{p}n$

proton, th

from Table

effect, s.

the target

by

where  $\sigma_{\bar{p}p'}$

reference

cross secti

the predicti

in equation

Table 2.11-B.--Contamination from the  $\bar{p}p$  type reactions in the 6 prong sample in millibarns. Correction due to deuteron screening has been applied.

Momentum GeV/c	$6\pi$ mb	$6\pi 1\pi^0$ mb	$6\pi 2\pi^0$ mb	Total mb
1.09	.44 $\pm$ .07	.71 $\pm$ .12	.039 $\pm$ .07	1.19 $\pm$ .26
1.19	.41 $\pm$ .06	.72 $\pm$ .11	.040 $\pm$ .08	1.17 $\pm$ .25
1.31	.42 $\pm$ .06	.71 $\pm$ .11	.084 $\pm$ .08	1.22 $\pm$ .25
1.43	.41 $\pm$ .06	.72 $\pm$ .11	.085 $\pm$ .08	1.21 $\pm$ .25

The N prong topological cross sections for the reaction  $\bar{p}d \rightarrow p_{sp} + N$  charged tracks are given in Table 2.12. Figure 2.7 compares the values with the odd prong topological cross section of Eastman, et al.<sup>3</sup>

Because the even (odd) prong events are really due to  $\bar{p}n$  interactions with (without) a visible spectator proton, the  $\bar{p}n$  topological cross section can be determined from Table 2.12, correcting for the deuteron screening effect, s. The factor s accounts for the shadowing of the target nucleon by the spectator nucleon and is given by

$$S = (\sigma_{\bar{p}p} + \sigma_{\bar{p}n}) / \sigma_{\bar{p}d} \quad (2.6)$$

where  $\sigma_{\bar{p}p}$ ,  $\sigma_{\bar{p}n}$  and  $\sigma_{\bar{p}d}$  are the cross sections from reference 11. Table 2.13 summarizes the  $\bar{p}n$  topological cross sections. Figure 2.8 compares these results with the predictions of the impulse approximations as expressed in equation 2.7.



Fig. 2.7.--The  $\bar{p}d \rightarrow 3, 4, 5$  and 6 prong topological cross section arising from the  $\bar{p}n$  interaction. The symbols are  $\square$  (3 prong, this work),  $\times$  (4 prong, this work),  $\boxtimes$  (5 prong, this work),  $-$  (6 prong, this work). The symbols  $\ominus$  and  $\boxminus$  are for the 3 and 5 prong data from Reference 3.

CROSS SECTION (MB)  
 0.0 2.5 5.0 7.5 10.0 12.5 15.0 17.5 20.0

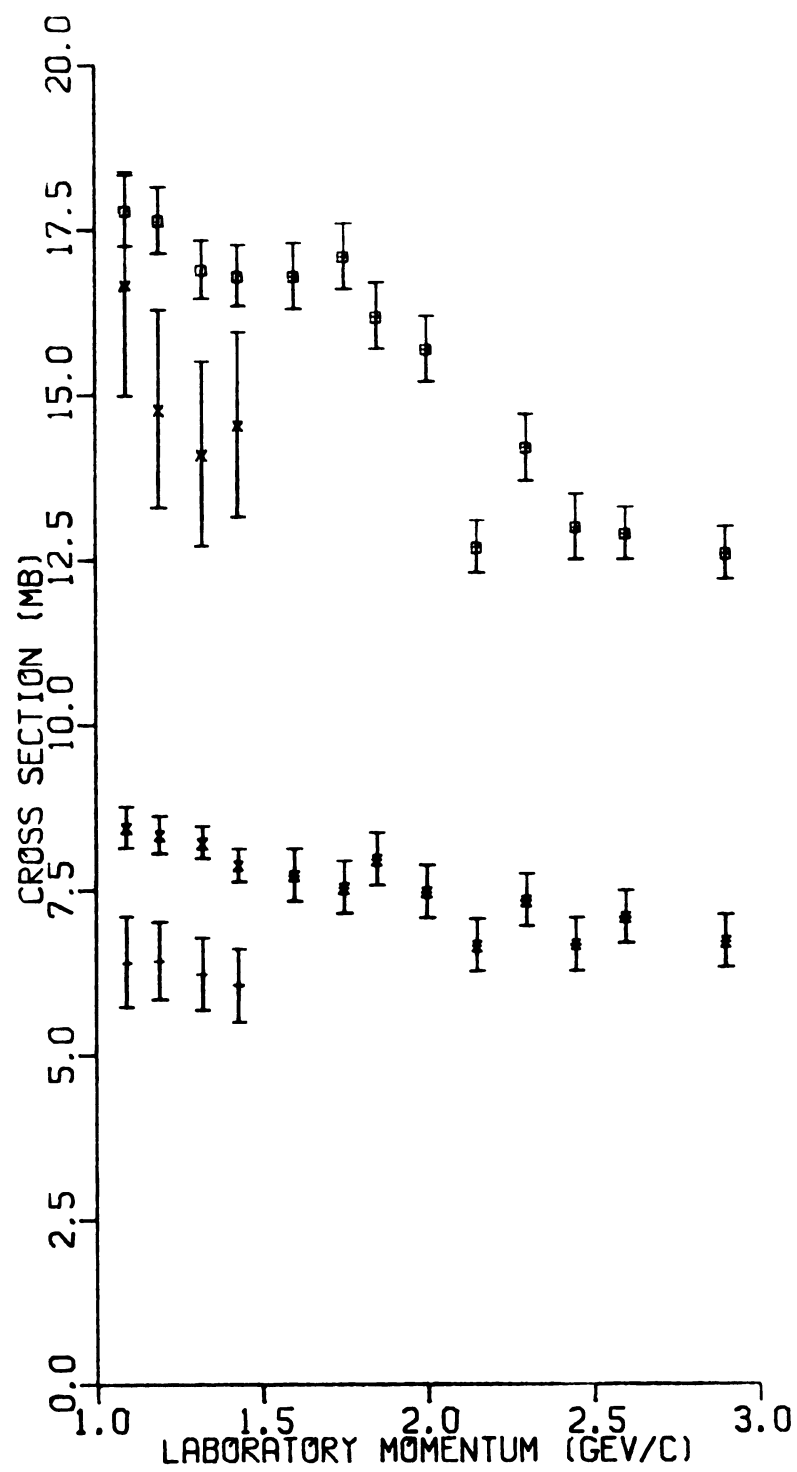


Fig. 2.8.--The  $\bar{p}n$  3 and 5 prong topological cross section compared with the prediction of the impulse approximation. The symbols are  $\nabla$  (3 prong, this work),  $\times$  (5 prong, this work). The symbols  $-$  and  $\square$  (with wider error bars) are for the 3 and 5 prong results from the impulse approximation.

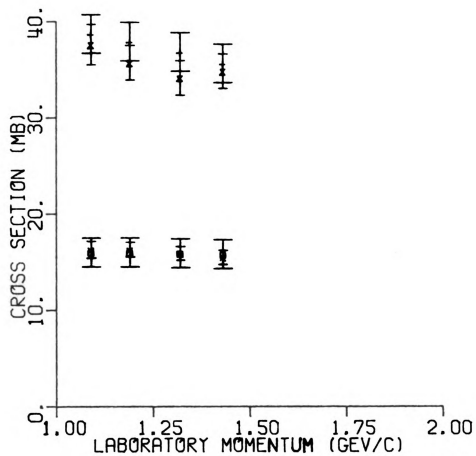


Table 2.12.--The  $\bar{p}d \rightarrow p_{sp} + \dots$  topological cross sections.

Momentum (GeV/c)	3 Prong (mb)	4 Prong (mb)	5 Prong (mb)	6 Prong (mb)
1.09	17.80 $\pm$ .47	16.68 $\pm$ 1.43	8.45 $\pm$ .32	6.41 $\pm$ .55
1.19	17.65 $\pm$ .43	14.79 $\pm$ 1.32	8.34 $\pm$ .24	6.43 $\pm$ .47
1.31	16.90 $\pm$ .39	14.11 $\pm$ 1.24	8.23 $\pm$ .21	6.23 $\pm$ .44
1.43	16.81 $\pm$ .40	14.55 $\pm$ 1.23	7.88 $\pm$ .22	6.05 $\pm$ .44

Table 2.13.-- $\bar{p}n$  topological cross section and the screening factor.

Momentum (GeV/c)	3 Prong mb	5 Prong mb	Screening Factor
1.09	37.6 $\pm$ 2.1	16.26 $\pm$ .88	1.09
1.19	35.70 $\pm$ 1.8	16.26 $\pm$ .78	1.10
1.31	34.12 $\pm$ 1.8	15.89 $\pm$ .71	1.10
1.43	34.8 $\pm$ 1.76	15.48 $\pm$ .73	1.11

$$\sigma_{\bar{p}n}^{N_{\text{odd prongs}}} = \left[ \sigma_{(\bar{p}d)}^{N+1 \text{ Prongs}} + \sigma_{(\bar{p}d)}^{N \text{ prongs}} \right] * s - \sigma_{(\bar{p}p)}^{N+1 \text{ Prongs}} \quad (2.7)$$

Here, good agreement is seen.

### 2.6.3 Acceptance Criteria for Events for the Reaction $\bar{p}n \rightarrow \pi^+\pi^-\pi^-$

A sample of events satisfying the acceptance criteria, discussed in Section 2.6, for the reaction

$\bar{p}d \rightarrow p_{sp} + \pi^+\pi^-\pi^-$  was separated from all other events. A partial ionization scan of this sample shows an initial contamination as given in Table 2.14.

Table 2.14.--The initial contamination of the data.

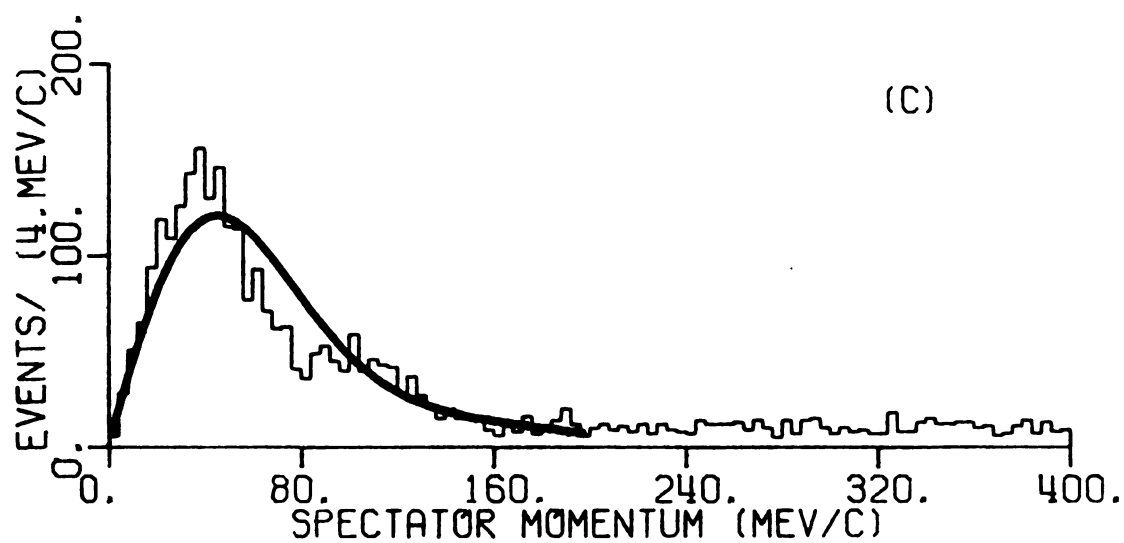
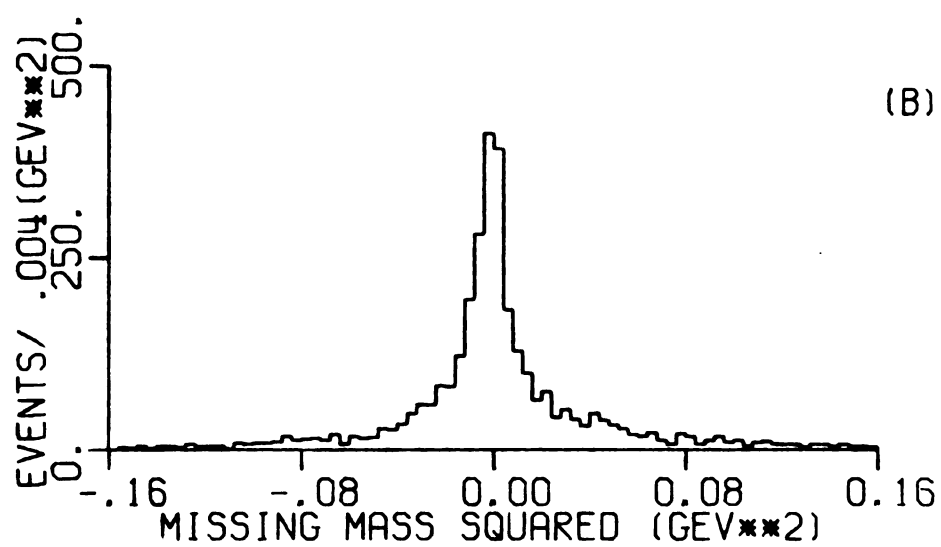
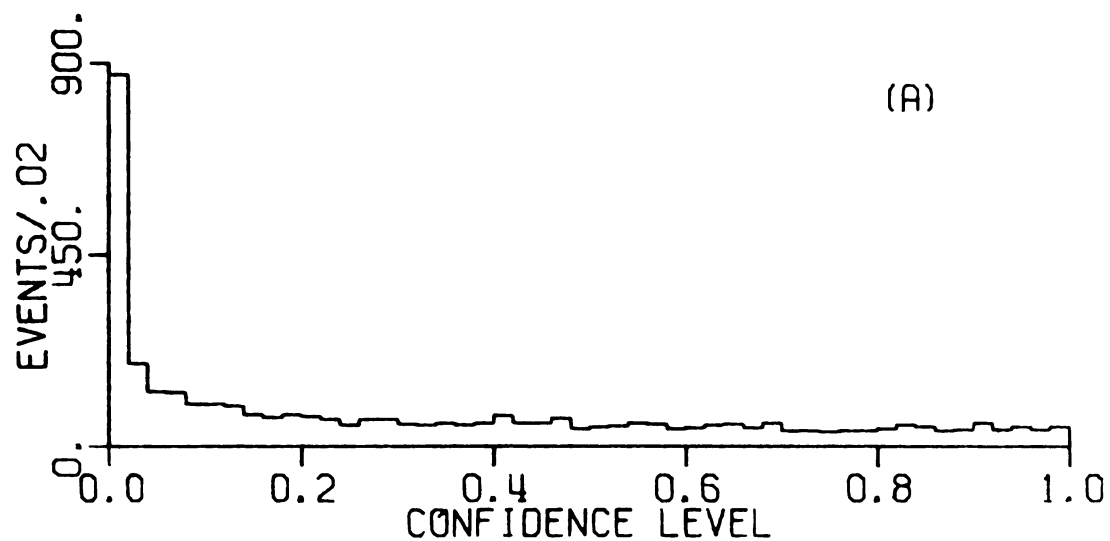
Reaction	% Contamination
$\bar{p}d \rightarrow p_{sp} + K^+K^-\pi^-$	6%
$\bar{p}d \rightarrow n_{sp} + \pi^+\pi^+\pi^-\pi^-$	6%
$(\bar{p}d \rightarrow p_{sp} + \pi^+\pi^-\pi^-) *$	3%
TOTAL	15%

\*These are 4-prong events with spectator proton and  $\pi^+$  incorrectly switched in the fit.

Initial confidence level, missing mass squared, and spectator momentum distributions are shown in Figure 2.9. One notes that the confidence level distribution is flat down to 2 1/2%. The missing mass squared distribution is symmetric around 0. The spectator momentum distribution is compared with the Hamada Johnston wave functions prediction.<sup>12</sup> Using only the events from the four prong sample (where spectator momentum was actually measured) the fit was performed over the momentum region between 100. and 200. MeV/c. Here good qualitative agreement is found. The area under the fitted curve was found to be equal to the number of data points.

Fig. 2.9.--Characteristics of events satisfying initial acceptance criteria for the  $\bar{p}d \rightarrow p_{sp} + \pi^+\pi^-\pi^-$  reactions

- (A) Confidence level distribution
- (B) Missing mass squared distribution
- (C) Spectator proton momentum distribution.  
The curve is from a prediction using the Hamada Johnston wave function.





To eliminate the small contamination that exists in the sample, many combinations of cuts on the missing mass squared and confidence level distribution were tried, and the corresponding total contamination was studied, based on the ionization scan. The cuts which maximize the total number of events and minimize the contamination was a missing mass squared cut at 2 standard deviations from 0, and a confidence level cut at 2.5%. No spectator cut was needed. After invoking these cuts the contamination was found to be less than 4%; mostly due to the reaction  $\bar{p}d \rightarrow p_{sp} + K^+K^-\pi^-$ . The confidence level and missing mass squared cuts gave an 18% overall reduction of the data.

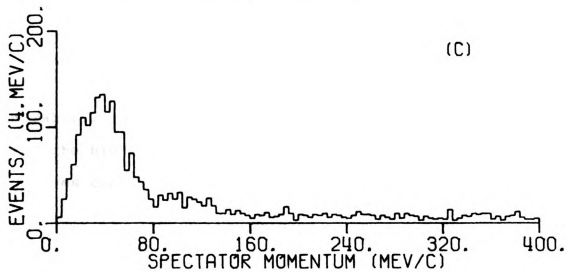
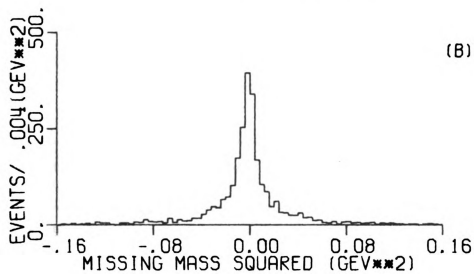
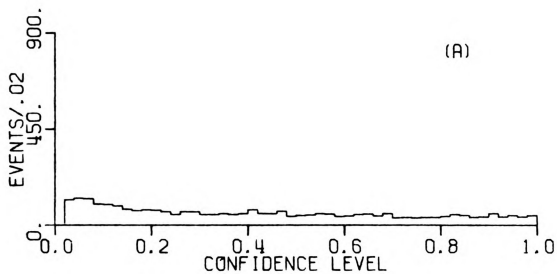
The final confidence level, missing mass squared, and spectator momentum distributions are shown in Figure 2.10. All distributions look representative of a clean data sample. The statistics for the final analysis sample are listed in Table 2.15.

#### 2.6.4 $\bar{p}n \rightarrow \pi^+\pi^-\pi^-$ Reaction Cross Section Calculation

The reaction cross section  $\bar{p}n \rightarrow \pi^+\pi^-\pi^-$  was obtained by multiplying the number of events in this channel before the confidence level cut by the interaction likelihood given in Table 2.6, and correcting for contaminations given in Table 2.11. Corrections for scanning and measuring losses as well as the deuteron screening effect were also applied. The cross sections are given

Fig. 2.10.--Characteristics of events satisfying final acceptance criteria for the  $\bar{p}d \rightarrow p_{sp} + \pi^+\pi^-\pi^-$  reaction.

- (A) Confidence level distribution
- (B) Missing mass squared distribution
- (C) Spectator proton momentum distribution.



Tab

Mon

(G)

Tab

Mon

(G)

In

Wet

Obs

Table 2.15-A.--The number of events accepted as the  $\bar{p}d \rightarrow p_{sp} + \pi^+\pi^-\pi^-$  reaction, and the corresponding cross section with the fiducial volume cut.

Momentum (GeV/c)	3 Prong	4 Prong	Cross section mb
1.09	210	164	$2.07 \pm .18$
1.19	290	207	$1.82 \pm .14$
1.31	443	364	$1.63 \pm .10$
1.43	245	227	$1.49 \pm .11$

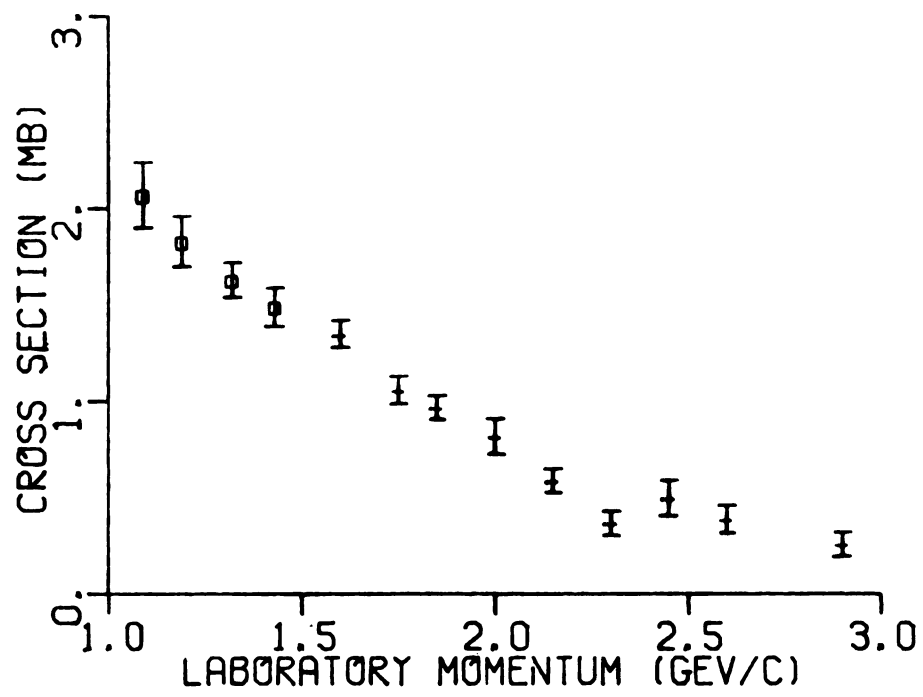
Table 2.15-B.--The number of events accepted as the  $\bar{p}d \rightarrow p_{sp} + \pi^+\pi^-\pi^-$  reaction, and the corresponding cross section without the fiducial volume cut. The total number of events is 2871.

Momentum (GeV/c)	3 Prong	4 Prong	Total
1.09	285	217	502
1.19	383	261	644
1.31	588	483	1071
1.43	349	305	654

in Table 2.15 and shown in Figure 2.11, and are compared with the higher momentum data from Eastman, et al.<sup>3</sup> One observes excellent agreement between these data.

Fig. 2.11.--The  $\bar{p}n \rightarrow \pi^+\pi^-\pi^-$  reaction cross section compared to the results published by Eastman, et al.

The symbols are  $\square$  (this work), and  $-$  (Eastman, et al.)



## CHAPTER III

### RESONANCE PRODUCTION

#### 3.1 The $\rho^0\pi^-$ , $f^0\pi^-$ Resonance Production

The  $\rho^0$  and  $f^0$  are resonance which dominantly decay into into the two particle  $\pi^+\pi^-$  state. If these resonances are produced in the  $\bar{p}d \rightarrow p_{sp} \pi^+\pi^-\pi^-$  interaction, the invariant mass distribution of the  $\pi^+\pi^-$  system will exhibit the characteristic Breit-Wigner bumps above an ever present background. Each bump should be located near the mass of the resonant particle, and the width of the bump inversely proportional to the lifetime of the resonance. The  $\pi^+\pi^-$  invariant mass distribution for events satisfying the final selection criteria corresponding to the  $\bar{p}d \rightarrow p_{sp} + \pi^+\pi^-\pi^-$  reaction is shown in Figure 3.1-A. The two bumps at 760 and 1280 McV/c indicate that a considerable amount of  $\rho^0$  and  $f^0$  production is present in the data.

#### 3.2 Event Selection

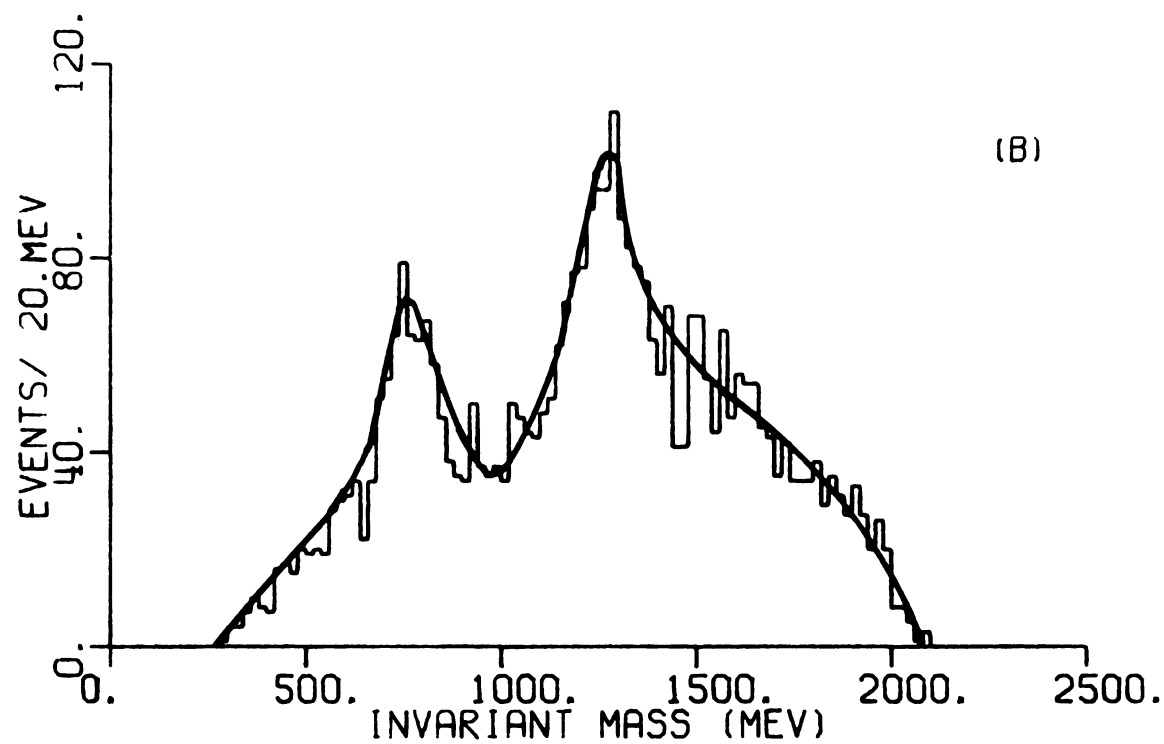
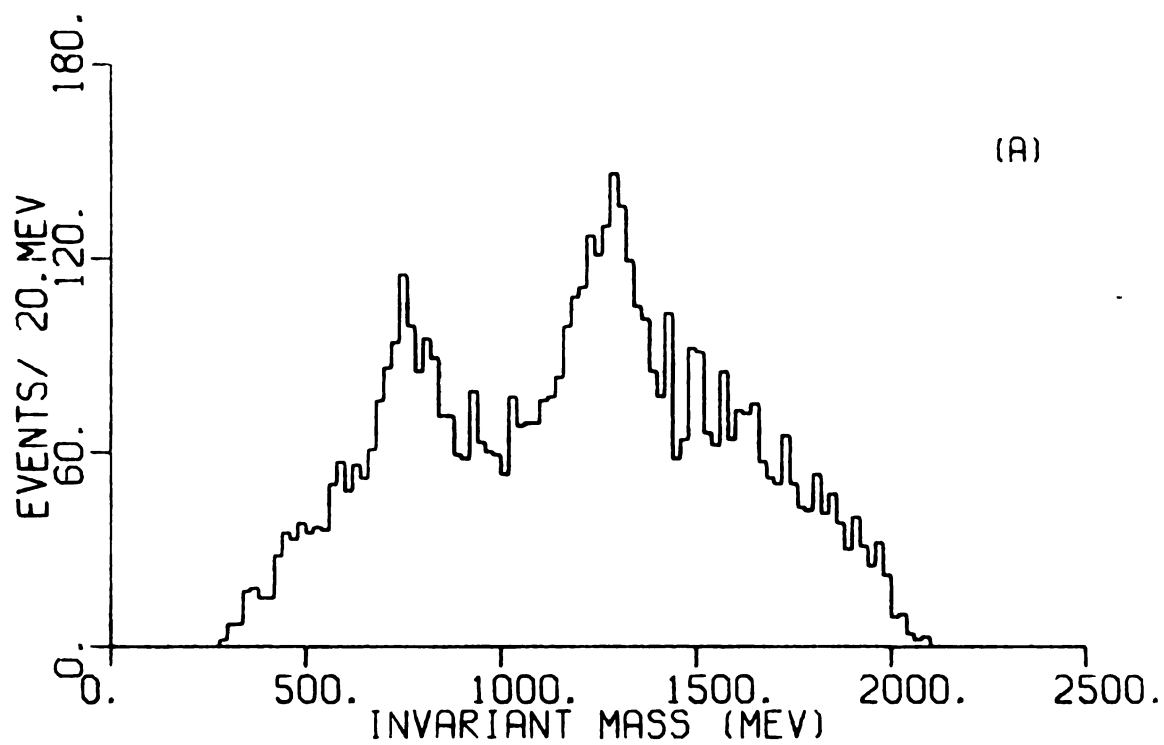
As explained in Chapter 2.6.3, confidence level and missing mass squared cuts reduced the contamination in the  $\bar{p}d \rightarrow p_{sp} + \pi^+\pi^-\pi^-$  sample to less than 4%. Since the remainder of this work deals with the  $\pi^+\pi^-\pi^-$  final state,



Fig. 3.1.--The  $\pi^+\pi^-$  invariant mass distribution for the reaction  $\bar{p}d \rightarrow p_{sp} + \pi^+\pi^-\pi^-$

(A) All events

(B) Events with  $p_{sp} < 160$  MeV/c



one must now investigate the validity in the assumption that studying the reaction  $\bar{p}d \rightarrow p_{sp} + \pi^+\pi^-\pi^-$  will lead to information on the reaction  $\bar{p}n \rightarrow \pi^+\pi^-\pi^-$ . A factor to be considered was discussed in section 2.6.2 concerning screening corrections. Another factor which is particularly important when discussing the dynamics of the interaction is the possible presence of double scattering effect. The incident antiproton may collide with the two constituent nucleons in succession or the product of the first collision may scatter from the spectator nucleon. The effect is being studied in detail by Zemany, et al.<sup>8</sup> Since this complication is not a property of the  $\bar{p}n$  interaction, the effect of this process must be removed. It is generally believed that such processes will alter the characteristics of collision products and/or that of the spectator nucleon. Collisions against the spectator nucleon increases its momentum due to the momentum transfer from the other participant. This distortion may be eliminated by imposing the additional acceptance criterion, that the proton spectator momentum be less than 160 MeV/c. Referring to  $\pi^+\pi^-$  invariant mass distribution in Figure 3.1-B, one indeed sees that the  $\rho^0$  and  $f^0$  peaks appear sharper than in Figure 3.1-A. The final confidence level, missing mass squared, and spectator momentum distribution given in Figure 3.2 reflect the high quality of this data sample. An event count for this sample is given in Table 3.1.

Fig. 3.2.--Characteristic of events satisfying final acceptance criteria for the reaction  
 $\bar{p}n \rightarrow \pi^+\pi^-\pi^-$

- (A) Confidence level distribution
- (B) Missing mass squared distribution
- (C) Spectator momentum distribution

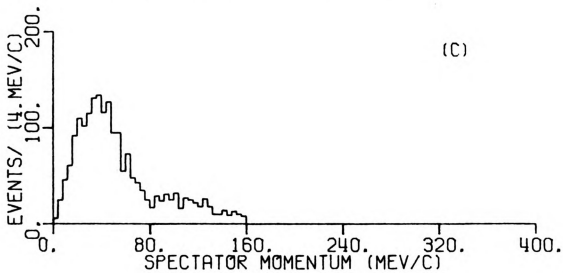
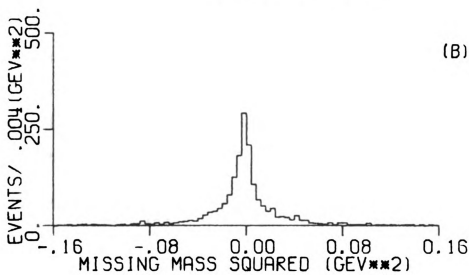
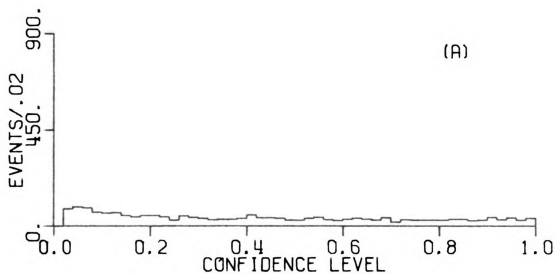


Table 3.1.--Sample count. Total = 1919 events.

Momentum GeV/c	3-Prong	4-Prong	Total
1.09	278	58	336
1.19	373	71	444
1.31	573	147	720
1.43	340	79	419

### 3.3 Resonance Cross Section Determination

The maximum likelihood method<sup>13</sup> is used here. The data in Figure 3.1-B are assumed to be an incoherent sum of phase space background and resonant productions. The distribution is assumed to be proportional to the squared matrix element

$$|M|^2 = (1 - \sum_{i=1}^2 \alpha_i) + \sum_{i=1}^2 \alpha_i R_i / N_i \quad (3.1)$$

$$\text{with } R_j = \left| \frac{\Gamma_j/2}{(M_j - E) - i \Gamma_j/2} \right|^2 = \frac{\Gamma_j^2/4}{(M_j - E)^2 + \Gamma_j^2/4} \quad (3.2)$$

where  $\Gamma_j$  is the full width at half maximum of the  $j^{\text{th}}$  resonance, with mass  $M_j$ . The normalization factor  $N_i$  is obtained by integrating  $R_i$  over the available phase space.

In the fit only  $\rho^0$ ,  $f^0$  production was assumed to exist, and the fit parameters were therefore  $\alpha_\rho$ ,  $\alpha_f$ ,  $m_\rho$ ,  $m_f$  and  $\Gamma_\rho$ ,  $\Gamma_f$ . The parameters obtained from the fit to the entire data sample from 1.09 to 1.43 GeV/c are listed

in Table 3.2 and shown as a smooth curve in Figure 3.1-B. Using the masses and widths thus obtained, the events at each individual momentum were fitted for  $\alpha_\rho$  and  $\alpha_f$ . These percentages were scaled to the total  $\bar{p}n \rightarrow \pi^+\pi^-\pi^-$  reaction cross section to give the partial  $\rho^0\pi^-$ ,  $f^0\pi^-$ , and statistical production cross section contributions at each momentum. The results are given in Table 3.3. As an example of the quality obtained in the individual momentum fitting process, Figure 3.3 shows the  $\pi^+\pi^-\pi^-$  fit for the events with a laboratory momentum of 1.31

Table 3.2.--Resonance Parameters for the reaction  
 $\bar{p}n \rightarrow \pi^+\pi^-\pi^-$  from 1.09 to 1.43 GeV/c.

Fit Parameter <sup>1</sup>	Values (MeV/c)
$M_\rho^*$	761. $\pm$ 7.
$M_\rho^*$	1278. $\pm$ 7.
$\omega_\rho$	165. $\pm$ 11.
$\omega_f$	176. $\pm$ 13.
$\chi^2/(\text{degree of freedom})$	1.3

\*The actual masses here should be 1.8% higher due to a small magnetic field problem.

<sup>1</sup>In this fit the masses and widths were constrained to be within 2 standard deviations of the Particle Data Group values.

Table 3.3-A.-- $\alpha_\rho$  and  $\alpha_f$  values for  $\bar{p}n \rightarrow \pi^+\pi^-\pi^-\pi^-$  for momenta 1.09, 1.19, 1.31 and 1.43 GeV/c.

Laboratory Momentum GeV/c	$\alpha_\rho$	$\alpha_f$	% Statistical	$\chi^2$ (degree of freedom)
1.09	$30.0 \pm 5$	$47.9 \pm 6$	$22.1 \pm 8$	1.05
1.19	$33.1 \pm 5$	$42.4 \pm 6$	$24.5 \pm 8$	1.17
1.31	$25.3 \pm 5$	$51.4 \pm 6$	$23.3 \pm 9$	1.57
1.43	$26.6 \pm 9$	$29.6 \pm 12$	$43.8 \pm 18$	1.38



Table 3.3-B.--The  $\rho^0$ ,  $\pi^-$ ;  $f^0$ ,  $\pi^-$ ; and  $\pi^+\pi^-\pi^-$  statistical cross sections for the momentum range of 1.09 to 1.43 GeV/c.

Laboratory Momentum GeV/c	Total $\bar{p}n \rightarrow \pi^+\pi^-\pi^-$ (mb)	$\bar{p}n \rightarrow \rho^0\pi^-$ (mb)	$\bar{p}n \rightarrow f^0\pi^-$ (mb)	$\bar{p}n \rightarrow \pi^+\pi^-\pi^-$ (Statistical) (mb)
1.09	$2.07 \pm .18$	$.624 \pm .10$	$1.00 \pm .12$	$.446 \pm .17$
1.19	$1.82 \pm .14$	$.605 \pm .09$	$.775 \pm .11$	$.440 \pm .13$
1.31	$1.63 \pm .10$	$.415 \pm .08$	$.842 \pm .10$	$.373 \pm .14$
1.43	$1.49 \pm .11$	$.399 \pm .13$	$.444 \pm .18$	$.647 \pm .24$

Fig. 3.3.--The  $\pi^+\pi^-$  invariant mass distribution at 1.31 GeV/c. The solid lines give the shape and relative amount of each term in the fit.

(A) Final fit distribution

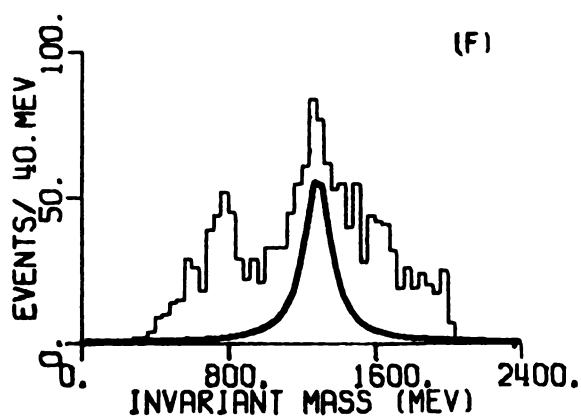
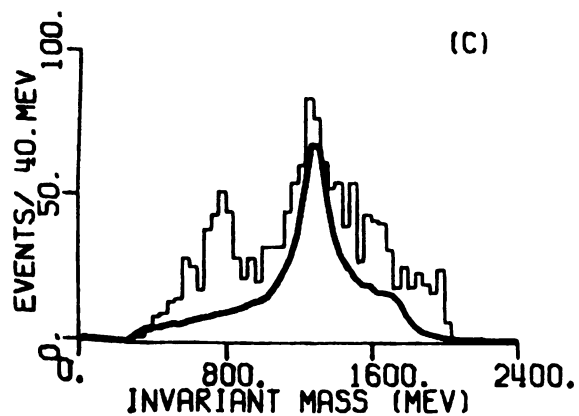
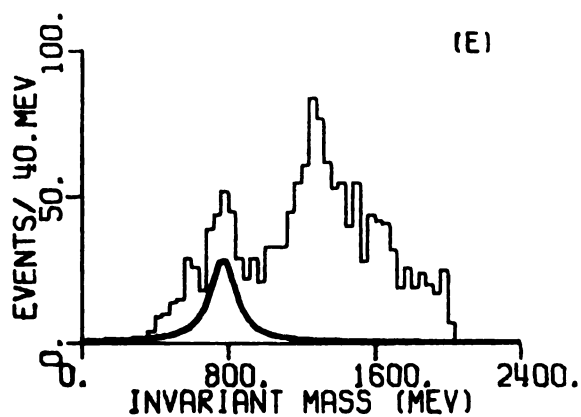
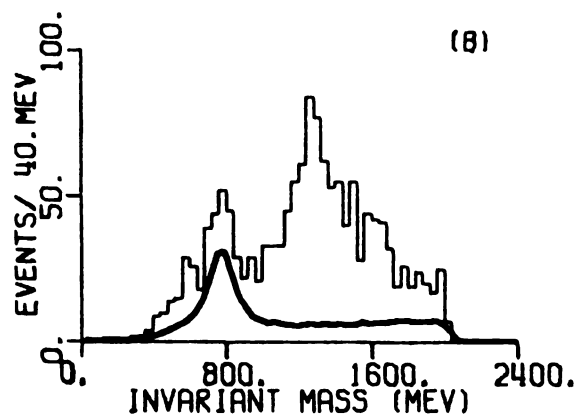
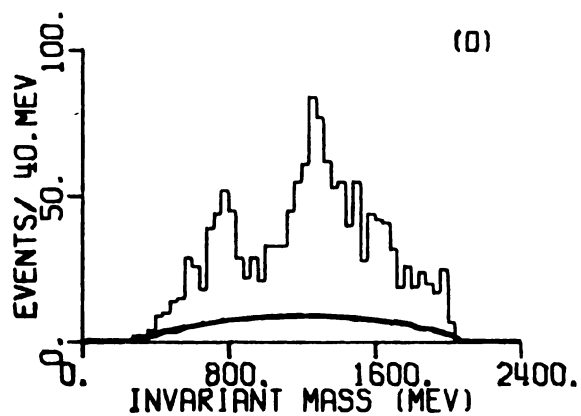
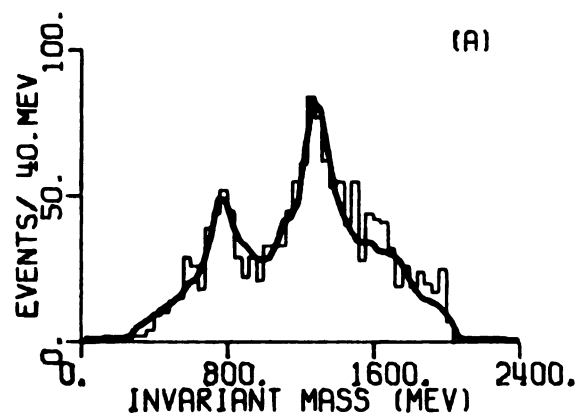
(B)  $\rho^0$  contribution

(C)  $f^0$  contribution

(D) Statistical production contribution

(E) Breit-Wigner curve for  $\rho^0$

(F) Breit-Wigner curve for  $f^0$

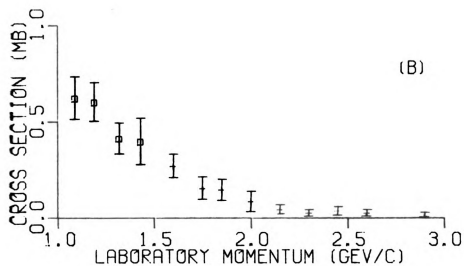
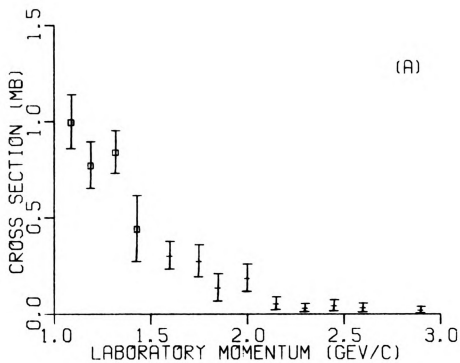


GeV/c. Figure 3.4 compares the  $\rho^0\pi^-$ , and  $F^0\pi^-$  cross sections with the higher momenta results by Ma et al.<sup>15</sup> One notes good agreement between the data.

Fig. 3.4.--The resonant cross section and comparison with higher momentum data

(A) The symbols are  $\square (f^0\pi^- \text{ this work})$  and  
-  $(f^0\pi^- \text{ from reference 15})$

(B) The symbols are  $\square (\rho^0\pi^- \text{ this work})$  and  
-  $(\rho^0\pi^- \text{ from reference 15})$



## CHAPTER IV

### DIFFERENTIAL CROSS SECTIONS AND COMPARISON OF LINE REVERSED REACTIONS

#### 4.1 Motivation and Formalism

The crossing symmetry principle asserts that the scattering amplitude describing a reaction remains the same in form when particles are replaced by antiparticles provided that signs of the four momenta are reversed.<sup>16</sup> This basic property of strong interaction S matrix theory has been subjected to experimental tests in two body reactions such as  $\bar{p}p \rightarrow \pi^-\pi^+$  and  $\bar{p}p \rightarrow K^-K^+$ .<sup>17,18</sup> This section deals with a further test of this principle using quasi two body reactions

$$\bar{p}n \rightarrow \rho^0\pi^- \quad (4.1)$$

$$\text{and} \quad \bar{p}n \rightarrow f^0\pi^- \quad (4.2)$$

and the line reversed reactions

$$\pi^-p \rightarrow n\rho^0 \quad (4.3)$$

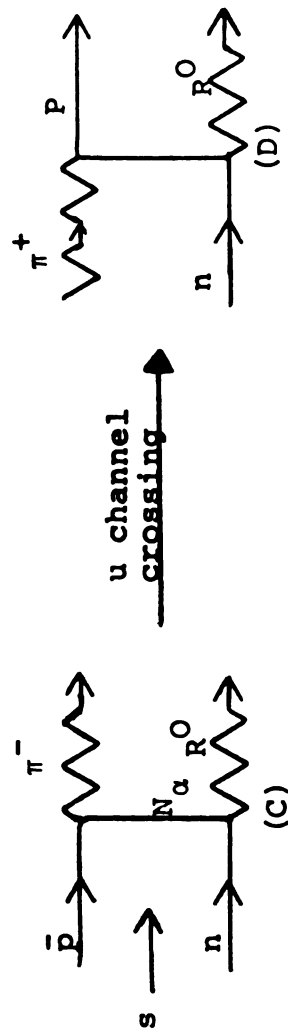
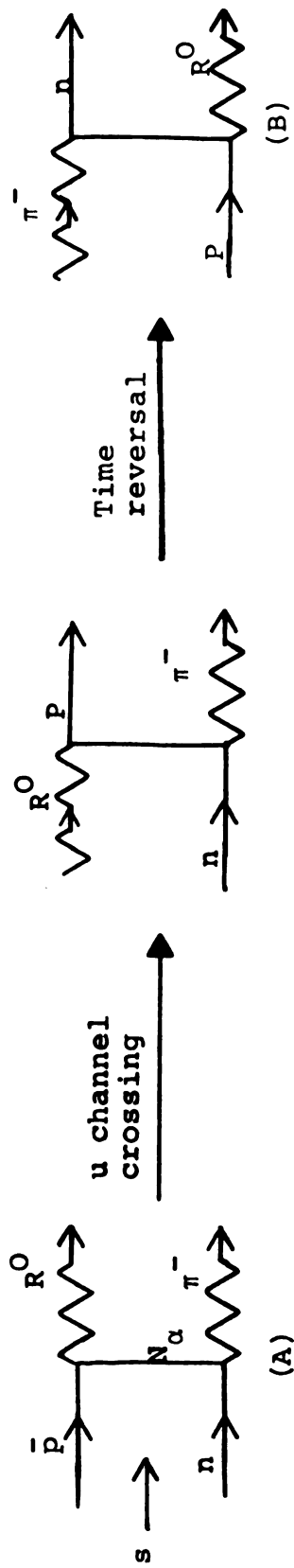
$$\pi^-p \rightarrow nf^0 \quad (4.4)$$

In Figure 4.1, if  $A_i(u,s)$  represents the amplitude for the s channel process (A)  $\bar{p}n \rightarrow R^0\pi^-$ , and  $B_i(u,t)$  represents the amplitude for the t channel process (B)  $\pi^-p \rightarrow nR^0$  for exchange of the  $i^{\text{th}}$  Regge trajectory, where R stands

Fig. 4.1.--The elementary baryon exchange diagrams for the  
Processes listed below

- (A) Forward s channel process for  $\bar{p}n \rightarrow R^0\pi^-$
- (B) Backward t channel process for  $\pi^-p \rightarrow R^0n$
- (C) Backward s channel process for  $\bar{p}n \rightarrow R^0\pi^-$
- (D) Backward t channel process for  $\pi^+n \rightarrow R^0p$





for either the  $\rho^0$  or  $f^0$  meson, then it is known<sup>17,18,19</sup> that there are two classes of trajectories for which

$$\sum_i |A_i|^2 = \sum_i |B_i|^2$$

Class 1: All the contributing trajectories have the same signature, or if they do not have the same signature the exchange of one of the trajectories is dominant.

Class 2: Contributing trajectories are exchange degenerate.

Similar arguments may also be made for Figures (4.1-C) and (4.1-D).

In the case of  $\rho^0$  production one can exchange  $\Delta\delta$ ,  $N_\gamma$  and  $N_\alpha$  trajectories. For  $f^0$  production only the  $I=1/2$   $N_\gamma$  and  $N_\alpha$  are allowed. Although the signatures of  $\Delta\delta$  and  $N_\gamma$  are different, it is found experimentally<sup>20</sup> in  $\pi^+p$  backward elastic scattering that  $N_\alpha$  is the dominant trajectory. The assumption made here is that the exchange of  $N_\alpha$  is the dominant trajectory. The assumption made here is that the exchange of  $N_\alpha$  also dominates the reactions considered in this analysis.

In the  $f^0$  production the experimentally confirmed<sup>21</sup> exchange degeneracy of the  $N_\alpha$  and  $N_\gamma$  is assumed sufficient to allow the cross channel comparison to be made. The same argument should hold in the  $\rho^0$  production case.

Referring to Figure 4.1, the  $s$  channel differential cross section is given by<sup>19</sup>

$$\frac{d\sigma}{du} = \frac{\pi}{(2s_a+1)(2s_b+1)} \frac{1}{q_s^2} \sum_i |A_i|^2 |\cos^2(\frac{1}{2}\theta_u)|^{|\lambda+\mu|} |\sin^2(\frac{1}{2}\theta_u)|^{|\lambda-\mu|} \quad (4.5)$$

where the kinematic singularities of the helicity amplitude have to be explicitly removed so that  $A_i$  may be analytically continued to the cross channel region of the Mandelstam diagram.  $s_a$  and  $s_b$ ,  $\theta_u$  and  $\theta$  are the spins of the initial state particles, the incident c.m. momentum, and the scattering angle respectively.  $\lambda$  and  $\mu$  are the relative final and initial state helicities.

If  $\sum_i |A_i|^2 = \sum_i |B_i|^2$  as is expected here, then

$$(2s_a + 1) (2s_b + 1) q_s^2 \frac{d\sigma}{du}(s) = (2s_c + 1) (2s_d + 1) q_t^2 \frac{d\sigma}{du}(t) \quad (4.6)$$

where  $u$  clearly retains its meaning throughout this discussion.

Putting in the initial state spins, equation (4.6) is equivalent to

$$\frac{d\sigma}{du} (\bar{p}n \rightarrow R^0 \pi^-) = \frac{1}{2} \left( \frac{q_\pi}{q_{\bar{p}}} \right)^2 \frac{d\sigma}{du} (\pi^+ N \rightarrow p R^0) \quad (4.7.1)$$

and

$$\frac{d\sigma}{dt} (\bar{p}n \rightarrow R^0 \pi^-) = \frac{1}{2} \left( \frac{q_\pi}{q_{\bar{p}}} \right)^2 \frac{d\sigma}{du} (\pi^- p \rightarrow n R^0) \quad (4.7.2)$$

where  $q_\pi$  is the incident cm momentum for the  $\pi N$  reactions and  $q_{\bar{p}}$  is the incident cm momentum for the  $\bar{p}n$  reaction.

## 4.2 Experimental Analysis

Data used in this analysis are divided into three groups. Group 1 include events from 1.09, 1.19, 1.31 and 1.43 GeV/c. Event selection for this sample has been discussed in Chapter 3. Group 2 data include momentum settings of 1.60, 1.75, 1.85, and 2.00 GeV/c, and Group 3 includes 2.15, 2.30, 2.60, 2.75, and 2.90 GeV/c. Both Groups 2 and 3 are from reference 15.

Figure 4.2 shows the differential distributions for data which had  $\pi^+\pi^-$  invariant masses within the resonance region described in Table 4.1. The variables,  $t' = t - t_{\min}$  and  $u' = u - u_{\min}$  were used in order to remove the kinematic effects associated with the invariant mass spread within each resonance region. The variable  $R'$  stands for  $t'$  or  $u'$ , which ever is appropriate. The differential cross section  $d\sigma/dt'$  is plotted if  $\cos\theta^* \geq 0$  and  $d\sigma/du'$  is plotted if  $\cos\theta^* < 0$ , where  $\theta^*$  is the cm scattering angle of the  $\pi^+\pi^-$  invariant mass system with respect to the incident  $\bar{p}$  as shown in Figure 4.3.

In Figure 3.3 one can see that a randomly selected  $\pi^+\pi^-$  combination from a resonance region would not necessarily result from resonance production. To obtain differential cross sections for the production of the  $\rho^0\pi^-$  and  $f^0\pi^-$  states, one must remove contributions due to nonresonance background events. In order to determine the shape of the nonresonance differential cross section,

1

Fig. 4.2.--Differential distributions. The background is shown by the shaded area (A), (B), and (C) are for the reaction  $\bar{p}n \rightarrow \rho^0\pi^-$ , (D), (E) and (F) are for the reaction  $\bar{p}n \rightarrow f^0\pi^-$ .

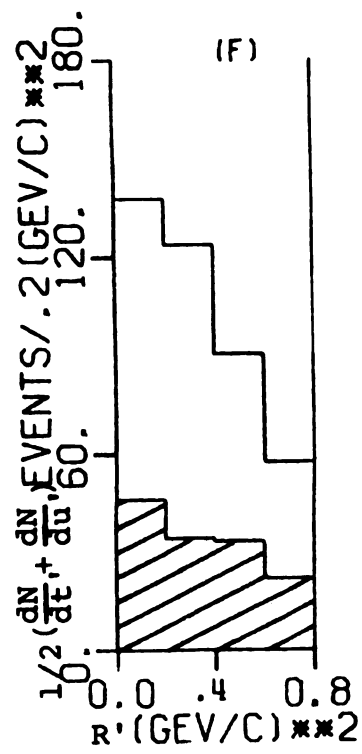
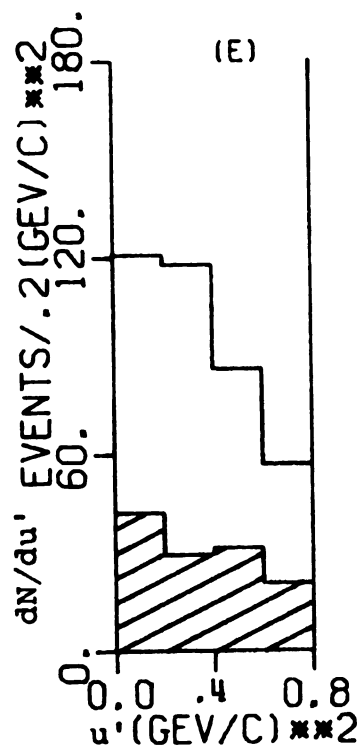
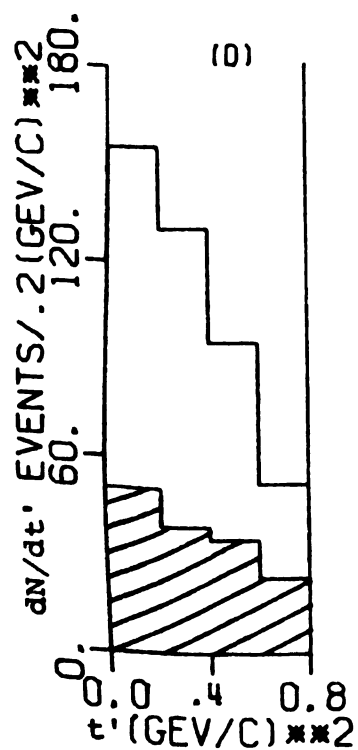
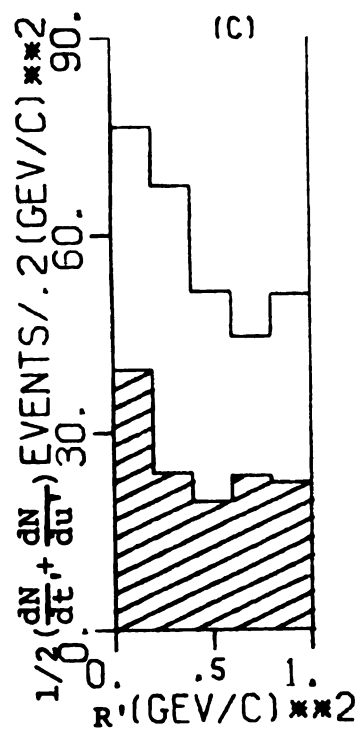
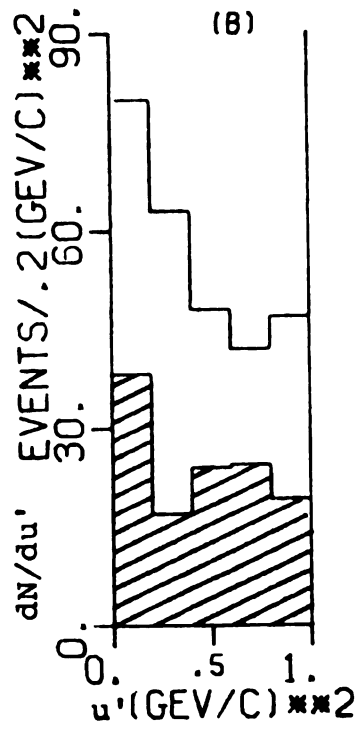
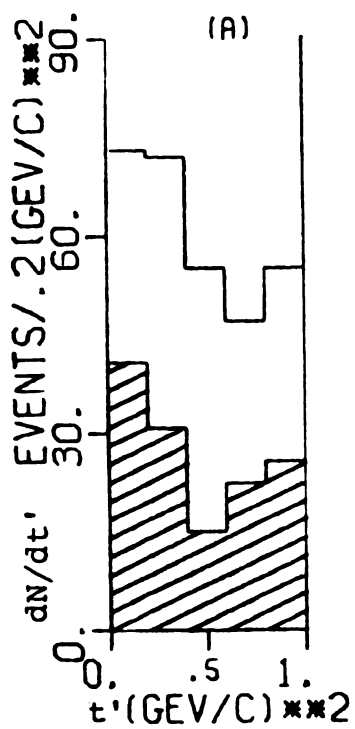


Table 4.1.--Invariant mass cuts.

Description	Mass (MeV)
$\rho^0$ resonance region	640 - 880
$f^0$ resonance region	1160 - 1400
$\rho^0$ lower control band region	540 - 640
$\rho^0$ upper control band region	880 - 980
$f^0$ lower control band region	940 - 1140
$f^0$ upper control band region	1420 - 1520

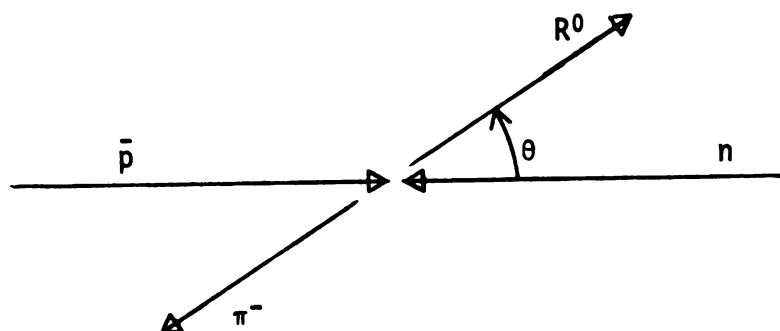


Fig. 4.3.--The definition for  $\theta$  in the cm frame. Here  $R^0$  refers to the  $\pi^+\pi^-$  system.



control band cuts on each side of the resonance region are made, as shown in Figure 4.4 and given in Table 4.1.

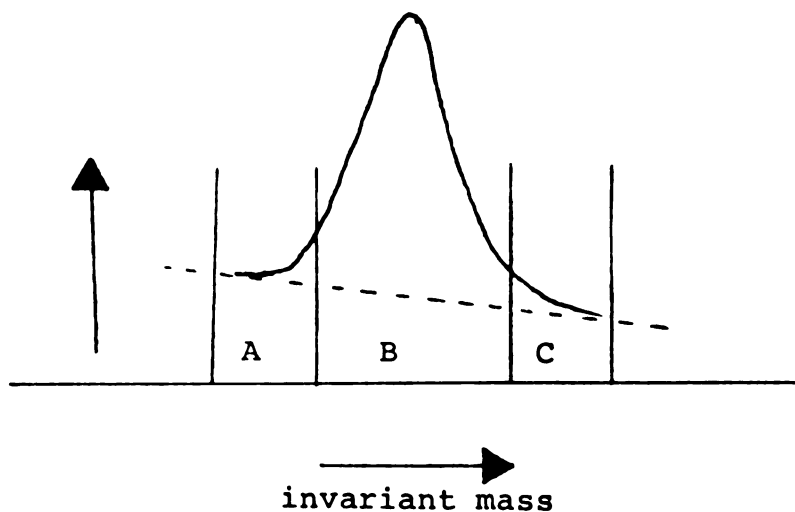


Fig. 4.4.--Resonance region and control band regions. Background is shown under the dotted line. The regions are defined as

- A. Lower control band region
- B. Resonance region
- C. Upper control band region

A specific boundary to the resonance regions B, was selected to maximize the ratio of resonance to nonresonant events, and to keep as many resonance events as possible for analysis.

In order to obtain a good representation of the background under the resonance, the control band regions were made as narrow as possible.

It is assumed here that the behavior of background events is slow varying across the resonance region. The events in the control bands are normalized to the total amount of background in the resonance region, and are

shown as the shaded area in Figure 4.2. The actual amount of resonance events within the resonance regions were found to be 65% and 63% for the  $\rho^0$  and  $f^0$  respectively.

To obtain the resonance production distribution, the background contribution is removed from the differential cross section of the resonance region and the result is normalized to the total resonance production cross section. These cross sections are shown in Figure 4.5 and are listed in Table 4.2.

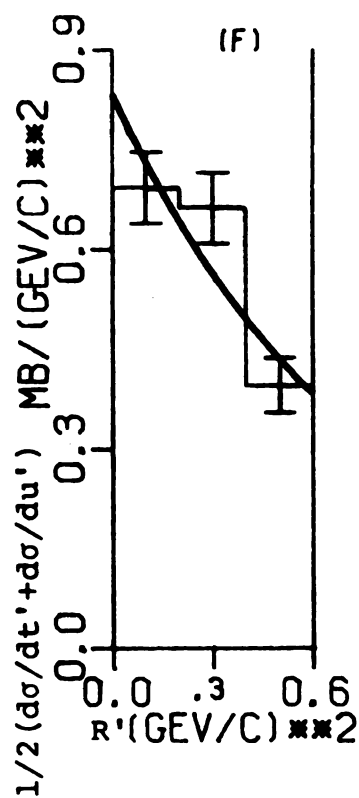
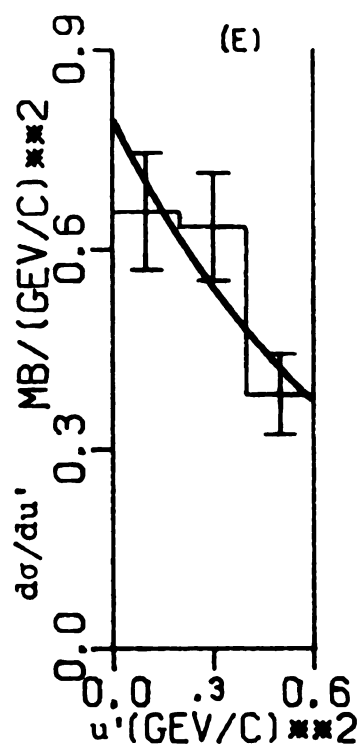
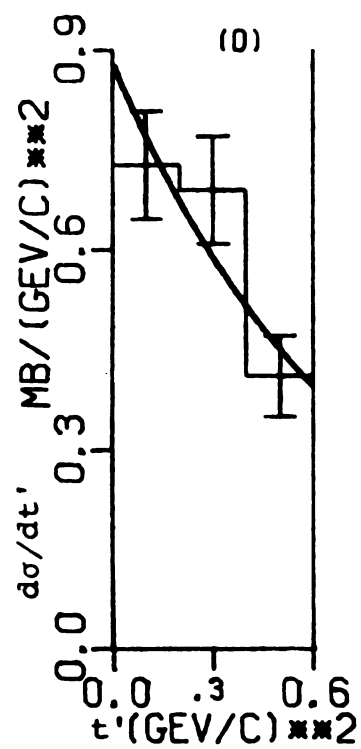
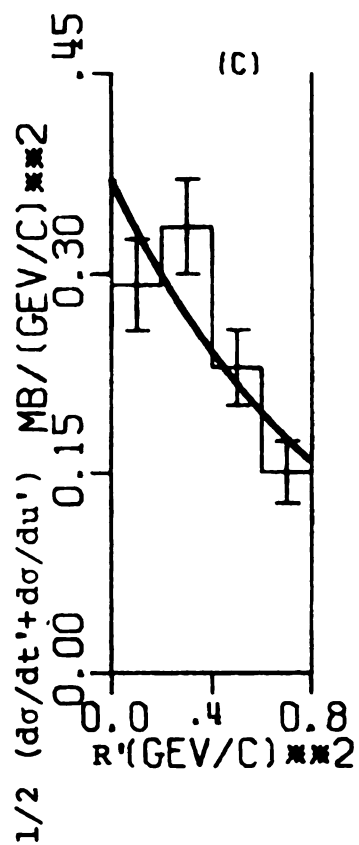
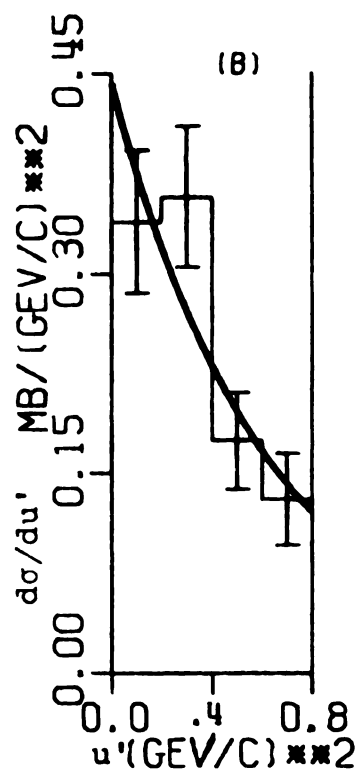
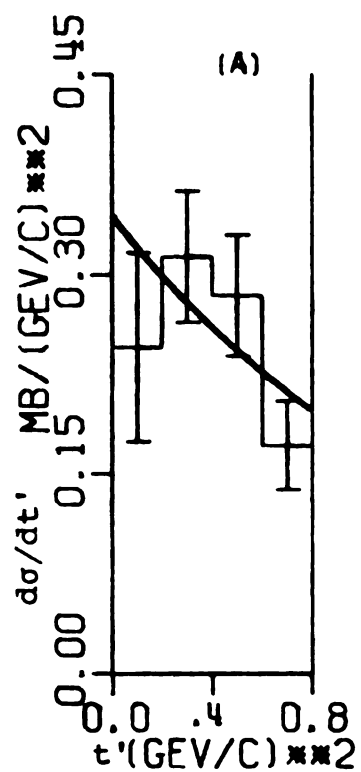
Table 4.2.--Average Differential Cross Sections.

$R'$ (GeV/c) <sup>2</sup>	$\frac{d\sigma}{dt'}(\rho)$ (mb)/(GeV/c) <sup>2</sup>	$\frac{d\sigma}{du'}(\rho)$ (mb)/(GeV/c) <sup>2</sup>	$\frac{d\sigma}{dt'}(f)$ (mb)/(GeV/c) <sup>2</sup>	$\frac{d\sigma}{du'}(f)$ (mb)/(GeV/c) <sup>2</sup>
.0 → .1	.19 ± .07	.27 ± .07	.52 ± .09	.69 ± .10
.1 → .2	.30 ± .08	.40 ± .08	.91 ± .11	.62 ± .09
.2 → .3	.40 ± .08	.43 ± .08	.91 ± .11	.56 ± .09
.3 → .4	.21 ± .07	.27 ± .08	.45 ± .08	.70 ± .10
.4 → .5	.40 ± .08	.054 ± .03	.34 ± .07	.43 ± .08
.5 → .6	.17 ± .05	.30 ± .08	.48 ± .08	.34 ± .07
.6 → .7	.18 ± .07	.15 ± .05		
.7 → .8	.16 ± .05	.12 ± .04		
.8 → .9	.37 ± .08	.26 ± .07		

Fig. 4.5.--The average differential cross section

(A), (B) and (C) are for  $\bar{p}n \rightarrow \rho^0\pi^-$

(D), (E) and (F) are for  $\bar{p}n \rightarrow f^0\pi^-$



The data are parameterized by

$$\frac{d\sigma}{dR'} = a e^{b(R')} \quad (4.8)$$

using the least squares method. The results are shown in Figure 4.5 as a smooth curve. Since the data were averaged over different laboratory momenta, the kinematic limit for  $R'$  at  $\cos \theta^* = 0$  is not a constant. The range of the fit was limited to the maximum  $R'$  value at 1.09 GeV/c. These are  $.8 \text{ (GeV/c)}^2$  and  $.6 \text{ (GeV/c)}^2$  for the  $\rho^0$  and  $f^0$  respectively. Table 4.3 lists the parameters obtained in these fits.

#### 4.3. The Line Reversed Reaction Comparisons

In the spirit of Regge models, it is expected that exchange trajectories in the  $t'$  and  $u'$  channels are identical. The data show that separately for  $\rho^0\pi^-$  and  $f^0\pi^-$  states, the slope and intercept values are indeed consistent for the  $t'$  and  $u'$  channels, thus suggesting that the data are consistent with such a conjecture. Therefore for the purpose of comparison with the line reversed reaction, the values of  $b_R$  and  $a_R$  will be used.

The available backward  $\pi N$  scattering data<sup>22,23</sup> limits the line reverse reaction comparison to the reaction in equation 4.7.2 where  $R^0$  is the  $\rho^0$  meson. The parameterization of these data was similar to the method used here, and thus can be directly compared.

Table 4.3.--The differential cross section parameters.

Resonance	$b_t \text{ (GeV/c)}^{-2}$	$b_u \text{ (GeV/c)}^{-2}$	$b_R \text{ (GeV/c)}^{-2}$	$a_t \text{ mb/(GeV/c)}^2$	$a_u \text{ mb/(GeV/c)}^2$	$a_R \text{ mb/(GeV/c)}^2$
$\rho$	$-.7 \pm .5$	$-1.6 \pm .5$	$-1.1 \pm .4$	$.340 \pm .073$	$.438 \pm .078$	$.366 \pm .065$
$f^0$	$-1.3 \pm .4$	$-1.3 \pm .4$	$-1.3 \pm .3$	$.869 \pm .11$	$.789 \pm .11$	$.829 \pm .08$

Table 4.4 gives the comparison for the three sets of data. The factor  $1/2 \left(\frac{q_\pi}{q_p}\right)^2$  is listed in column 6. Overall, the data are in good agreement, thus indicating that within the experimental uncertainties the crossing principle is valid in quasi two body annihilation processes. This further implies that the baryon exchange picture cannot be ruled out as a part of the annihilation mechanism, even at these relatively low energies. The good agreement between the direct and cross channel differential cross sections indicate that any absorption corrections<sup>24,25</sup> will have similar effects on both distributions.

Table 4.4.--The comparison of the intercept and slope parameters from this experiment with its line reversed reaction.

Reaction	Laboratory Momentum (GeV/c)	c.m. energy (GeV)	R range (GeV/c) <sup>2</sup>	Slope $b_R^{-2}$ (GeV/c) <sup>-2</sup>	Intercept, mb/(GeV/c) <sup>2</sup>	$1/2(\frac{q_\pi}{q_p})^2$	Intercept Comparison† mb/(GeV/c) <sup>2</sup>
$\bar{p}n \rightarrow \rho^0 \pi^-$	1.09 → 1.43	2.17	t~0 → .8	-1.1 ± .4	.366 ± .070	--	.366 ± .068
$\pi^- p \rightarrow n \rho^0$ <sup>22</sup>	2.77	2.47	t~1.5→3.9	-1.2 ± .4	.163 ± .016*	1.84	.300 ± .030
$\pi^- p \rightarrow n \rho^0$ <sup>23</sup>	4.0	2.90	--	--	.063 ± .021	2.80	.180 ± .06

\*This value was renormalized to the total backward  $\rho^0$  production cross section.

†For comparison, the value a is listed for  $\bar{p}n \rightarrow \rho^0 \pi^-$ , and  $1/2(\frac{q_\pi}{q_p})^2$  \* a is listed for  $\pi^- p \rightarrow \rho^0 n$ .



## CHAPTER V

### SPIN DETERMINATION OF THE ANTIPROTON NEUTRON SYSTEM

#### 5.1 Formalism

In order to better understand the reaction  $\bar{p}n \rightarrow \pi^+\pi^-\pi^-$  an angular momentum analysis was performed to determine the spin state composition of the initial  $\bar{p}n$  system. This determination is particularly important from the viewpoint of direct channel interaction. In this section the helicity frame is used to determine the initial spin composition by examining angular distributions of the resonance final states. This is justified since the  $\rho^0$  and  $f^0$  resonance production dominate the  $\bar{p}n \rightarrow \pi^+\pi^-\pi^-$  reaction.

Consider the reaction  $A + B \rightarrow C + D$ . One can relate the helicity amplitude to the differential cross section by

$$\frac{d\sigma}{d\Omega} = \frac{1}{(2S_a + 1)} \frac{1}{(2S_b + 1)} \sum_{abcd} |f_{c,d,a,b}|^2 \quad (5.1)$$

where the scattering amplitude is written as

$$f_{\lambda_c, \lambda_d, \lambda_a, \lambda_b}^{(s, \theta)} = \frac{1}{q} \sum_j (2J + 1) T_{\lambda_c, \lambda_d, \lambda_a, \lambda_b}^J(s) d_{\lambda, \mu}^J(\theta). \quad (5.2)$$

and  $T_{\lambda_c, \lambda_d, \lambda_a, \lambda_b}^J(s)$  is the transition amplitude. The function  $d_{\lambda, \mu}^J(\theta)$  is a single variable rotation matrix defined in reference 27. The letter  $s$  represents the cm energy squared and  $q$  is the initial cm momentum. The letter  $J$  is the total spin of the  $\bar{p}n$  system in units of  $\hbar$ . The helicities of particles C, D, A, and B are written as  $\lambda_c, \lambda_d, \lambda_a$  and  $\lambda_b$  respectively. The relative helicities  $\lambda$  and  $\mu$  are defined as  $\lambda_a - \lambda_b$  and  $\lambda_c - \lambda_d$ .

$$T_{-\lambda_c, -\lambda_d, -\lambda_a, -\lambda_b}^J = \eta_a \eta_b \eta_c \eta_d (-1)^{S_c + S_d - S_a - S_b} T_{\lambda_c, \lambda_d, \lambda_a, \lambda_b}^J \quad (5.3)$$

where  $\eta_a, \eta_b, \eta_c, \eta_d$  are the intrinsic parities of the particles and  $S_c, S_d, S_a, S_b$  are their spins.

If one now considers particle C to be either the  $\rho^0$  or  $f^0$  meson, and particle D to be the  $\pi^-$  meson, one knows that the spin and parities of these particles are  $1^-, 2^+$ , and  $0^-$  respectively. One further knows that the antiproton and neutron have spin  $1/2$  and opposite intrinsic parity. This means  $\eta_a \eta_b = -1$ , and equation (5.3) becomes  $T_{-\lambda_c, -\lambda_a, -\lambda_b}^J = -T_{\lambda_c, \lambda_a, \lambda_b}^J$  for both the  $\rho^0$  and  $f^0$  mesons. The helicities which must be considered for the antiproton and neutron are  $\pm 1/2$ . The  $\rho^0$  may be  $\pm 1, 0$  and for the  $f^0$  one has  $\pm 2, \pm 1, 0$ . The factor  $\sum_{abcd} |f_{cdab}|^2$  for the  $\rho^0$  meson can be explicitly written as follows, where the unconventional definition  $D_{\lambda, \mu}^J = \frac{(2J+1)}{q} d_{\lambda, \mu}^J(\theta)$  is utilized.

$$\sum_{abcd} |f_{cdab}|^2 =$$

$$\begin{aligned} & \left[ \sum_J T^J_{1, \frac{1}{2}, -\frac{1}{2}, 1} D^J \right]^2 + \left[ \sum_J T^J_{1, \frac{1}{2}, \frac{1}{2}, 0, 1} D^J \right]^2 + \left[ \sum_J T^J_{1, \frac{1}{2}, \frac{1}{2}, -1, 1} D^J \right]^2 + \\ & \left[ \sum_J T^J_{1, -\frac{1}{2}, \frac{1}{2}, 0, 1} D^J \right]^2 + \left[ \sum_J T^J_{0, \frac{1}{2}, -\frac{1}{2}, 10} D^J \right]^2 + \left[ \sum_J T^J_{0, \frac{1}{2}, \frac{1}{2}, 00} D^J \right]^2 + \end{aligned} \quad (5.4)$$

$$\begin{aligned} & \left[ \sum_J T^J_{0, -\frac{1}{2}, \frac{1}{2}, -1, 0} D^J \right]^2 + \left[ \sum_J T^J_{0, -\frac{1}{2}, -\frac{1}{2}, 00} D^J \right]^2 + \left[ \sum_J T^J_{-1, \frac{1}{2}, -\frac{1}{2}, 1, -1} D^J \right]^2 + \\ & \left[ \sum_J T^J_{-1, \frac{1}{2}, \frac{1}{2}, 0, -1} D^J \right]^2 + \left[ \sum_J T^J_{-1, -\frac{1}{2}, \frac{1}{2}, -1, -1} D^J \right]^2 + \left[ \sum_J T^J_{-1, -\frac{1}{2}, -\frac{1}{2}, 0, -1} D^J \right]^2 \end{aligned}$$

The symmetry relations for  $d_{\lambda, \mu}^J(\theta)$  are  $d_{\lambda, \mu}^J(\theta) = d_{-\mu, -\lambda}^J(\theta) (-1)^{\lambda-\mu} d_{\mu, \lambda}^J(\theta)$ . This means  $D_{1,1}^J = D_{-1,-1}^J$ ;  $D_{1,-1}^J = D_{-1,1}^J$ ; and  $D_{0,1}^J = D_{-1,0}^J = -D_{0,-1}^J = -D_{1,0}^J$ . Using these symmetry relations equation (5.4) becomes:

$$\begin{aligned} 2 * & \left[ \sum_J T^J_{1, \frac{1}{2}, -\frac{1}{2}, 1} D^J \right]^2 + \left[ \sum_J T^J_{-1, \frac{1}{2}, -\frac{1}{2}, 1, -1} D^J \right]^2 + \left[ \sum_J T^J_{0, \frac{1}{2}, \frac{1}{2}, 0, 0} D^J \right]^2 \\ & + \left[ \sum_J T^J_{1, \frac{1}{2}, \frac{1}{2}, 0, 1} D^J \right]^2 + \left[ \sum_J T^J_{1, -\frac{1}{2}, -\frac{1}{2}, 0, 1} D^J \right]^2 + \left[ \sum_J T^J_{0, -\frac{1}{2}, \frac{1}{2}, 0, 1} D^J \right]^2 \end{aligned} \quad (5.5)$$

The last three terms of equation (5.5) have the same angular distribution, even though they correspond to different helicity amplitudes. Because the interest here is the initial spin state, and because the unique separation of the last three terms is impossible, equation (5.5) is rewritten as:

$$2 * \left[ \left[ \Sigma_{J, \frac{1}{2}, -\frac{1}{2}}^J D_{1,1}^J \right]^2 + \left[ \Sigma_{J, -1, \frac{1}{2}, -\frac{1}{2}}^J D_{1,-1}^J \right]^2 + \left[ \Sigma_{J, 0, \frac{1}{2}, \frac{1}{2}}^J D_{0,0}^J \right]^2 + \left[ \Sigma_{J, R}^J D_{0,1}^J \right]^2 \right] \quad (5.6)$$

where  $[\Sigma_{J, R}^J D_{0,1}^J]^2$  has been written in place of the last three terms in equation (5.5). One finally obtains the expression for the angular differential cross section of the  $\rho^0$  meson as:

$$\frac{d\sigma}{d\cos\theta}(\rho^0) = \pi^* \left[ \left[ \Sigma_{J, \frac{1}{2}, -\frac{1}{2}}^J D_{1,1}^J \right]^2 + \left[ \Sigma_{J, -1, \frac{1}{2}, -\frac{1}{2}}^J D_{1,-1}^J \right]^2 + \left[ \Sigma_{J, 0, \frac{1}{2}, \frac{1}{2}}^J D_{0,0}^J \right]^2 + \left[ \Sigma_{J, R}^J D_{0,1}^J \right]^2 \right] \quad (5.7)$$

For the  $f^0$  meson the additional helicity states of  $\pm 2$  must be considered. This leads to an expression involving all the terms above, plus some additional ones. The differential cross section for the  $f^0$ ,  $\pi^-$  final state will be written as:

$$\frac{d\sigma}{d\cos\theta}(f^0) = \frac{d\sigma}{d\cos\theta}(\rho^0) + \pi^* \left[ \left[ \Sigma_{J, 2, \frac{1}{2}, -\frac{1}{2}}^J D_{-1,-2}^J \right]^2 + \left[ \Sigma_{J, 2, -\frac{1}{2}, \frac{1}{2}}^J D_{1,-2}^J \right]^2 + \left[ \Sigma_{J, F}^J D_{0,2}^J \right]^2 \right] \quad (5.8)$$

where the additional terms are not present if  $J < 2$ .

Similar to the situation for the  $\rho^0$  meson, one defines

$$[\Sigma_{J, F}^J D_{0,2}^J]^2 = \left[ \Sigma_{J, 2, \frac{1}{2}, \frac{1}{2}}^J D_{0,2}^J \right]^2 + \left[ \Sigma_{J, 2, -\frac{1}{2}, -\frac{1}{2}}^J D_{0,2}^J \right]^2$$

in the interest of simplicity.

## 5.2 Analysis

The angular distribution for  $\rho^{0-}$  and  $f^0\pi^-$  are shown in Figures 5.1-A and 5.1-B, respectively. The definition of the angle  $\theta$  is shown in Figure 4.3. In Figure 5.1 the statistical uncertainty of the data are shown with error bars. The background was removed by first, obtaining the average angular distribution for invariant mass combinations in regions A and C as shown in Figure 4.4. This distribution was then normalized to the background in the resonance region, and subtracted.

The analysis was limited to the events in the laboratory momentum range from 1.09 to 1.43 GeV/c. The distributions were fit to angular functions for J values up to and including 4. A typical term in the fit involving the complex transition matrix elements  $T_{\lambda_c, \lambda_a, \lambda_b}^J$  would appear as

$$\pi \sum_{JJ'} T_{\lambda_c, \lambda_a, \lambda_b}^J T_{\lambda_c, \lambda_a, \lambda_b}^{J'*} D_{(\lambda_a - \lambda_b), \lambda_c}^J D_{(\lambda_a - \lambda_b), \lambda_c}^{J'}$$

The transition amplitudes were normalized according to

$$\frac{d\sigma}{d\cos\theta} = \sigma \sum_{JJ'} T_{\lambda_c, \lambda_a, \lambda_b}^J \sqrt{\frac{(2J+1)}{2}} \sqrt{\frac{(2J'+1)}{2}} T_{\lambda_c, \lambda_a, \lambda_b}^{J'*} d_{\lambda, \mu}^J d_{\lambda, \mu}^{J'}$$

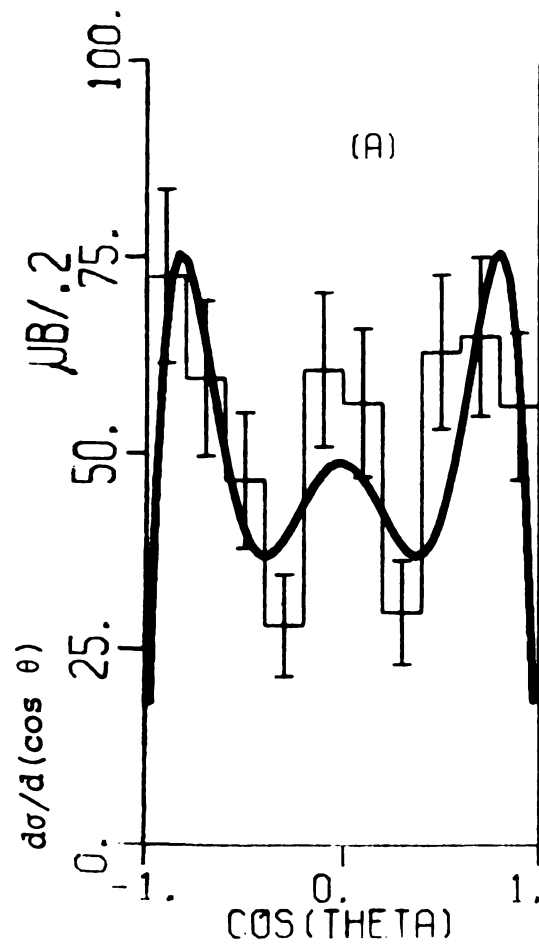
and the usual normalization

$$\int d_{\lambda, \mu}^J(\cos\theta) d_{\lambda, \mu}^{J'}(\cos\theta) d(\cos\theta) = \delta_{JJ'} \frac{2}{(2J+1)}$$

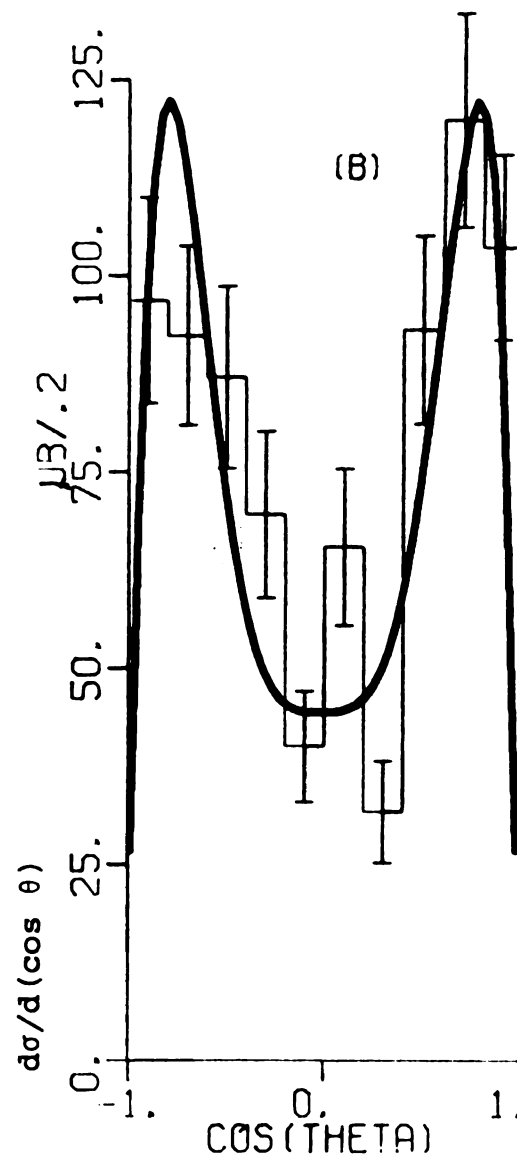
Fig. 5.1.--The resonance produced differential cross section.

A.  $\frac{d\sigma}{d(\cos \theta)}$  for the  $\rho^0$ , and fit.

b.  $\frac{d\sigma}{d(\cos \theta)}$  for the  $f^0$ , and fit.



RHO ANGULAR DISTRIBUTION



F ANGULAR DISTRIBUTION

was maintained. In this way the product  $T_{\lambda_c, \lambda_a, \lambda_b}^J$  will represent the percentage of the data in a particular total spin helicity state.

The least squares method was used to examine the fits for all combinations of total spin and helicity. Considering  $J$  values greater than 3 did not improve the  $\chi^2 / (\text{degree of freedom})$ . The best fits were obtained when incoherent sums of the helicity amplitudes represented by  $R^J$  and  $F^J$  were considered. A pure spin 2 state also gave reasonable agreement when an incoherent sum of all helicities was considered. The best results are shown in Figure 5.1 with a smooth line on top of the data. The spin state composition of the  $\bar{p}n$  system, as determined by the fit, is given in Table 5.1.

Table 5.1.--Spin state composition of the  $\bar{p}n$  system.

Total Spin	Amount of $\rho$ (percent)	Amount of $f$ (percent)
$J = 1$	$.31 \pm .07$	$.16 \pm .05$
$J = 2$	$.28 \pm .08$	$.52 \pm .06$
$J = 3$	$.33 \pm .07$	$.24 \pm .05$
Total	$.91 \pm .22$	$.92 \pm .16$



## CHAPTER VI

### THE DALITZ PLOT FOR THE $\bar{p}n \rightarrow \pi^+ \pi^- \pi^-$ REACTION AND ITS COMPARISON WITH THE PREDICTIONS OF THE VENEZIANO MODEL

#### 6.1. Motivation, Theoretical Background, and Analyses

One of the most successful models ever presented to explain high energy scattering phenomenology is the Regge Pole Model.<sup>28</sup> The main idea is that the scattering amplitude is dominated by particle exchanges in the  $t$ -channel if the total cm energy  $\sqrt{s}$ , is large. The asymptotic behavior for the Regge Pole amplitude is expressed by

$$A(s,t) \sim g(t) s^{\alpha(t)} \quad (6.1) \quad ^{29}$$

where the Mandelstam Variables  $s$  and  $t$  are defined in the conventional manner.<sup>30</sup>

If, on the other hand, the low energy meson-baryon scattering data are examined, one observes that except for  $K^+N$  reactions the scattering process is dominated by resonance production.<sup>31</sup> These facts lead to entirely different mathematical parameterizations for the low and high energy scattering processes.

The obvious question is how one can reconcile this apparent difference, and construct a model that will continuously describe the experimental scattering process for all  $s$  values. One may also argue that no single description is necessary, and construct a Regge-resonance interference model.<sup>32</sup>

Veneziano<sup>1</sup> proposed a dualistic type model which offers a description of the scattering data for low energy as well as asymptotic regions of  $s$ . Its original form exhibits Regge behavior, and is explicitly crossing symmetric,

$$A(s,t,u) = \frac{\bar{\beta}}{\pi} \left[ B(1-\alpha(t), 1-\alpha(s)) + B(1-\alpha(t), 1-\alpha(u)) + B(1-\alpha(s), 1-\alpha(u)) \right] \quad (6.2)$$

where  $B$  is the Euler B-function and is defined by

$$B(x,y) = \frac{\Gamma(x) \Gamma(y)}{\Gamma(x+y)} \quad (6.3)$$

and  $\bar{\beta}$  is a constant. The functions  $\alpha(s)$  is the Regge trajectory in the  $s$  channel as previously defined, and  $\Gamma(x)$  is the gamma function. It is evident by examining equation (6.3) that the poles of the gamma function at  $0, -1, -2 \dots -N$  lie on the real part of the  $s$  axis if  $\alpha(s)$  is real. By allowing  $\alpha(s)$  to be imaginary one may not only move these poles to an acceptable unphysical region, but also give appropriate widths to the direct channel resonances.

The modified expression for  $\alpha(s)$  can be written as

$$\alpha(s) = A + Bs + iC\sqrt{s-4M^2} \quad (6.4)$$

where A and B describe a linearly rising trajectory, and C depends on the width of the s channel resonances. M is the mass of the pion in this work.

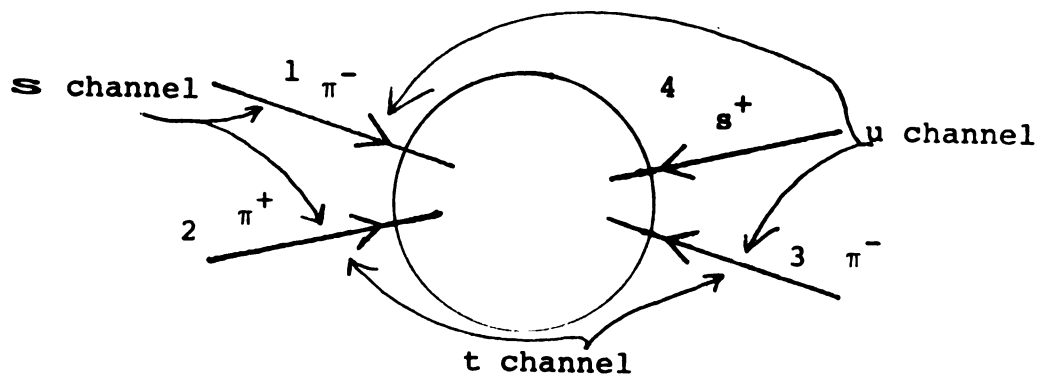
Lovelace<sup>2</sup> first applied Veneziano's formula to three-body final state scattering. In the analysis of the reaction  $\bar{p}n \rightarrow \pi^+\pi^-\pi^-$  at rest the initial spin parity state is assumed to be entirely  $0^-$ .

Bettini,<sup>33</sup> et al., has examined the reaction  $\bar{p}n \rightarrow \pi^+\pi^-\pi^-$  for laboratory momenta between 1.0 and 1.6 GeV/c and compared their data with the predictions of the Veneziano model. A phenomenological approach was taken with regard to the spin parity state of the  $\bar{p}n$  system. They found that the Veneziano Model was in good agreement with their data if they assumed the spin-parity of the  $\bar{p}n$  system was entirely in a  $2^+$  state, but contributions to the process by other states cannot be ruled out.

In this analysis the data are compared to the Veneziano model. Since the spin state composition for the  $\bar{p}n$  system has been determined in Chapter V, comparison can be made with Veneziano amplitudes appropriately summed over known percentages of participating spin states. This will give a stronger test of the Veneziano model since the spin state is obtained independently from the model comparison.

The problem of constructing an amplitude describing the decay of a state of given spin, parity and isospin into three pions has been investigated by Zemach<sup>34</sup> and Goebel, et al.<sup>35</sup> Goebel has investigated the specific problem of constructing Veneziano amplitudes for definite spin parity states. In Goebel's derivation the full amplitude is obtained by multiplying a spin factor times a scalar Veneziano amplitude. The spin factor consists of products of the final state particles momenta vectors. The scalar Veneziano amplitudes differ for different spin parity states because the full amplitude is required to exhibit Regge behavior.

In order to better understand how the Veneziano model will be related to the reaction  $\bar{p}n \rightarrow \pi^+\pi^-\pi^-$  discussed here, one is led to consider the scattering process  $\pi_1^-\pi_2^+ \rightarrow \pi_3^+s_4^-$  where particle  $s^-$  with spin  $S$  represents the  $\bar{p}n$  system. This process is shown below, with all four particles taken as incoming.



The four momentum conservation equation reads:

$$P_1 + P_2 + P_3 + P_4 = 0$$

The Mandelstam variables are defined as

$$s = s_{12} = -(P_1 + P_2)^2$$

$$t = s_{23} = -(P_2 + P_3)^2$$

$$\text{and } u = s_{13} = -(P_1 + P_3)^2$$

The dual nature of the Veneziano Model requires one to consider which channels have known resonances since resonant effects in one channel must be identical in the duality sense to particle exchanges in the cross channel. One can see that both the s and t channels are identical and may have resonances, while the u channel with isospin  $|I, I_z\rangle = |2, -2\rangle$  cannot. If the  $\bar{p}n$  system has the natural spin parity quantum numbers ( $S^P = 1^-, 2^+, 3^-, \dots$ ), one may write the full amplitude for the above mentioned scattering process<sup>35</sup> as

$$A(s_{12}, s_{23}) = \text{Const} * [\epsilon_{\mu\alpha\beta\gamma} P_{1\alpha} P_{2\beta} P_{3\gamma} S_{\mu} \dots (P_3)^L (P_1)^M V(s_{12}, s_{23}) + (1 \leftrightarrow 3)] \quad (6.5)$$

where  $S_{\mu}$  is the polarization tensor of the  $\bar{p}n$  system.

$\epsilon_{\mu\alpha\beta\gamma} = 0$  if any indices are equal.

-1 for odd permutations of the indices

+1 for even permutations of the indices



$S_\mu \dots (P_3)^L (P_1)^M$  is understood to mean the contraction of the polarization tensor  $S_\mu$  with  $L$  factors of  $P_3$  and  $M$  factors of  $P_1$ . The relationship  $L + M = S-1$  is required to hold in order for the contracted product to have vector qualities, and the amplitude to be a scalar. The notation  $(1 \leftrightarrow 3)$  will mean to symmetrize the previous term by interchanging particle 1 and 3.  $V(s_{12}, s_{23})$  is the appropriate Veneziano Scalar amplitude for the particular spin parity state being considered. The requirement for  $A(s_{12}, s_{23})$  to exhibit Regge behavior restricts the Veneziano amplitude to the form

$$V(s_{12}, s_{23}) = \frac{\Gamma(S-L - \alpha(s_{12})) \Gamma(S-M - \alpha(s_{23}))}{\Gamma(S+1 - \alpha(s_{12}) - \alpha(s_{23}))} \quad (6.6)$$

If the  $\bar{p}n$  system has unnatural spin parity quantum numbers ( $S^P = 0^-, 1^+, 2^- \dots$ ) the amplitude may similarly be written

$$A(s_{12}, s_{23}) = \text{Const} * S \dots (P_3)^L (P_1)^M V(s_{12}, s_{23}) + (1 \leftrightarrow 3) \quad (6.7)$$

where now  $S = L + M$  is required. The requirement of Regge behavior gives the form of the Veneziano Amplitude to be in this case

$$V(s_{12}, s_{23}) = \frac{\Gamma(m - \alpha(s_{12})) \Gamma(n - \alpha(s_{23}))}{\Gamma(m + n - p - \alpha(s_{12}) - \alpha(s_{23}))} \quad (6.8)$$

where

$$m \geq M+p; \quad n \geq L+p; \quad \text{and } p = \text{integer} \geq 0.$$

Further, one must have  $m \geq 1$  and  $n \geq 1$  to avoid the poles at  $\alpha(s_{ij}) = 0$ . All spin parity state up to spin of 4 are considered with the exception of  $0^+$ ,  $1^-$  and  $3^-$ . For a three pion system with arbitrary total spin  $J$ , one may write the parity as  $P = [\eta]^3 (-1)^L (-1)^\ell$  where  $\ell$  is the relative orbital angular momentum of the  $\pi^+ \pi^-$  system, and  $L$  is the orbital angular momentum of the third pion with respect to that system. Here  $\eta = -1$ , is the intrinsic parity of the pion. If the total spin  $J = 0$  then  $L = \ell$  and  $P = [\eta]^3 = -1$ , therefore  $0^+$  is forbidden.

Now one is led to consider the natural parity states  $J^P = 1^-, 2^+, 3^- \dots$  of a fermion-antifermion system of total spin  $S$  and relative orbital angular momentum  $\ell$ . The parity ( $P$ ), G-parity ( $G$ ), and charge conjugation operator ( $C$ ) are defined as  $-(-1)^\ell$ ,  $(-1)^{\ell+S+I}$  and  $(-1)^{\ell+S}$  respectively, where  $I$  is the isotopic spin. Since there are no single states one has  $S = 1$  and  $C = P$ . The isotopic spin of the  $\bar{p}n$  system is 1, therefore  $G = -(-1)^J$ . For a system of  $N$  pions, one has  $G = (-1)^N$  or here  $G = (-1)^3 = -1$ . But since  $G = (-1) (-1)^J$ ,  $J$  must be even and hence the states  $1^-, 3^-, \dots$  are excluded.

The spin tensor transition amplitudes for each of the allowed  $\bar{p}n$  spin parity states will now be explicitly



written in accordance with the prescription given by Goebel and Zemach.

$$J^P = 0^- \quad (L = 0, M = 0, p = 1) \quad T(0^-) = 1 \quad (6.9-A)$$

$$J^P = 1^+ \quad (L = 1, M = 0, p = 1) \quad T^i(1^+) = p_3^i + p_1^i \quad (6.9-B)$$

$$J^P = 2^- \quad (L = 1, M = 1, p = 0) \\ T^{ij}(2^-) = [p_{3i}p_{1j} + p_{1i}p_{3j}] - \frac{1}{3} \delta_{ij}[p_{3i}p_{1j} + p_{1i}p_{3j}] \quad (6.9-C)$$

$$J^P = 2^+ \quad (L = 1, M = 0) \\ T^{ij}(2^+) = [(\vec{p}_1 \times \vec{p}_3)^i p_3^j + (\vec{p}_1 \times \vec{p}_3)^j p_3^i] + [(\vec{p}_3 \times \vec{p}_1)^i p_1^j + (\vec{p}_3 \times \vec{p}_1)^j p_1^i] \\ (6.9-D)$$

$$T^{ijk}(3^+) = [p_3^i p_3^j p_1^k + p_3^k p_3^i p_1^j + p_3^j p_3^k p_1^i] \\ - \frac{1}{5} \delta_{ij} [|\vec{p}_3|^2 p_1^k + 2 p_3^k \vec{p}_1 \cdot \vec{p}_3] - \frac{1}{5} \delta_{ik} [|\vec{p}_3|^2 p_1^j + 2(\vec{p}_1 \cdot \vec{p}_3) p_3^j] \\ - \frac{1}{5} \delta_{jk} [|\vec{p}_3|^2 p_1^i + 2(\vec{p}_1 \cdot \vec{p}_3) p_3^i] + (1 \leftrightarrow 3). \quad (6.9-E)$$

In the explicit representation of the scalar Veneziano Amplitude only the term that exhibits the Regge behavior is considered.  $\alpha$  is taken as the  $\rho$ -f exchange degenerate trajectory, and none of the lower order daughter trajectories are used. Using the Veneziano amplitudes given by equation (6.6) and (6.8) along with the spin tensor transition amplitudes as in (6.9) one may finally write the total transition amplitude for each spin parity state as:

$$0^-) \quad A = \frac{\Gamma(1-\alpha(s_{12})) \Gamma(1-\alpha(s_{23}))}{\Gamma(1-\alpha(s_{12}) - \alpha(s_{23}))} \quad (6.10-A)$$

$$1^+) A^i = p_1^i \frac{\Gamma(1-\alpha(s_{12})) \Gamma(2-\alpha(s_{23}))}{\Gamma(2-\alpha(s_{12}) - \alpha(s_{23}))} + p_3^i \frac{\Gamma(1-\alpha(s_{23})) \Gamma(2-\alpha(s_{12}))}{\Gamma(2-\alpha(s_{12}) - \alpha(s_{23}))} \quad (6.10-B)$$

$$2^-) A^{ij} = \left[ [p_{3i} p_{1j} + p_{1i} p_{3j}] - \frac{1}{3} \delta_{ij} [p_{3i} p_{1j} + p_{1i} p_{3j}] \right] \frac{\Gamma(1-\alpha(s_{12})) \Gamma(1-\alpha(s_{23}))}{\Gamma(2-\alpha(s_{12}) - \alpha(s_{23}))} \quad (6.10-C)$$

$$2^+) A^{ij} = \left[ (\vec{p}_1 \times \vec{p}_3)^i p_3^j + (\vec{p}_1 \times \vec{p}_3)^j p_3^i \right] \frac{\Gamma(1-\alpha(s_{12})) \Gamma(2-\alpha(s_{23}))}{\Gamma(3 - \alpha(s_{12}) - \alpha(s_{23}))} \\ + \left[ (\vec{p}_3 \times \vec{p}_1)^i p_1^j + (\vec{p}_3 \times \vec{p}_1)^j p_1^i \right] \frac{\Gamma(1-\alpha(s_{23})) \Gamma(2-\alpha(s_{12}))}{\Gamma(3-\alpha(s_{12}) - \alpha(s_{23}))} \quad (6.10-D)$$

$$3^+) A^{ijk} = \left[ [p_3^i p_3^j p_1^k + p_3^k p_3^i p_1^j + p_3^j p_3^k p_1^i] - \frac{1}{5} \delta_{ij} [|\vec{p}_3|^2 p_1^k + 2 p_3^k \vec{p}_1 \cdot \vec{p}_3] \right. \\ \left. - \frac{1}{5} \delta_{ik} [|\vec{p}_3|^2 p_1^j + 2(\vec{p}_1 \cdot \vec{p}_3) p_3^j] - \frac{1}{5} \delta_{jk} [|\vec{p}_3|^2 p_1^i + 2(\vec{p}_1 \cdot \vec{p}_3) p_3^i] \right] \\ * \frac{\Gamma(1-\alpha(s_{12})) \Gamma(2-\alpha(s_{23}))}{\Gamma(3-\alpha(s_{12}) - \alpha(s_{23}))} + (1 \leftrightarrow 3) \quad (6.10-E)$$

The Dalitz plot is defined here to be the three dimensional figure described by the surface  $h(s_{12}, s_{23})$ , where the two independent variables  $s_{12}$  and  $s_{23}$  are represented along two mutually perpendicular cartesian coordinate axis. An important property of this representation, as proved in Appendix E, is that equal areas on the Dalitz plot correspond to equal probabilities in phase space. One therefore expects that the surface  $h$  will be proportional to the square of the transition matrix amplitude for values of  $s_{12}$  and  $s_{23}$  in the kinematically allowed region. The Dalitz plot comparison is especially well suited for the Veneziano model since the scalar amplitude has only two independent variables, aside from an overall scale factor. The Dalitz plot here will be symmetric along the diagonal since the two negative pions are indistinguishable.

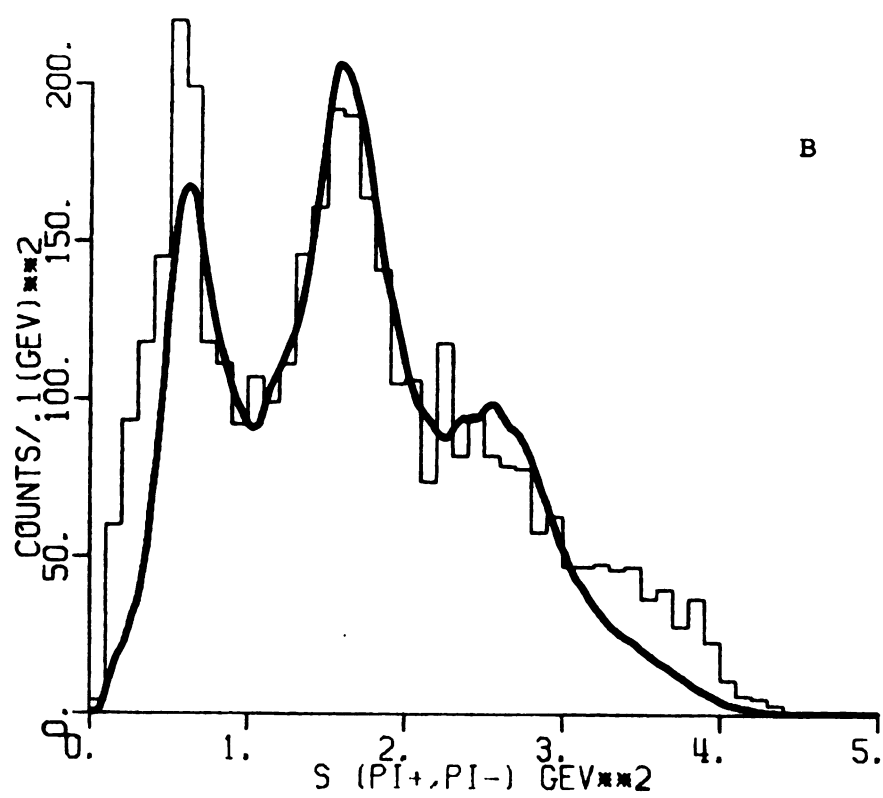
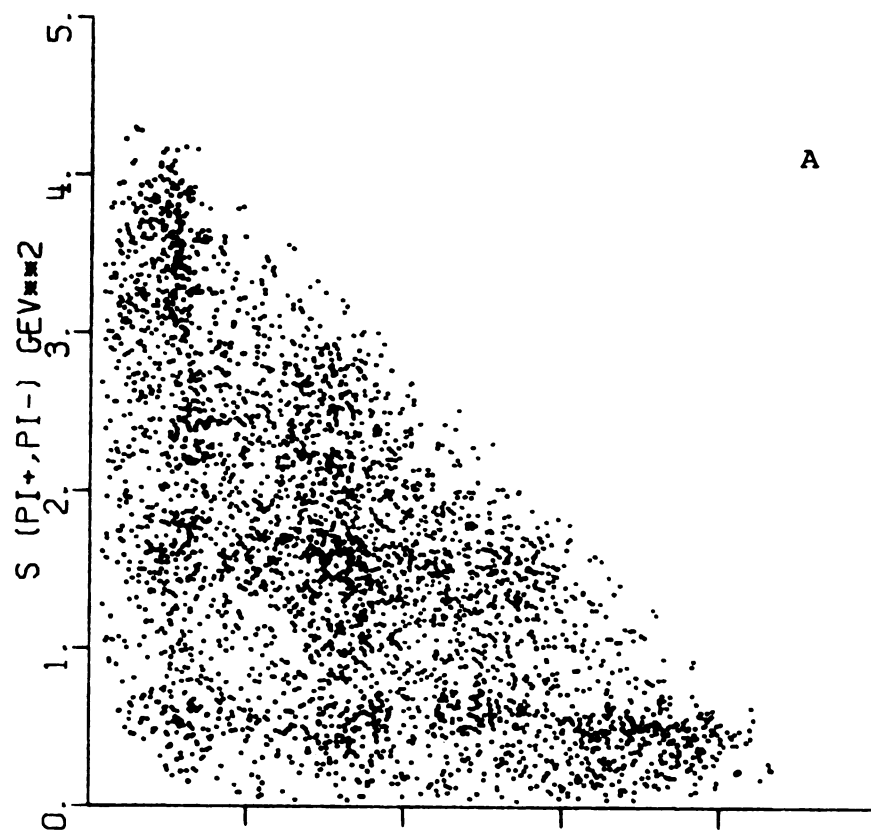
The data comparison has been separated into two samples. Sample 1 consists of the 1914 events (3828 points on the Dalitz plot) with laboratory momentum from 1.09 to 1.43 GeV/c. Sample 2 consists of 610 events (1220 Dalitz plot points) with laboratory momentum from 1.6 to 2.0 GeV/c, and is taken from reference 15. Chapter V describes the spin analysis performed with the data in sample 1. The events in sample 2 were analyzed in a manner similar to the phenomenological approach taken by Bettini. The analysis here will serve to extend this comparison up to laboratory momentum of 2.0 GeV/c. Figure 6.1 shows the

Fig. 6.1.--Group 1 data for

A. The Dalitz plot of  $s(\pi^+\pi_1^-)$  vs  $s(\pi^+\pi_2^-)$

B. The projection onto the mass squared axis

The Veneziano prediction is shown as a smooth curve.



Dalitz plot and its projection onto the invariant mass squared axis for the data in sample 1. One observes strong  $\rho^0$  and  $f^0$  resonant bands at .57 and 1.64  $\text{GeV}^2$ , respectively. The minimum density areas, in between the resonant bands, on the Dalitz plot are also very evident. Figure 6.2 shows the Dalitz plot and its projection onto the invariant mass squared axis for the data in sample 2. One here observes similar features as in the sample 1 data.

The values of A and B in Equation (6.4) were obtained by simultaneous solving:

$$\begin{aligned} \alpha(s = M_\rho^2) &= 1 = A + B(M_\rho^2) \\ \text{and} \quad \alpha(s = M_f^2) &= 2 = a + B(M_f^2) \end{aligned}$$

The parameters  $M_\rho$  and  $M_f$  were obtained by fitting the  $\pi^+\pi^-$  invariant mass distribution to Briet-Wigner resonance forms as described in Chapter 3.3. The values of  $M_\rho$  and  $M_f$  used for the sample 1 data were 760 MeV and 1277 MeV respectively. The values of  $M_\rho$  and  $M_f$  used for sample 2 data were 712 MeV and 1260 MeV respectively. The parameter C in equation (6.4) was determined by requiring that the Veneziano model give the correct width to the  $\rho^0$  meson. Table 6.1 lists A, B, and C for the data in sample 1 and sample 2. The values used here are compared to the values used by Lovelace, Bettini, and the normally accepted values<sup>36</sup> for the  $\rho$  trajectory.

The model was expressed in terms of the Dalitz plot parameters as

Fig. 6.2.--Sample 2 data for

A. The Dalitz plot of  $s(\pi^+\pi_1^-)$  vs  $s(\pi^+\pi_2^-)$

B. The projection onto the mass squared axis.

The Veneziano prediction is shown as a smooth curve.

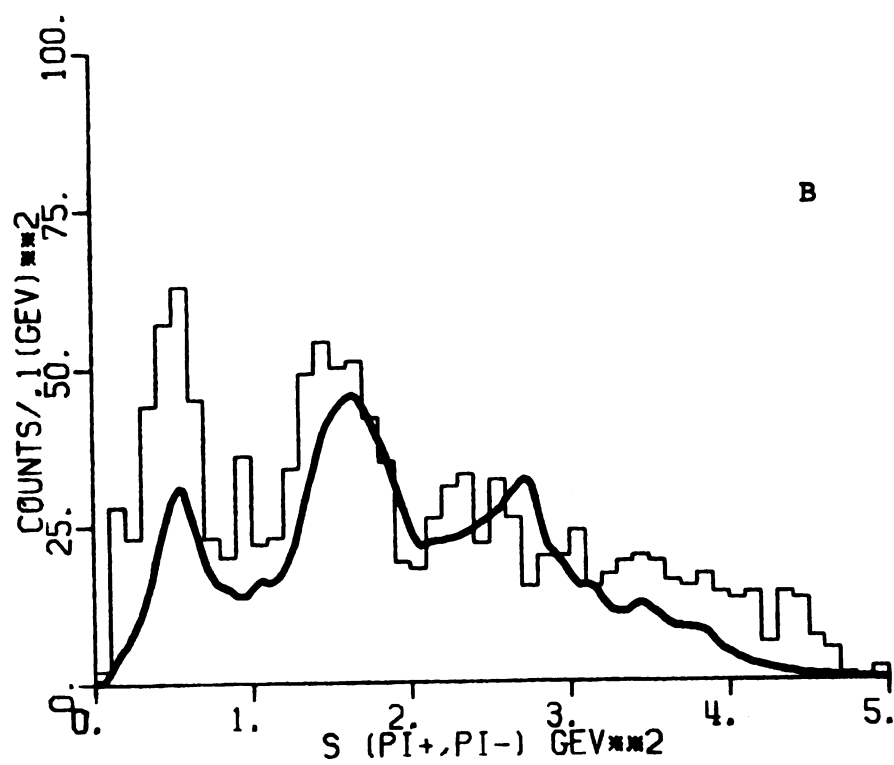
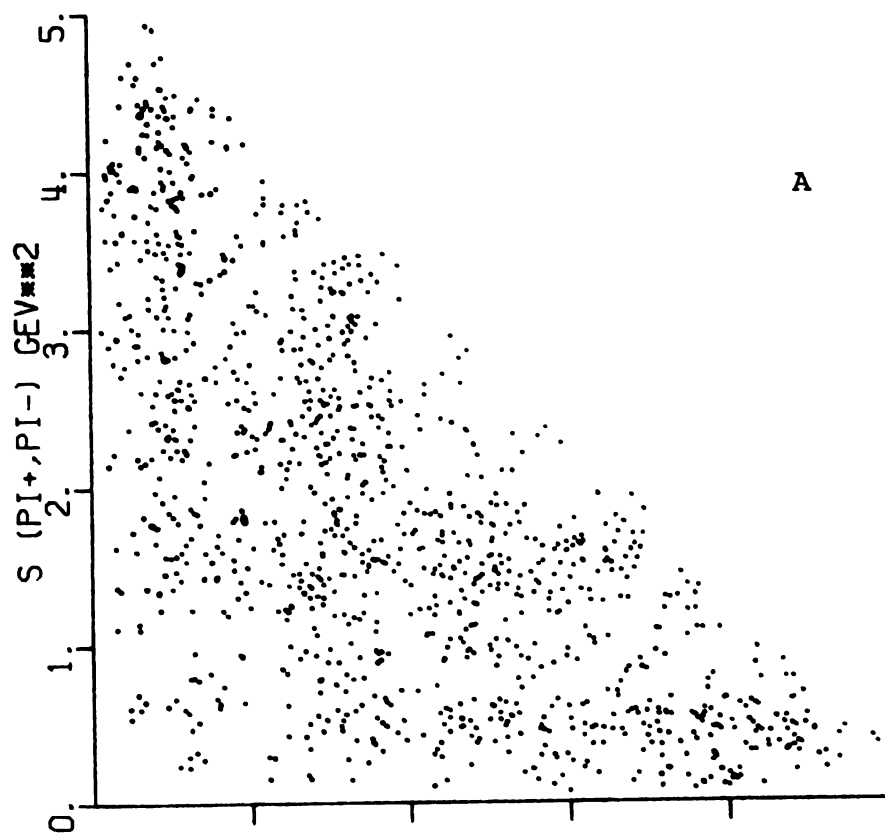




Table 6.1.--Values of the  $\rho$  trajectory parameters.

	Sample 1	Sample 2	Lovelace	Bettini	Accepted Value <sup>36</sup>
A	.46 $\pm$ .03	.53 $\pm$ .03	.483	.65	.57
B	.94 $\pm$ .01	.925 $\pm$ .01	.885	.84	.91
C	.25 $\pm$ .003	.20 $\pm$ .003	.28	.26	--

$$|T|^2 = \sum_p a^{J^P} |T^{J^P}(s_{12}, s_{23})|^2$$

where  $|T|^2$  is the square of the total transition matrix element and  $|T^{J^P}(s_{12}, s_{23})|^2$  is the square of the transition matrix elements given in equation (6.10).  $a^{J^P}$  is the percentage of each contributing spin parity. The fit was performed by considering Dalitz plot grid sizes of .5 (GeV)<sup>2</sup>. Approximately 60,000 events were selectively generated by a Monte Carlo routine, Sage II,<sup>37</sup> according to the number of events present at each momentum in the two data samples. These events were further weighted according to the magnitude of the square of the transition matrix element. The normalization requirements are  $\sum_{ij} |T_{ij}^{J^P}|^2 = \sum_{ij} \text{Data}_{ij}$  where  $i$  and  $j$  are the Dalitz plot grid point coordinates, and  $a^{J^P}$  are constrained to remain within two standard deviations of the values given in Table 5.1. Since the parity of the spin 2 state could not be determined, contributions from both the  $2^+$  and  $2^-$  states were assumed possible. The fit, projected onto one invariant

mass squared axis, for the data in sample 1 is given in Figure 6.1 as a smooth curve. Figure 6.3 shows comparison slices across the Dalitz Plot. Figure 6.4-B shows a Dalitz plot of the fit. Figure 6.4-A shows a Dalitz plot illustration of the absolute deviation between the Data and the Model. Overall one observes good agreement between the data and the model. Obvious area of disagreement are when  $s_{12}$  is large and  $s_{23}$  is small and vice versa.

Figure 6.2 shows a comparison of the invariant mass squared predicted by the model, with the data for the events in sample 2. Figure 6.5 gives a comparison for slices across the Dalitz plot. Figure 6.6 show the Dalitz plots for the model, and the absolute deviation between the model and the data. The area of disagreement seen before are also present here.

The percentage of each spin parity state used in the fit, and the overall normalization is shown in Table 6.2. The amount of each spin state for the data in sample 2 was not constrained in the fitting process. The necessity for higher spin states is consistent with the expectation one might have had for this higher momentum sample.

Table 6.2.--Percentages of each spin parity state and N,  
the ratio of the fitted to the total number  
of events.

	0-	1 <sup>+</sup>	2 <sup>-</sup>	2 <sup>+</sup>	3 <sup>+</sup>	N
Sample 1	0	.16	0	.68	.16	.90
Sample 2	0	0	0	.74	.26	.70

Fig. 6.3.--The comparison of the Veneziano fit to the data in sample 1 for slices across the Dalitz plot.

- |                              |                              |
|------------------------------|------------------------------|
| A. .0 to .2 $\text{GeV}^2$   | E. 1.9 to 2.5 $\text{GeV}^2$ |
| B. .2 to .8 $\text{GeV}^2$   | F. 2.5 to 3.0 $\text{GeV}^2$ |
| C. .8 to 1.4 $\text{GeV}^2$  | G. 3.0 to 3.6 $\text{GeV}^2$ |
| D. 1.4 to 1.9 $\text{GeV}^2$ | H. 3.6 to 5.0 $\text{GeV}^2$ |

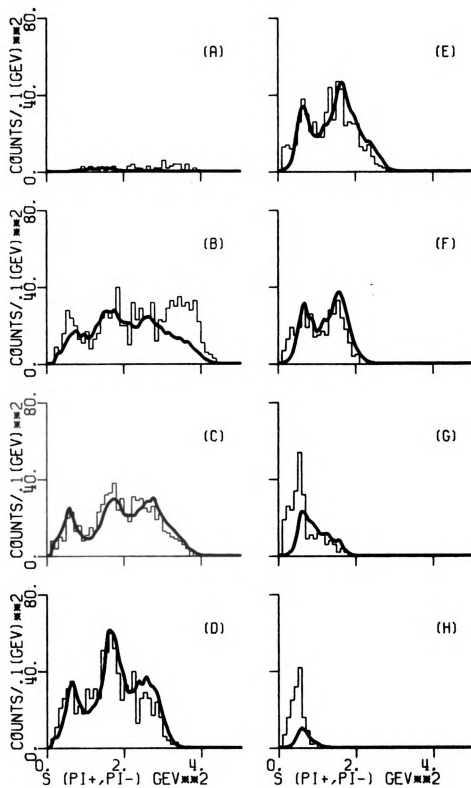


Fig. 6.4.--Dalitz plot of the Veneziano Model fit for sample 1 for

- A. The absolute deviation between the model and the data
- B. The Fit

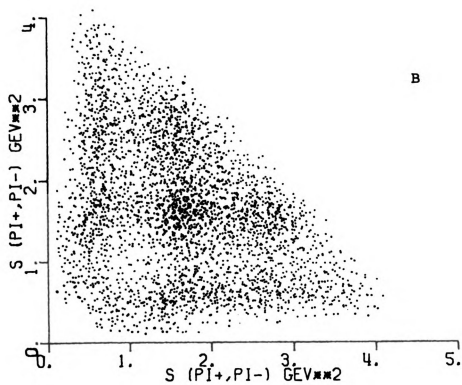
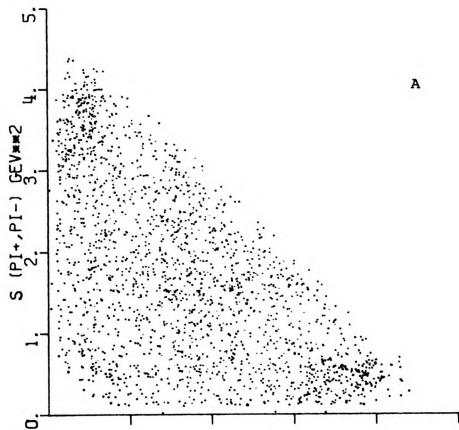


Fig. 6.5.--The comparison of the Veneziano fit to the data in sample 2 for slices across the Dalitz plot

- A. .0 to .2  $\text{GeV}^2$
- B. .2 to .8  $\text{GeV}^2$
- C. .8 to 1.4  $\text{GeV}^2$
- D. 1.4 to 2.0  $\text{GeV}^2$
- E. 2.0 to 2.6  $\text{GeV}^2$
- F. 2.6 to 3.2  $\text{GeV}^2$
- G. 3.2 to 3.8  $\text{GeV}^2$
- H. 3.8 to 5.0  $\text{GeV}^2$



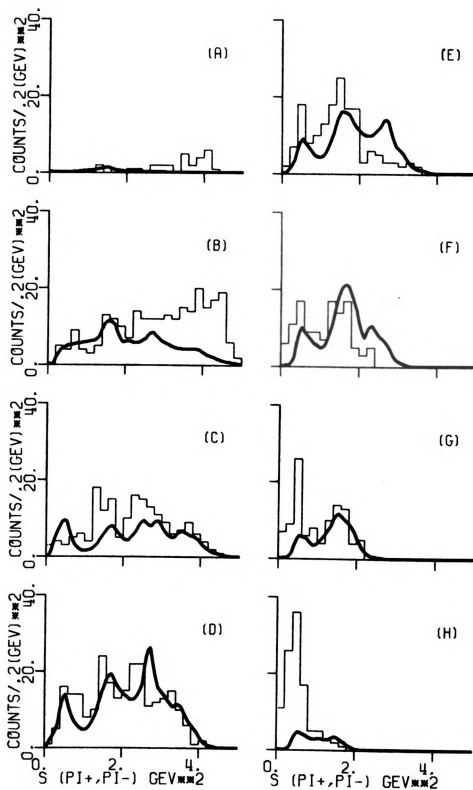
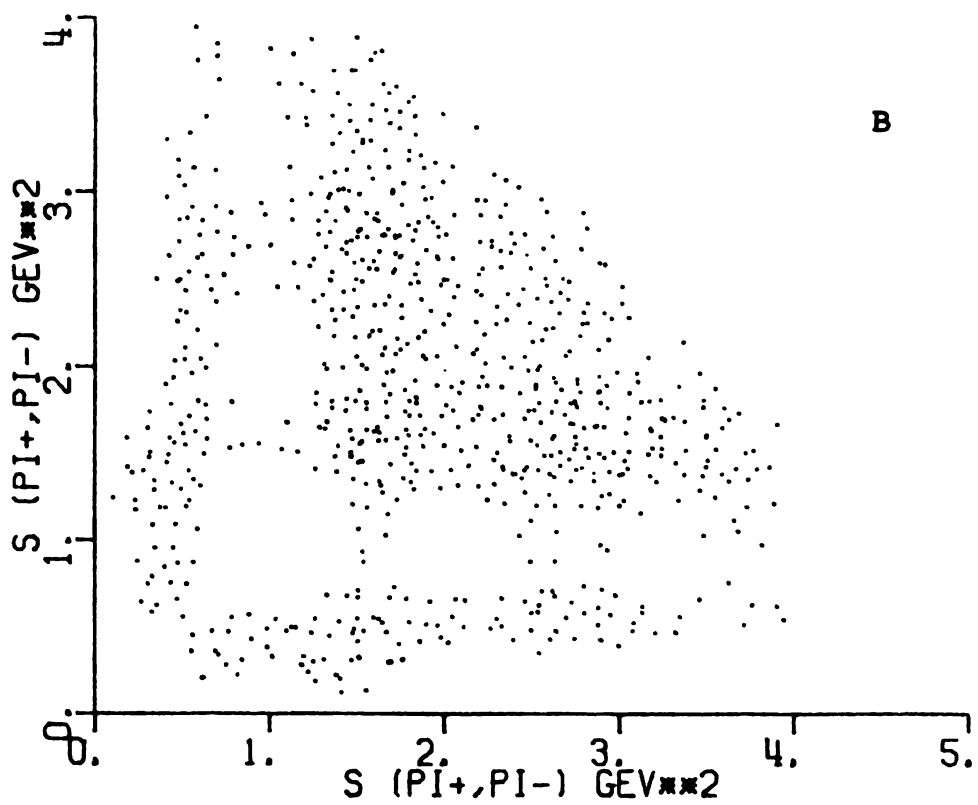
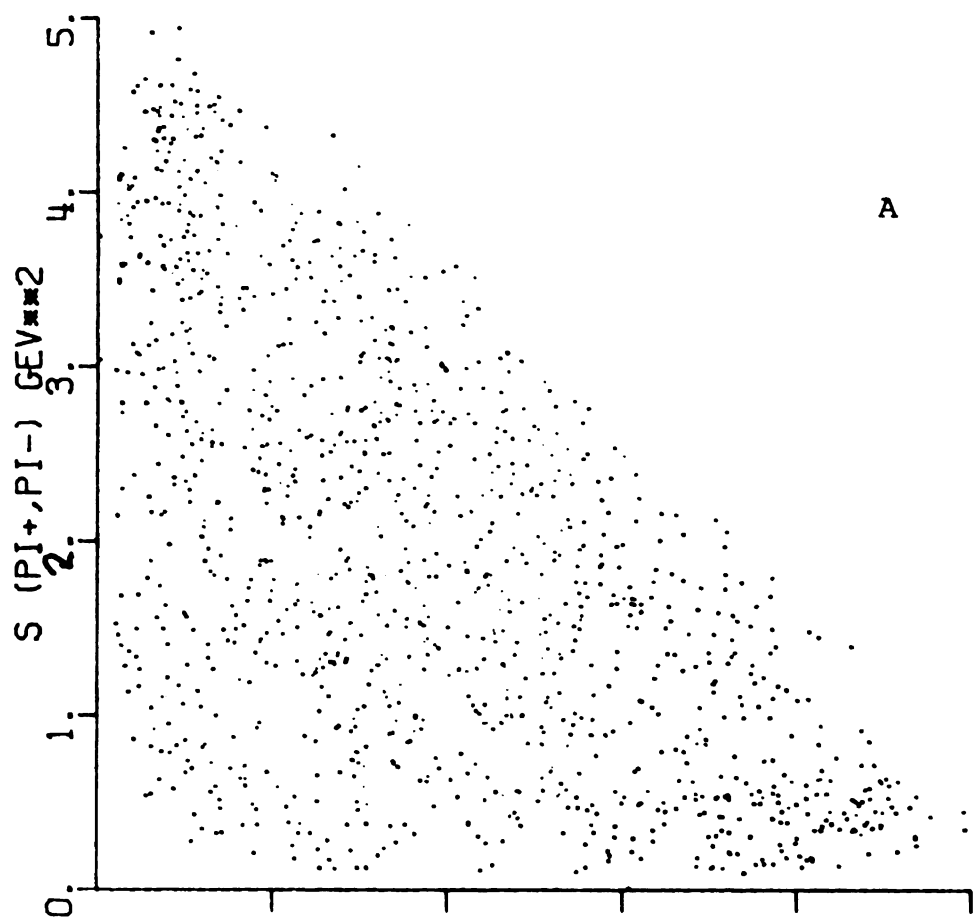


Fig. 6.6.--Dalitz plot of the Veneziano Model fit for  
sample 2 for

A. The absolute deviation between the model  
and the data

B. The fit



## CHAPTER VII

### SUMMARY AND CONCLUSIONS

In this experiment a total of 121,399 antiproton deuteron interactions were analyzed. Data were collected using the 31-inch deuterium bubble chamber at the Brookhaven National Laboratory exposed to an antiproton beam at 1.09, 1.19, 1.31, and 1.42 GeV/c momenta. The cross sections were determined for the 3, 4, 5, and 6 prong topologies that had a proton spectator. The cross sections for the odd prong topologies agreed well with the cross sections from higher momentum data.

An even prong event results when the spectator has sufficient momentum to produce a visible track in the bubble chamber. In this experiment, events with spectator proton momentum up to 1. GeV/c were measured. Correcting for deuteron shadowing effect, topological cross sections for  $\bar{p}n$  interactions were obtained. These were found to be in good agreement with predictions from the impulse approximation. The  $\bar{p}n \rightarrow \pi^+ \pi^- \pi^-$  reaction cross sections were determined by analyzing  $\bar{p}d \rightarrow p_{sp} + \pi^+ \pi^- \pi^-$  events. This reaction was found to be dominated by the production

of  $\rho^0$  and  $f^0$  resonances. Cross sections for  $\rho^0\pi^-$  and  $f^0\pi^-$  resonance states were determined and were found to be in excellent agreement with data from higher momenta.

Not only do these cross sections add valuable knowledge to the subject of antiproton neutron interaction, but the excellent agreement with data from higher momenta further serves the purpose of establishing reputable credentials for the data for use in the dynamics analysis.

The different cross sections  $\frac{d\sigma}{dt}$  and  $\frac{d\sigma}{du}$  were obtained for both the  $\rho^0$  and  $f^0$  meson production. The slopes of the forward and backward differential cross sections were shallow, and consistent with being identical. In order to test the crossing symmetry principle the differential cross section for the reaction  $\bar{p}n \rightarrow \rho^0\pi^-$  was compared with its line reversed reaction  $\pi^-p \rightarrow n\rho^0$ . The agreement between the slope parameters and intercept comparison indicates that the crossing symmetry principle is applicable to these quasi two body reactions at this low momentum. The c.m. angular distribution for the  $\rho^0$  and  $f^0$  were found to be nearly symmetric about  $\cos \theta^* = 0$ . From these distributions the spin of the  $\bar{p}n$  system was found to be predominately in a  $s = 2$  state.

The Dalitz plot for the invariant mass square of the  $\pi^+\pi^-$  system show strong  $\rho^0$  and  $f^0$  bands. The minimum density areas in between the bands are also evident. The predictions of the Veneziano model was compared to the data in this experiment and data at 1.60, 1.75, 1.85, and

2.00 GeV/c from Reference 15. The Veneziano model was constructed by multiplying tensor spin-parity functions times scalar Veneziano amplitudes. Since for the data in this experiment the spin state composition of the  $\bar{p}n$  system is known, the magnitudes of the spin parity functions are constrained to these values in the comparison. For the comparison with the higher momenta data, the magnitudes of the spin-parity functions were free parameters in the fit.

The model gives good agreement with the data at the lower momentum region. Noticeable area of disagreement are at places where the invariant mass square of the  $(\pi^+\pi_1^-)$  system is large and that for the  $(\pi^+, \pi_2^-)$  system is small. This disagreement becomes more prominent at the higher momentum region. The overall agreement between the data and the Veneziano model confirms the validity of the model and its application to the  $\bar{p}n \rightarrow \pi^+\pi^-\pi^-$  reaction at these laboratory momenta.

APPENDIX A

SCANNING EFFICIENCY DETERMINATION

## APPENDIX A

### SCANNING EFFICIENCY DETERMINATION

In order to determine the scanning efficiency an independent second scan was performed on 12 reels of film. All events from both scans were examined in a third scan and were classified according to the scan code numbers given in Table A-1. The results of the code number count for the add and even prong events are listed in Table A-2 and A-3 respectively.

Consider a total sample of  $N$  true events from which  $N_1$  and  $N_2$  events were found in scan 1 and scan 2 respectively. The number of events found in common is given by

$$N_1 \cap N_2 = P_1 P_2 N \quad (A-1)$$

where  $P_1$  and  $P_2$  are the probabilities of finding a good event in scans 1 and 2 respectively.

If the sets of  $N_1$ ,  $N_2$ , and  $N_1 \cap N_2$  are written in terms of the code numbers one finds that the number of events in common is the sum of the events with code 7, code 6 and code 5. This will be written as



$$N_1 \cap N_2 = 5 + 6 + 7 \quad (\text{A-2})$$

Similarly, 
$$N_1 = 1 + 3_{(1)} + 5 + 6 + 7 \quad (\text{A-3})$$

and 
$$N_2 = 2 + 3_{(2)} + 5 + 6 + 7. \quad (\text{A-4})$$

where  $3_{(1)}$ ,  $[3_{(2)}]$  represent the number of events which had a minor error in scan 1, [2], and a major error in scan 2, [1]. The scanning efficiencies can then be determined for scan 1 and scan 2 as

$$P_1 = \frac{N_1 \cap N_2}{N_2} \quad P_2 = \frac{N_1 \cap N_2}{N_1} .$$

Since the events with code 8 were measured twice, to obtain total number of events  $N$ , one must correspondingly lower the number of events found in the entire 72 roll sample by the fraction of code 8 events found in these selected 12 roll sample.

Table A-1-A.--Definition of the Scan Code Numbers.

Code number	Meaning
1	The event had a major error in scan 2; Scan 1 had no error
2	The event had a major error in scan 1; Scan 2 had no error
3	The event had a major error in one scan, and a minor error in the other
4	Junk event -- note reason
5	The event was found in both scans but scan 2 made a minor error
6	The event was found in both scans but scan 1 made a minor error
7	The event was found in both scans and both events were good
8	The event was measured twice

Table A-1-B.--Classification of Major and Minor Errors.

---

Major errors

- (a) The event was not found
- (b) Any type of prong misinterpretation except in the cases of three/four prong or five/six prong misinterpretation

Minor errors

- (a) A three prong event was measured as a four-prong event or vice versa.
  - (b) A five-prong event was measured as a six prong event or vice versa.
  - (c) The frame number was not the same in both scans
-

Table A-2.--Results of Code Number Count for the Three and Five Prong Events.

Roll	Scan	Code 1	Code 2	Code 3	Code 4	Code 5	Code 6	Code 7	Total
5	1	106	0		47	6	13	1118	1290
	2	0	124		81	6	13	1118	1342
10	1	201	0		74	4	11	1466	1756
	2	0	233		94	4	11	1466	1808
14	1	209	0		78	6	3	1377	1673
	2	0	175		116	6	3	1377	1677
24	1	85	0		39	11	2	786	913
	2	0	120		73	11	2	786	992
28	1	68	0		44	4	3	981	1100
	2	0	119		63	4	3	981	1170
34	1	128	0		47	3	20	1008	1205
	2	0	173		59	3	20	1008	1264

Table A-2.--Continued.

Roll	Scan	Code 1	Code 2	Code 3	Code 4	Code 5	Code 6	Code 7	Total
24	1	67	0		43	6	13	748	877
	2	0	53		52	6	13	748	872
49	1	120	0		53	1	10	920	1104
	2	0	169		103	1	10	920	1203
53	1	70	0		48	0	0	967	1085
	2	0	173		97	0	0	967	1237
61	1	43	0		30	5	25	627	730
	2	0	75		77	5	25	627	809
65	1	65	0		11	3	2	683	764
	2	0	75		70	3	2	683	832
69	1	44	0		19	3	5	541	609
	2	0	59		44	3	5	541	652

Table A-3.--Results of the Code Number Count for the Four and six Prong Events.

Roll	Scan	Prong	Code 1	Code 2	Code 3	Code 4	Code 5	Code 6	Code 7	Code 8	Total
5	1	4	186	0	3	43	3	4	679	9	927
	2	4	0	95	1	126	3	4	679	0	908
5	1	6	23	0	0	10	1	0	272	3	309
	2	6	0	39	0	36	1	0	272	0	348
10	1	4	158	0	0	48	2	2	867	19	1096
	2	4	0	193	0	149	2	2	867	0	1213
10	1	6	58	0	0	16	1	3	307	5	390
	2	6	0	75	1	56	1	3	307	0	443
14	1	4	216	0	4	47	1	6	718	16	1008
	2	4	0	180	0	65	1	6	718	0	970
14	1	6	55	0	0	9	3	3	274	1	345
	2	6	0	27	0	43	3	3	274	0	350
24	1	4	74	0	0	39	1	2	413	5	534
	2	4	0	89	0	86	1	2	413	0	591
24	1	6	28	0	0	5	0	0	153	1	187

Table A-3.---Continued.

Roll	Scan	Prong	Code 1	Code 2	Code 3	Code 4	Code 5	Code 6	Code 7	Code 8	Total
	2	6	0	24	0	27	0	0	153	0	204
28	1	4	91	0	0	23	0	1	467	2	584
	2	4	0	112	0	96	0	1	467	0	676
28	1	6	23	0	0	10	0	1	189	0	225
	2	6	0	36	0	45	0	1	189	0	271
34	1	4	182	0	4	49	2	5	614	9	865
	2	4	0	113	0	66	2	5	614	0	800
34	1	6	34	0	0	6	3	2	256	3	304
	2	6	0	42	0	53	3	2	256	0	356
44	1	4	81	0	3	35	1	0	450	9	579
	2	4	0	46	0	95	1	0	450	0	592
44	1	6	18	0	0	9	2	1	144	0	174
	2	6	0	22	0	26	2	1	144	0	195
49	1	4	79	0	1	39	0	1	499	8	626
	2	4	0	133	0	64	0	1	499	0	679

Table A-3.--Continued.

Roll	Scan	Prong	Code 1	Code 2	Code 3	Code 4	Code 5	Code 6	Code 7	Code 8	Total
49	1	6	30	0	1	14	1	1	209	1	257
	2	6	0	49	0	40	1	1	209	0	300
53	1	4	143	0	0	48	3	2	509	7	712
	2	4	0	81	0	84	3	2	509	0	679
53	1	6	36	0	0	10	0	3	149	2	248
	2	6	0	25	0	34	0	3	149	0	259
61	1	4	62	0	0	19	2	0	355	4	442
	2	4	0	61	0	84	2	0	355	0	502
61	1	6	12	0	0	6	2	1	120	2	143
	2	6	0	23	0	15	2	1	120	0	161
65	1	4	68	0	0	76	1	2	369	4	525
	2	4	0	67	0	97	1	2	369	0	536
65	1	6	6	0	0	9	0	0	127	4	146
	2	6	0	18	0	14	0	0	127	0	159
69	1	4	64	0	0	32	0	3	334	7	440



Table A-3.--Continued.

Roll	Scan	Prong	Code 1	Code 2	Code 3	Code 4	Code 5	Code 6	Code 7	Code 7	Total
	2	4	0	66	0	42	0	3	334	0	445
69	1	6	16	0	0	5	2	2	132	3	160
	2	6	0	21	0	20	2	2	132	0	177



APPENDIX B

MEASURING EFFICIENCY DETERMINATION

## APPENDIX B

### MEASURING EFFICIENCY DETERMINATION

To determine the measurement efficiency each event on the original scan tape was classified as passed or failed, depending on whether it did or did not appear on the final data tape. Table B-1 summarized the result of this classification. The measurement efficiencies given in Table B-2 are the ratios of the number of events on the final data tape to the number of events on the original scan tape. In these efficiencies one assumes that each counted event belonged in the desired sample. According to the scanning analysis some events measured were not in the desired sample, as defined in Table B-3. Since these events have a higher failure rate, the effect on the measurement efficiencies must be determined.

One imagines the data containing two samples of events; a desired sample with  $N_1$  events and measurement efficiency  $\epsilon_1$ , and an undesired sample with  $N_2$  events and measurement efficiency  $\epsilon_2$ . The measurement efficiencies in Table B-1 are the weighted average of these efficiencies,

$$\bar{\epsilon} = \frac{\epsilon_1 N_1 + \epsilon_2 N_2}{N_1 + N_2}$$

Then,  $\epsilon_1 = \frac{1}{N_1} \left[ \bar{\epsilon} (N_1 + N_2) - \epsilon_2 N_2 \right]$  represents the efficiency for the desired sample.

Based on a sample scan analysis,  $\epsilon_2$  was determined to be .55 and the percent of undesired events was 1.%. Table 2-2 lists the corrected measuring efficiencies. The overall effect for this experiment was .4%.

Table B-1.--The Total Number of Passed Events is Given in Table B-1-A; the Total Number of Failed Events is Given in Table B-1-B.

Table B-1-A.

Momentum gev/c	3 Prong	4 Prong	5 Prong	6 Prong
1.09	5063	6937	2235	2060
1.19	7567	9411	3347	2945
1.31	13634	17274	6379	5791
1.43	9427	12062	4164	3970

Table B-1-B.

Momentum gev/c	3 Prong	4 Prong	5 Prong	6 Prong
1.09	355	558	234	281
1.19	376	753	323	453
1.31	823	1229	674	787
1.43	471	806	402	558

Table B-2.--The measurement efficiencies for the entire Sample.

Momentum gev/c	3 Prong	4 Prong	5 Prong	6 Prong
1.09	.934	.926	.907	.380
1.19	.953	.926	.912	.367
1.31	.943	.934	.904	.880
1.43	.952	.937	.912	.877

Table B-3.--Events in Measured Sample which were Unwanted Quantified in Terms of Percentage of the Total Sample.

Description	3-Prong	4-Prong	5-Prong	6-Prong
No dark positive	-	3.8	-	2.5
Junk	.31	.19	.31	.19
Not beam	.25	.49	.25	.82
Out of fiducial volume	.55	.28	.55	.39
Wrong primary event type	.12	.41	.12	.93
Strange particles present	.13	.26	.13	.12
Dalitz Pair	-	.22	.02	.51
No event found	-	.23	-	.19

APPENDIX C

FIDUCIAL VOLUME LENGTH CALCULATION

## APPENDIX C

### FIDUCIAL VOLUME LENGTH CALCULATION

Figure C-1 shows the position of the fiducial volume with respect to the vertex positions of all measured events. If one knows the radius of curvature of the beam, and the azimuthal angle  $\phi$  of the beam at the vertex, the arc determined by these numbers will intersect the fiducial volume boundary at two points. The radius of curvature is determined by  $R = P/.03 B$ , where  $R$  is meters and  $P$  is the momentum of the incident particle in GeV/c moving at right angles to a magnetic field  $B$  in kilogauss.

The origin of the circle thus described, and as shown in Figure C-2, is given by

$$X_O = X_V + R \sin \phi$$

$$Y_O = Y_V - R \cos \phi$$

where  $(X_V, Y_V)$  is the vertex position for a measured event. By elementary geometry one finds that the circle will



intersect the fiducial volume boundary at

$$X = X_O - \sqrt{R^2 - (Y_O - Y_W)^2} \quad \text{and}$$

$$Y = Y_O + \sqrt{R^2 - (X_O - X_W)^2} \quad \text{if } 0 < \phi < 90^\circ \quad \text{or}$$

$$Y = Y_O - \sqrt{R^2 - (X_O - X_W)^2} \quad \text{if } 90^\circ < \phi < 180^\circ$$

where  $X_W$  and  $Y_W$  give the position of the fiducial volume boundary in the X and Y directions respectively.

The positions of intersection between the circle and the fiducial volume boundary were found for each interaction, and the arc length  $S = 2 R \arcsin (D/2R)$  was calculated, where D is the chord between the intersecting points. In this experiment the fiducial volume is defined by  $-24. < Y < 17.6$  cm and  $-10 < K < 10$  c.m. The average arc length is determined for each incident momentum setting and is given in Table 2-3.

One minor consideration worth mentioning is the energy loss of the beam particle as it travels through the liquid. This will cause the particle to spiral, thus increasing the fiducial volume length. The momentum loss  $dp/dx$  for a 1.3 GeV/c antiproton in deuterium is .3 (MeV/c)/cm. The average particle will lose a momentum of 12.5 MeV/c travelling through 41.7 cm of liquid deuterium. This effect is much less than the experimental uncertainties, therefore has been neglected.

Fig. C-1.--Vertex position of all measured events with respect to the fiducial volume. The coordinate system corresponds to a front view of the bubble chamber. The rectangular box represents the fiducial volume.

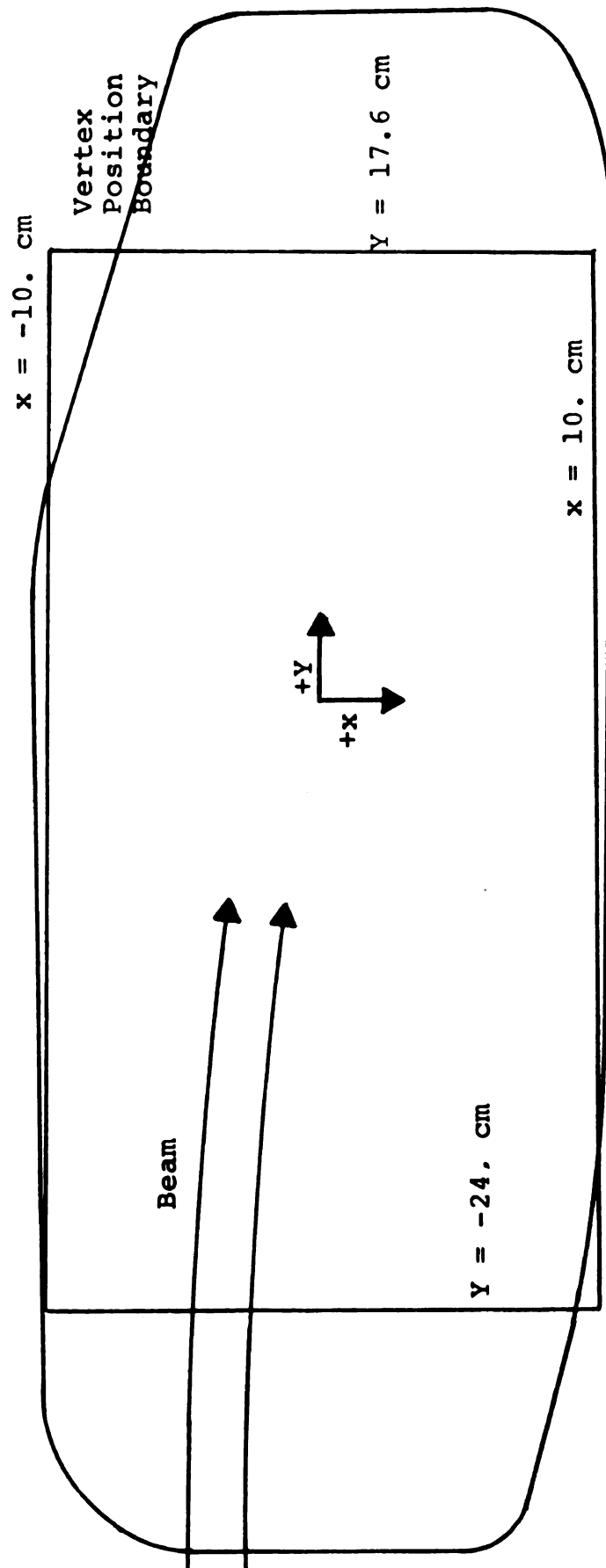
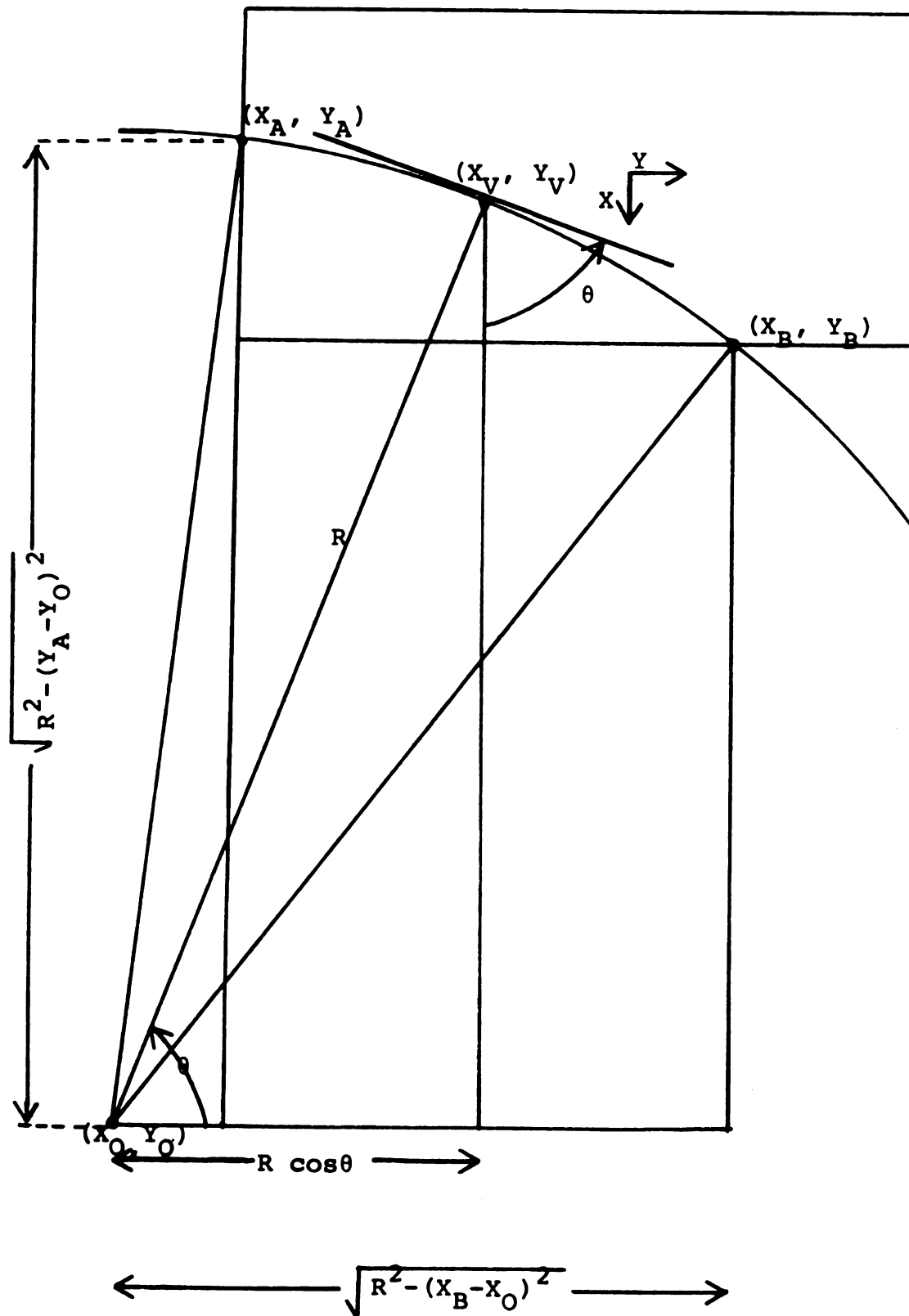


Fig. C-2.--Geometric picture of a circle with the same radius of curvature as the beam. The event vertex position is  $(X_V, Y_V)$ . The beam will intersect the fiducial volume at two points, labelled  $(X_A, Y_A)$  and  $(X_B, Y_B)$  in this example. The rectangular box represents the fiducial volume boundary.



APPENDIX D

TRACK COUNT

## APPENDIX D

### TRACK COUNT

Table D-1 gives the track count for beam passing through the upstream boundary of the measurement region. Table D-2 summarized the results.

In order to determine the corresponding track count for the fiducial volume, a correction must be made for beams entering the measurement region but interacting before reaching the fiducial volume.

Figure D-1 gives a two dimensional illustration of the vertex positions for all measured events, in relation to both the fiducial volume, and measurement region. The average distance between the two regions is 7.2 cm. Therefore it is necessary to calculate the attenuation of the beam through 7.2 cm of liquid deuterium. If  $N_0$  tracks enter the liquid then the number that survive at a distance  $\ell$  is given by  $N = N_0 e^{-\rho A_0 \sigma \ell / 2}$ , where  $\rho$  is the density of the liquid,  $A_0$  is Avagadros number and  $\sigma$  is the total cross section. One must reduce the original beam count by the percentage of beam loss  $1 - e^{-\rho A_0 \sigma \ell / 2}$  to yield the number of beam tracks entering the fiducial volume as listed in Table 2-4.

Table D-1.--Beam Count Results.

Reel	Frame number on Film	Number of frames on film	#Beam on basis of counting every 50th frame	Number of frames scanned	Estimated total number of beam
1	4 - 1227	1224	187	24	9537.0
2	3 - 2089	2087	452	42	22460.1
3	3 - 2101	2099	447	42	22339.3
4	1 - 2092	2092	514	41	26226.5
5	0 - 2095	2096	417	41	21317.8
6	5 - 2090	2086	250	41	12719.5
7	3 - 2075	2073	301	41	15218.8
8	1 - 2085	2055	392	41	19647.8
9	3 - 2087	2085	298	41	15154.4
10	2 → 2094	2093	567	41	28944.6
11	2 → 2100	2099	649	42	32434.5
12	6 → 2081	2076	578	41	29266.5
13	1 → 2108	2108	396	42	19875.4
14	1 → 2102	2102	635	42	31780.2
15	1 → 2102	2102	518	42	25924.7
16	0 → 2091	2092	284	41	14490.9
17	1 → 2093	2093	592	41	30220.9
18	3 → 2104	2102	549	42	27471.9
19	2 → 2093	2092	431	41	21989.6
20	1 → 2090	2090	386	41	19676.6
21	2 → 2096	2095	386	41	19723.7
22	1 → 2098	2098	417	41	21338.2
23	1 → 2100	2100	365	42	18250.0



Table D-1.--Continued.

Reel	Frame number on film	Number of frames on film	#Beam on basis of counting every 50th frame	Number of frames scanned	Estimated total number of beam
24	1 → 2198	2198	291	41	15600.4
25	1 → 2107	2107	575	42	28845.8
26	7 → 2087	2081	392	41	19896.3
27	1 → 2112	2112	393	42	19762.2
28	9 → 2114	2106	378	42	18954.0
29	3 → 2099	2097	364	41	18617.2
30	0 → 2096	2097	549	41	28079.3
31	1 → 2104	2104	593	42	29706.5
32	1 → 2101	2101	500	42	25011.9
33	2 → 2107	2106	512	42	25673.1
34	2 → 2097	2096	400	41	20448.8
35	18 → 2083	2066	462	41	23280.3
36	2 → 2100	2099	321	42	16042.4
37	2 → 2100	2099	401	42	20040.5
38	1 → 2091	2091	366	41	18666.0
39	2 → 2090	2089	300	41	15285.4
40	5 → 2092	2088	411	41	20930.9
41	1 → 2089	2089	251	41	12788.7
42	3 → 2092	2090	270	41	13763.3
43	2 → 2099	2098	272	41	13918.2
44	4 → 2098	2095	275	41	14051.7
45	1 → 2089	2089	210	41	10699.7
46	5 → 2092	2088	183	41	9319.5

Table D-1.--Continued.


Reel	Frame number on film	Number of frames on film	#Beam on basis of counting every 50th frame	Number of frames scanned	Estimated total number of beam
47	3 → 2104	2102	307	42	15364.6
48	2 → 2096	2095	344	41	17066.4
49	3 → 2096	2094	422	41	21552.9
50	2 → 2091	2090	432	41	22021.5
51	1 → 2109	2109	413	42	20738.5
52	1 → 1999	1999	462	39	23680.5
53	0 → 2086	2087	443	41	22549.8
54	2 → 2099	2098	386	41	19751.9
55	4 → 2093	2090	382	41	19472.7
56	2 → 2111	2110	309	42	15523.6
57	1 → 2092	2092	186	41	9490.5
58	0 → 2088	2089	169	41	8610.5
59	2 → 2094	2093	239	41	12200.6
60	2 → 2095	2094	210	41	10725.4
61	5 → 2096	2092	235	41	11990.7
62	2 → 2097	2096	210	41	10735.6
63	2 → 2089	2088	272	41	13852.1
63	3 → 2095	2093	238	41	12149.6
65	0 → 2111	2112	250	42	12571.4
66	1 → 2107	2107	196	42	9832.7
67	2 → 2132	2131	230	42	11669.8
68	2 → 2092	2091	232	41	11832.0
69	2 → 2088	2087	236	41	12013.0

Table D-1.--Continued.

Reel	Frame number on film	Number of frames on film	#Beam on basis of counting every 50th frame	Number of frames scanned	Estimated total number of beam
70	1 2088	2088	199	41	10134.4
71	3 2084	2082	194	41	9851.4
72	2 2080	2079	203	41	10293.6

Table D.2.--Summary of the Track Count.

Reel number	Momentum	Number of tracks (counting every 50th frame)	Number of frames scanned	Total number of frames in the experiment	Estimated number of tracks counted	Average number of tracks per frames
57 + 72	1.09	3499	659	33514	177953	5.31
41 + 56	1.19	5361	657	33423	272263	8.15
17 + 40	1.31	10334	994	50407	523512	10.39
1 + 16	1.43	6885	645	32569	347338	10.66

 Camera view

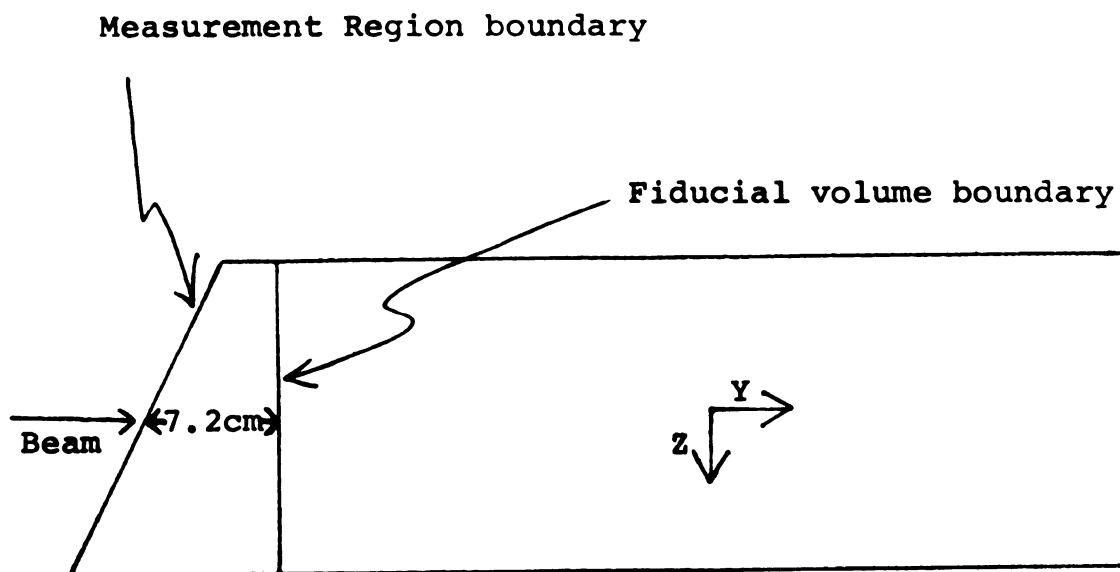


Fig. D.1.--Vertex position for all measured events.

APPENDIX E

PROOF THAT EQUAL AREAS ON THE DALITZ PLOT  
CORRESPOND TO EQUAL PROBABILITIES  
IN PHASE SPACE

## APPENDIX E

### PROOF THAT EQUAL AREAS ON THE DALITZ PLOT CORRESPOND TO EQUAL PROBABILITIES IN PHASE SPACE

The phase space density of states for  $n$  bodies can be written in the relativistic co-variant manner as:

$$\rho_n(E) = \int \prod_{i=1}^n \frac{d^3 p_i}{2E_i} \delta^3 \left( \sum_{i=1}^n \vec{p}_i - \vec{P} \right) \delta \left( \sum_{i=1}^n E_i - E \right) \quad (E.1)$$

where  $\vec{P}$  is the total momentum,  $E$  is the total energy and  $\vec{p}_i$  is the momentum of the  $i^{\text{th}}$  particle,  $E_i$  is the energy of the  $i^{\text{th}}$  particle. If one considers a three body final state then

$$\rho_3(E) = \int \frac{d^3 p_1}{2E_1} \frac{d^3 p_2}{2E_2} \frac{d^3 p_3}{2E_3} \delta^3 (\vec{p}_1 + \vec{p}_2 + \vec{p}_3 - \vec{P}) \delta(E_1 + E_2 + E_3 - E)$$

integrating over  $d^3 p_3$  and writing  $d^3 p_i = p_i^2 dp_i d\Omega_i$  one obtains

$$\rho_3(E) = \frac{1}{8} \int \frac{d\Omega_1 p_1^2 dp_1 d\Omega_2 p_2^2 dp_2}{E_1 E_2 E_3} \delta(E_1 + E_2 + E_3 - E) \quad (E.2)$$

1  
2  
3  
4



If the quantization axis is taken along  $\vec{P}_1$  then  $\int d\Omega_1 \rightarrow 4\pi$  and  $d\Omega_2 \rightarrow 2\pi d(\cos \theta_{12})$ , where  $\theta_{12}$  is the relative angle between  $\vec{P}_1$  and  $\vec{P}_2$ . In the  $\vec{P}$  rest frame one has  $\vec{P}_1 + \vec{P}_2 + \vec{P}_3 = 0$  so  $P_3^2 = P_1^2 + P_2^2 + 2P_1P_2 \cos \theta_{12}$ . The symbols  $P_1$ ,  $P_2$ , and  $P_3$  will be used to represent the magnitude of the vectors  $\vec{P}_1$ ,  $\vec{P}_2$ , and  $\vec{P}_3$  respectively. Differentiating with respect to  $P_3$  one has

$$2 P_3 d P_3 = 2 P_1 P_2 d(\cos \theta_{12})$$

one can therefore replace

$$d\Omega_1 P_1^2 d\Omega_2 P_2^2 dP_1 dP_2 \text{ as } 8\pi^2 P_1 dP_1 P_2 dP_2 P_3 dP_3 \text{ and write}$$

equation E.2 as:

$$\rho_3(E) = \pi^2 \int \frac{P_1 dP_1}{E_1} \frac{P_2 dP_2}{E_2} \frac{P_3 dP_3}{E_3} \delta(E_1 + E_2 + E_3 - E)$$

Differentiating  $E^2 = P^2 + M^2$ , one has  $dE = \frac{P}{E} dP$ , so

$$\rho_3(E) = \pi^2 \int dE_1 dE_2 dE_3 \delta(E_1 + E_2 + E_3 - E)$$

integrating over  $E_2$  gives

$$\rho_3(E) = \pi^2 \int dE_1 dE_3 \quad (E.3)$$

The invariant mass squared of particles 1 and 2 is defined as

$$s_{12} = (E_1 + E_2)^2 - (\vec{p}_1 + \vec{p}_2)^2$$

In the  $\vec{p}$  rest frame  $s_{12} = (E - E_3)^2 - p_3^2 = E^2 + m_3^2 - 2EE_3$

Differentiating with respect to  $E_3$  one has

$$ds_{12} = (-2E) dE_3 = \text{const } dE_3$$

similarly  $ds_{12} \sim dE_2$  and  $ds_{23} \sim dE_1$

In terms of the invariant mass squared variables (E.3)

becomes

$$\rho_3 \sim \int d(s_{12}) d(s_{23}) \quad (\text{E.4})$$

## LIST OF REFERENCES

# LIST OF REFERENCES

1. G. Veneziano, Nuovo Cimento 57A (1968) 190.
2. C. Lovelace, Phys. Lett 28B (1968) 264.
3. P. S. Eastman et al., Nuc. Phys. B51 (1973) 29.
4. F. T. Solmitz, A. P. Johnson, and T. B. Day, University of California, Berkeley; Alvarez Group Programming Note P-117.
5. O. I. Dahl, T. B. Day, and F. T. Solmitz, University of California, Berkeley; Alvarez Group Programming Note P-126.
6. Z. Ming Ma and G. A. Smith, Phys. Rev. Lett 27 (1971) 344.
7. Particle Data Group, LBL-58 (1972) 59.
8. P. D. Zeman, Z. Ming Ma, J. M. Mountz, and G. A. Smith, A Study of the Spectator Proton Distributions from the Reaction  $pd \rightarrow p_{sp} + \dots$  (to be published).
9. R. A. Donald et al., Nuc. Phys. B61 (1973) 333; and R. A. Donald et al., Nuc. Phys. B11 (1969) 551.
10. Particle Data Group, LBL-58 (1972) 23.
11. R. J. Abrams et al., Phys. Rev. D1 (1970) 1917.
12. T. Hamada and I. D. Johnston, Nuc. Phys. 34 (1962) 382.
13. J. P. Chandler, Behav. Sci. 14 (1969) 81.
14. D. L. Parker, Ph.D. Thesis, Michigan State University (1971), 70, unpublished.

15. Z. Ming Ma et al., Nuc. Phys. B51 (1973) 77.
16. H. Muirhead, Notes on Elementary Particle Physics, Pergamon Press, Inc. (1971) 167.
17. V. Barger and D. Cline, Phys. Lett. 25B (1967) 415.
18. B. C. Barish et al., Phys. Rev. Lett. 23 (1969) 607.
19. E. A. Paschos, Phys. Rev. 188 (1969) 188.
20. C. B. Chiu and J. D. Stack, Phys. Rev. 153 (1967) 1575.
21. V. Barger and P. Weiler, Phys. Lett. 30B (1969) 105.
22. J. Batou and G. Laurens, Nuc. Phys. B21 (1970) 551
23. P. B. Johnson et al., Phys. Rev. 176 (1968) 1651.
24. J. Myrheim; Letters Al Nuovo Cimento (1971) 221.
25. R. L. Kelley, G. L. Kane, and F. Henyey, Phys. Rev. Lett. 24 (1970) 1511.
26. J. D. Kimel, Physics Notes, Florida State University.
27. M. Jacob and G. C. Wick, Annals of Physics 7 (1959) 404.
28. T. Regge, Nuovo Cimento 14 (1959) 951.
29. R. Omnes and M. Freissert, Mandelstam Theory and Regge Poles (1963) 102.
30. William R. Frazer, Elementary Particles, Prentice-Hall, Inc. (1966) 16.
31. Particle Data Group, Review of Particle Properties, LBL-100 (1974) 33, and Physics Lett. Vol. 50B (1974).
32. V. Barger, Reviews of Modern Physics 40 (1968) 129.
33. A. Bettini et al., Nuovo Cimento 1A (1971) 333.
34. C. Zemach, Phys. Rev. 140B (1965) 97, and Phys. Rev. 133B (1964) 1201.
35. C. J. Goebel, Maurice L. Blackman, and Kameshwar, C. Wali, Phys. Rev. 182 (1969) 1487.

36. L. Van Hone, 13th International Conference on High Energy Physics (Berkeley) (1966) 253.
37. Jerry Friedman, University of California, Berkeley; Group A Programming Notes P-189.

MICHIGAN STATE UNIV. LIBRARIES



31293006218394